Biophysical and structural characterization of the interaction of the circadian transcription factor BMAL1 with its coactivator CBP

Dissertation

submitted to attain the academic degree
“Doctor of Natural Sciences”

at the Department of Biology
of the Johannes Gutenberg University Mainz

by

Archit Garg
born in Ghaziabad, India

Mainz 2020

Dekan:

1. Berichterstatter:

2. Berichterstatter:

Tag der mündlichen Prüfung: 05.05.2020

Preface

Parts of this thesis have been published:

Garg A, et al. (2019) Structural and mechanistic insights into the interaction of the circadian transcription factor BMAL1 with the KIX domain of the CREB-binding protein. *J. Biol. Chem.* doi: 10.1074/jbc.RA119.009845

Acknowledgments

The contents of this section have been removed for privacy.

Contents

Abbreviations

AEBSF	4-(2-aminoethyl)benzenesulfonyl fluoride hydrochloride
AEX	Anion-exchange chromatography
AMP	adenosine monophosphate
APS	Ammonium per sulfate
ATP	Adenosine triphosphate
β-Me	3-mercaptoethanol
β-TrCP	β-transducin repeat-containing protein
bHLH	basic helix-loop-helix
Bis-Tris	Bis(2-hydroxyethyl)amino-tris(hydroxymethyl)methane
BMAL1	Brain and muscle ARNT-like 1
bp	base pair
CD	Circular dichroism
CLOCK	Circadian Locomotor Output Cycles Kaput
CREB	cAMP response element-binding
CRY	Cryptochrome
CT	circadian time
Da	Daltons
DNA	Deoxyribonucleic acid
DNase	Deoxyribonuclease
dNTP	deoxyribonucleotide triphosphate
DPA	Day of proliferation arrest
DTT	1,4-dithiothreitol
E-box	enhancer box
E. coli	*Escherichia coli*
EDTA	Ethylenediaminetetraacetic acid
FBXL3	F-box/Leucine rich repeat protein 3

FF	Fast flow
FP	Fluorescence polarization
FL	full-length
FWHM	full width at half-maximum
GST	Glutathione S transferase
HEPES	4-(2-Hydroxyethyl)piperazine-1-ethanesulfonic acid
HRP	Horse radish peroxidase
IAA	iodoacetamide
IPTG	Isopropyl β-D-1-thiogalactopyranoside
KCl	Potassium chloride
K_D	Dissociation constant
kDa	kilodaltons
KIX	Kinase-inducible domain-interacting
LC-MS/MS	Liquid chromatography with tandem mass spectrometry
LB	Luria Bertani
MALDI	matrix-assisted laser desorption/ionization
MES	2-(N-morpholino)ethanesulfonic acid
$MgCl_2$	Magnesium chloride
$MgSO_4$	Magnesium sulfate
MLL	mixed lineage leukemia
MOPS	3-(N-morpholino)propanesulfonic acid
MS	Mass spectrometry
MST	Microscale Thermophoresis
NaCl	Sodium chloride
Nano-SPR	nano-Surface Plasmon Resonance
Ni	Nickel
$Na_2S_2O_3$	Sodium thiosulfate
PAS	PER-ARNT-SIM

PCR	Polymerase chain reaction
PEG	Polyethylene glycol
PER	Period
Pfu	*Pyrococcus furiosus*
PHR	Photolyase-homology region
pKID	phosphorylated kinase-inducible domain
PMSF	Phenylmethylsulfonyl fluoride
PSIPRED	PSI-blast based secondary structure prediction
PVDF	Polyvinylidene difluoride
rpm	revolutions per minute
rmsd	root-mean-square deviation
RT	room temperature
SAXS	small-angle X-ray scattering
SCN	suprachiasmatic nucleus
SDS-PAGE	sodium dodecyl sulfate-polyacrylamide gel electrophoresis
SEC	size-exclusion chromatography
SLIC	sequence and ligation independent cloning
TAE	Tris-acetate-EDTA
TB	terrific broth
TBS	Tris buffered saline
TBST	Tris buffer saline with Tween 20
TEMED	N,N,N,N'-Tetramethylethylenediamine
TEV	Tobacco Etch Virus
TOF	time of flight
Tris	2-Amino-2-(hydroxymethyl)-1,3-propanediol
WT, wt	wild-type
X-Gal	5-Bromo-4-chloro-3-indolyl-β-D-galactopyranoside

Abstract

The mammalian CLOCK:BMAL1 transcription factor complex and its coactivators CREB-binding protein (CBP)/p300 and mixed-lineage leukemia 1 (MLL1) play a central role in circadian transcriptional regulation and chromatin modification. The interactions of BMAL1's C-terminal transactivation domain (TAD) with the KIX domain of CBP/p300 (activating) and with CRY1 (repressing) as well as the BMAL1 G-region preceding the TAD regulate the circadian oscillations. The repressive BMAL1-TAD-CRY1 interactions are enhanced by the circadian acetylation of Lys-537 within the BMAL1 G-region. The CBP-KIX domain interacts with a plethora of transcription regulators via its two distinct pockets referred to as MLL- and CREB-pKID/c-Myb-binding pockets, typically targeting the intrinsically disordered regions within the TAD, which often attain folding upon binding to the KIX domain. In this thesis, we characterized the interaction of the CBP-KIX domain with BMAL1 proteins including the BMAL1-TAD, parts of the G-region, and Lys-537. Tethering the small compound 1-10 in the MLL-binding pocket of the CBP-KIX domain weakened BMAL1 binding and MLL1-bound KIX did not form a ternary complex with BMAL1, indicating that the MLL-binding pocket is important for KIX-BMAL1 interactions. Additionally, mutations in the second pKID/c-Myb-binding pocket of the KIX domain moderately impacted BMAL1 binding. The BMAL1(K537Q) mutation mimicking Lys-537 acetylation, however, did not affect the KIX-binding affinity, in contrast to its enhancing effect on CRY1 binding. Moreover, KIX binding does not induce the formation of extended regular secondary structures in BMAL1. SAXS models of BMAL1 and BMAL1:KIX complexes revealed that the N-terminal BMAL1 G-region including Lys-537 forms elongated extensions emerging from the bulkier BMAL1-TAD:KIX core complex. Fitting high-resolution KIX domain structures into the SAXS-derived envelopes suggested that the G-region emerges near the MLL-binding pocket, further supporting a role of this pocket in BMAL1 binding. This study significantly advances the mechanistic understanding of the roles of the BMAL1-TAD-CBP-KIX interaction and its interplay with other KIX ligands and with the BMAL1-CRY1 interaction in circadian gene regulation.

Zusammenfassung

Der Säuger-Transkriptionsfaktorkomplex CLOCK:BMAL1 und seine Coaktivatoren CREB-Bindungsprotein (CBP)/p300 und Mixed-Lineage-Leukämie 1 (MLL1) spielen eine zentrale Rolle bei der zirkadianen Transkriptionsregulation und Chromatinmodifikation. Die Wechselwirkungen der C-terminalen Transaktivierungsdomäne (TAD) von BMAL1 mit der KIX-Domäne von CBP/p300 (aktivierend) und mit CRY1 (reprimierend) sowie die BMAL1-G-Region vor der TAD regulieren die zirkadianen Oszillationen. Die repressiven BMAL1-TAD-CRY1-Wechselwirkungen werden durch die zirkadiane Acetylierung von Lys-537 in der BMAL1-G-Region verstärkt. Die CBP-KIX-Domäne interagiert mit einer Vielzahl von Transkriptionsregulatoren über zwei Bindestellen, den sogenannten MLL- und CREB-pKID/c-Myb-Bindetaschen, die typischerweise auf die intrinsisch ungeordneten Regionen innerhalb der TAD abzielen, die häufig beim Binden an die KIX-Domäne eine Faltung erreichen. In dieser Arbeit haben wir die Wechselwirkung der CBP-KIX-Domäne mit BMAL1-Proteinen einschließlich BMAL1-TAD, Teilen der G-Region und Lys-537 charakterisiert. Das Binden der kleinen Verbindung 1-10 in der MLL-Bindetasche der CBP-KIX-Domäne schwächt die BMAL1-Bindung und MLL1-gebundenes KIX bildet keinen ternären Komplex mit BMAL1, was darauf hinweist, dass die MLL-Bindetasche für KIX-BMAL1-Wechselwirkungen wichtig ist. Darüber hinaus wirkten sich Mutationen in der zweiten pKID/c-Myb-Bindetasche der KIX-Domäne mäßig auf die BMAL1-Bindung aus. Die BMAL1 (K537Q) -Mutation, die die Lys-537-Acetylierung nachahmt, beeinflusste jedoch nicht die KIX-Bindungsaffinität, im Gegensatz zu ihrer verstärkenden Wirkung auf die CRY1-Bindung. Darüber hinaus induziert die KIX-Bindung nicht die Bildung ausgedehnter regulärer Sekundärstrukturen in BMAL1. SAXS-Modelle von BMAL1 und BMAL1:KIX-Komplexen zeigten, dass die N-terminale BMAL1-G-Region einschließlich Lys-537 Verlängerungen bildet, die aus dem sperrigeren BMAL1-TAD:KIX-Kernkomplex hervorgehen. Das Einfügen von hochauflösenden KIX-Domänenstrukturen in die von SAXS abgeleiteten Hüllen deutete darauf hin, dass die G-Region in der Nähe der MLL-Bindestasche auftritt, was eine weitere Rolle dieser Tasche bei der BMAL1-Bindung unterstützt. Diese Studie verbessert das mechanistische Verständnis der Rolle der BMAL1-TAD-CBP-KIX-Wechselwirkung

und ihres Zusammenspiels mit anderen KIX-Liganden sowie mit der BMAL1-CRY1-Wechselwirkung bei der zirkadianen Genregulation erheblich.

1. Introduction

1.1 Circadian clock and molecular oscillators

Most organisms from bacteria to humans possess circadian rhythms coordinated by endogenous circadian clocks (Baker et al., 2012; Bell-Pedersen et al., 2005; Johnson et al., 2008; Lowrey and Takahashi, 2004; Yu and Hardin, 2006) which synchronizes them to the 24 h light-dark cycle, thereby exhibiting daily patterns of physiological processes. Nearly, every cell possesses a molecular clock capable of self-sustaining circadian rhythms (Buhr and Takahashi, 2013; Mohawk et al., 2012). Circadian rhythms regulate many physiological processes which includes regulation of body temperature, hormone secretion, metabolic and immune system activities, cell cycle and temporal homeostasis (Richards and Gumz, 2013; Takahashi et al., 2008).

1.1.1 The master clock in mammals

In mammals, the central autonomous master clock resides in the suprachiasmatic nucleus (SCN) of the hypothalamus in the brain which can directly get photo-entrained and maintains synchronization through coupling mechanisms. The SCN consists of approximately 20,000 neurons, each of which comprised of cell-autonomous circadian oscillators (Mohawk and Takahashi, 2011; Mohawk et al., 2012). The SCN receives the photic signal from the photoreceptor cells termed as ipRGCs (intrinsically photoreceptive retinal ganglion cells), expressing the photopigment melanopsin, in the retina (Berson, 2003; Mohawk et al., 2012). In the SCN, the light pulses induce phosphorylation of cAMP response element-binding protein (CREB) which then binds to the Ca^{+2}/cAMP regulatory elements (CREs) on DNA and activates the expression of *Per1* and *Per2*, thereby resetting the circadian clock (Gau et al., 2002; Travnickova-Bendova et al., 2002). The melanopsin-knockout mice displayed attenuated phase-resetting and circadian response to the light and the melanopsin deletion resulted in loss of intrinsic photosensitivity in the retinal ganglion cells (Lucas et al., 2003; Panda et al., 2002). Through systemic (e.g. body temperature) and endocrine cues (*Zeitgebers*; meaning “time giver”), the

photic information received by the SCN is passed to the peripheral clocks located throughout the body in mammals which mediate their synchronization (Buhr et al., 2010; Dibner et al., 2010) (Figure 1.1).

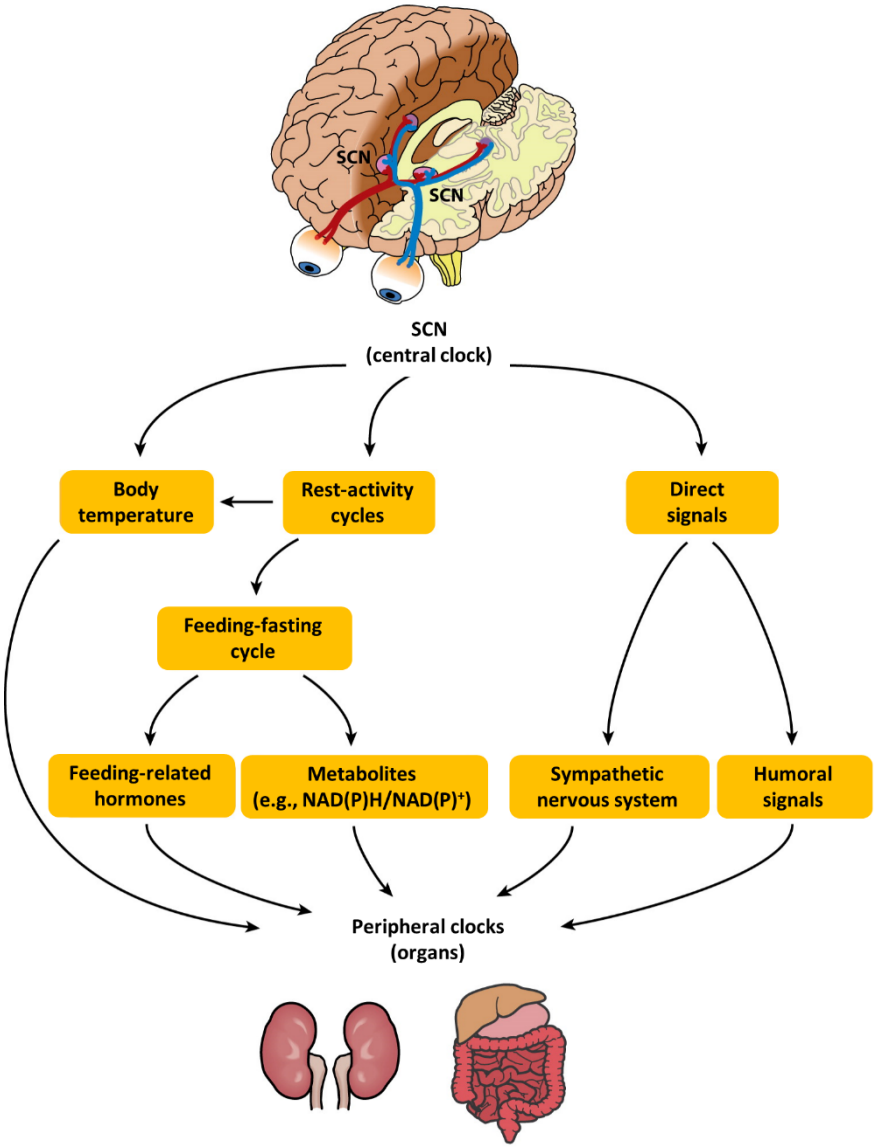

Figure 1.1. The entrainment pathways for the peripheral clocks. The central clock is synchronized mainly through the photic signals perceived by the retina and transmitted via synaptic transmission to the suprachiasmatic nucleus (SCN) neurons. In turn, the SCN, then synchronizes the peripheral clocks via direct signals such as humoral and neuronal signals, and via indirect cues imposed by the oscillating behavior, such as the rest-activity cycles and temperature. The rest-activity cycles generate feeding-fasting rhythms which act as the dominant *Zeitgebers* for many peripheral organs. Source: (Dibner et al., 2010).

1.1.2 Circadian oscillators and transcriptional/translational feedback loops

Most circadian systems are controlled through a common mechanism involving circadian oscillators that form the feedback loops comprising positive and negative elements, however, the components of the feedback loops vary in different organisms (Bell-Pedersen et al., 2005). In mammals, two transcriptional/translational feedback loops (TTFL) control the circadian rhythmicity. The basic helix-loop-helix (bHLH) transcriptional activators CLOCK (circadian locomotor output cycle kaput) and BMAL1 (brain and muscle ARNT-like protein-1), in the core TTFL, heterodimerize through their PAS (PER-ARNT-SIM) domains and bind to the E box elements of the promoters of *Period* (*Per1*, *Per2*, *Per3*), *Cryptochrome* (*Cry1*, *Cry2*) and several clock-controlled genes (ccgs), thereby activating their transcription (Merbitz-Zahradnik and Wolf, 2015; Partch et al., 2014) which leads to the accumulation of PER and CRY proteins. In the cytoplasm, the PER and CRY proteins heterodimerize, translocate to the nucleus and interact with CLOCK:BMAL1 to inhibit the transcriptional activation and their own transcription (Kume et al., 1999) (Figure 1.2). Through a second interconnected feedback loop, BMAL1 attenuates its own transcription by transcriptional activation of the nuclear orphan receptors such as retinoic acid-related orphan receptor α (*Rorα*) and *Rev-erbα*. The RORα protein activates the transcription of *Bmal1* while REV-ERBα inhibits it, thereby allowing the rhythmic BMAL1 expression (Merbitz-Zahradnik and Wolf, 2015; Mohawk et al., 2012). The phosphorylation of the PER protein by casein kinase 1 ε/δ (CK1 ε/δ) and the CRY protein by AMP kinase (AMPK) contribute to their degradation by promoting polyubiquitination of PER and CRY proteins by E3 ubiquitin ligases β-TrCP and FBXL3, respectively and thereby, degradation by 26S proteasome complex. The cycle begins again with 24h periodicity once the CLOCK:BMAL1 is relieved after the degradation of PER and CRY proteins (Busino et al., 2007; Shirogane et al., 2005) or the activation by co-activators (Etchegaray et al., 2003; Takahata et al., 2000).

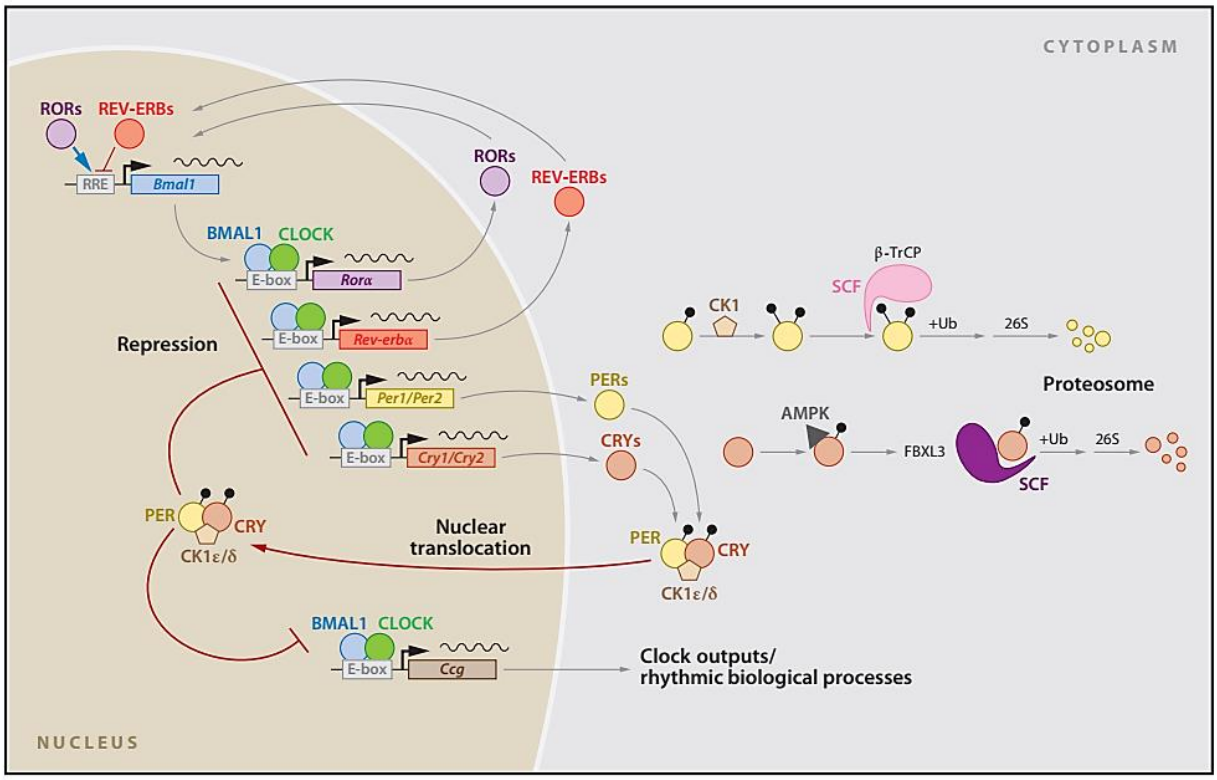

Figure 1.2. The molecular mechanism of the mammalian circadian clock. The core transcriptional/translational feedback loop consists of the activators CLOCK and BMAL1 and their target genes Per1, Per2, Cry1, and Cry2, whose gene products heterodimerize and form a negative-feedback repressor complex. Other feedback loop, driven by CLOCK:BMAL1, involves Rev-erbα and Rorα that represses the Bmal1 transcription. Many downstream target genes known as clock-controlled genes (Ccg) are also regulated by CLOCK:BMAL1. The SCF (Skp1-Cullin-F-box protein) E3 ubiquitin ligase complexes involving β-TrCP and FBXL3 regulates the stability of PER and CRY, respectively. The PER and CRY proteins are phosphorylated by casein kinase 1ε/δ (CK1ε/δ) and AMP kinase (AMPK), respectively, to promote polyubiquitination by their respective E3 ubiquitin ligase complexes, which promote their degradation by the 26S proteasome complex. Source: (Mohawk et al., 2012).

The analyses in the mouse liver led to a model of three different temporally separated states of the CLOCK:BMAL1-dependent circadian transcriptional regulation: an early repressive state, a late repressive or transcriptionally-poised state and an active state (Koike et al., 2012) (Figure 1.3). The PER:CRY complexes interact with CLOCK:BMAL1 in the early phase of repression between CT12-CT20 peaking at CT16-CT20 (CT = circadian time; CT0 = sunrise, usually onset of activity in diurnal organisms; CT12 = sunset, usually onset of activity in nocturnal organisms), and only CRY1 is sufficient for this repressive function in the late repressive state (CT0-CT4) (Gustafson and Partch, 2015; Merbitz-Zahradnik and Wolf, 2015; Ye et al., 2011, 2014). The early

repressive PER:CRY complexes are large multi-subunit complexes (several megadaltons) containing about 30 additional proteins that altogether can terminate transcription by chromatin and epigenetic modifications (Aryal et al., 2017; Brown et al., 2005; Duong et al., 2011; Padmanabhan et al., 2012) and over the time, its constituents can evolve (Duong and Weitz, 2014; Gustafson and Partch, 2015). Known components of the PER:CRY complexes include the histone methyltransferase subunit WDR5, the histone methyltransferase HP1Ɣ-Suv39H, the RNA-binding protein NONO, the pre-mRNA splicing factor (PSF) which recruits the SIN3-histone deacetylase complex (SIN3-HDAC) as well as RNA helicases such as senataxin (SETX) which is a helicase that promotes transcriptional termination (Aryal et al., 2017; Brown et al., 2005; Duong et al., 2011; Padmanabhan et al., 2012).

Until the appropriate time, the late repressive ternary CRY1:BMAL1:CLOCK complex prevents the transcriptional activation by coactivators such as histone acetyl transferase CREB-binding protein (CBP) and its paralog p300 (Koike et al., 2012; Shearman et al., 2000; Ye et al., 2011). The occupancy of BMAL1 and CLOCK increases at CT4-8 and in the absence of CRY1, the coactivators CBP/p300, which acetylate histone H3 K9/K14 (Etchegaray et al., 2003), interact with BMAL1 to begin the transcription again at CT8 which peaks at CT15 (Koike et al., 2012).

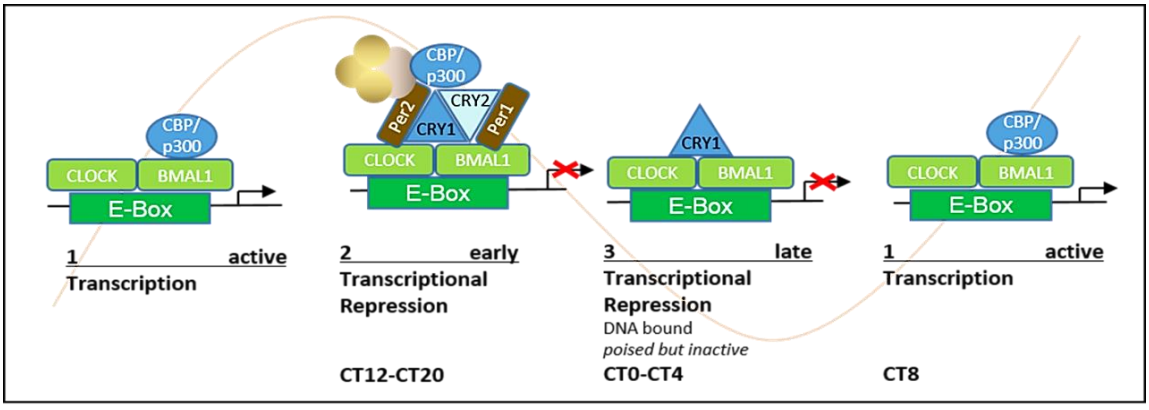

Figure 1.3. The daily rhythmic transcriptional cycles of the mammalian circadian clock. (1) In an active state, CLOCK/BMAL1 are bound to the E-box DNA and recruit CBP/p300 and potentially other co-activators such as MLL1. (2) In the early repressive state (~ CT12-CT20), large megadalton complexes including CRYs, PERs and additional factors (empty bulks; detailed in main text), which can terminate transcription by chromatin and epigenetic modifications, are recruited to CLOCK/BMAL1. (3) In the late repressive phase (about CT0-CT4), a repressive complex

is formed where only CRY1 is bound to CLOCK/BMAL1. (1) The dissociation of CRY1 and recruitment of CBP/p300 along with other coactivators leads to the reactivation of transcription at about CT8. CT = circadian time; CT0 = sunrise/light on; CT12 = sunset/light off. Source: (Merbitz-Zahradnik and Wolf, 2015)

1.1.3 Implications of the circadian clock in health

The circadian clock plays a key role in the regulation of majority of physiological processes (Richards and Gumz, 2013). The disruption of transcriptional regulation of the core circadian genes and the clock-controlled genes by CLOCK:BMAL1 and of the circadian rhythms is often involved in disease mechanisms. The knock out (KO) of circadian genes has been linked to the fluctuation in the blood pressure (Richards and Gumz, 2013). The *per1* KO leads to the lowering of the blood pressure in mice by interfering with the renal function (Stow et al., 2012) as also reported for the knockout of *Bmal1* (Curtis et al., 2007) and *Clock* (Zuber et al., 2009) genes while *Cry1/2* null mice displayed salt-sensitive hypertension (Doi et al., 2010). The loss of *Clock* in mice also leads to a phenotype revealing the mild diabetes insipidus (Zuber et al., 2009).

The disruption, mutation or loss of core circadian genes have also been linked to aging and heart-related problems. The *Bmal1*$^{-/-}$ mice shows the signs of premature aging (Kondratov et al., 2006) and die young. The BMAL1 deficient mice also develop age-associated dilated cardiomyopathy, which leads to the thinning of the ventricular walls, enlarging of the heart and its failure leading to the premature death (Lefta et al., 2012). The cardiomyocyte-specific clock mutant (CCM), wherein the cardiomyocyte circadian clock is selectively disrupted, displayed the reduction in heart rate and showed that the cardiomyocyte circadian clock plays a role in myocardial physiology (Durgan and Young, 2010; Richards and Gumz, 2013).

The circadian clock also possesses a role in metabolic syndromes such as diabetes and obesity. The knockout of *Bmal1* and *Clock* in mice leads to the reduction in insulin secretion and thereby, diabetes mellitus (Marcheva et al., 2010). The experimental desynchronization of circadian rhythms results in the accelerated onset of the diabetes in the diabetes-prone HIP rats in which the transgenic overexpression of human islet amyloid polypeptide leads to its accumulation and the pancreatic β cell failure which serve as a validated model for type 2 diabetes mellitus (Gale et al., 2011). The SCN-lesioned rats and mice show the disappearance of

circadian rhythmicity in glucose uptake and insulin sensitivity and glucose tolerance is enhanced in SCN-lesioned rats (Coomans et al., 2013; La Fleur et al., 2001).

The high fat diet leads to the significant increase in the body weight in *Per3* single KO or *Per1/2/3* triple KO mice compared to the wild type mice suggesting the role of Period genes in body mass regulation (Dallmann and Weaver, 2010). The homozygous *Clock (Δ19)* mutant mice are shown to develop hyperphagia and obesity (Turek et al., 2005) and in these mice, the diurnal feeding rhythm was severely altered. Furthermore, the Rev-erbα has been shown to be required for the lipid metabolism. The *Rev-erbα*$^{-/-}$ mice exhibit increased adiposity (Delezie et al., 2012). Moreover, the treatment with synthetic REV-ERB α/β agonists led to a decrease in obesity, plasma triglyceride and cholesterol levels and an increase in energy expenditure. Altogether, the clock genes play an important role in the metabolic diseases (Solt et al., 2012).

Several studies also highlight the role of circadian clock proteins in the regulation of cell cycle and cell cycle checkpoint pathways, oxidative stress and carcinogenesis (Antoch and Kondratov, 2010). The studies with the *Per2* mutant mice have shown that the *Per2* is involved in the regulation of DNA damage response and tumor suppression (Fu et al., 2002). Furthermore, another key circadian clock components such as *Per1* interacts with the pivotal components (ATM and Chk2 kinases) of the cell cycle checkpoint pathways and plays a role in the control of DNA damage in human cancer cells (Gery et al., 2006; Kondratov and Antoch, 2007). Another mammalian circadian clock protein Timeless (Tim) also interacts with the components of cell cycle checkpoint pathways such as ATR, ATR-interacting protein and Chk1 and plays a role in the DNA damage checkpoint response (Unsal-Kacmaz et al., 2005). The interaction of Tim with its interacting partner Tipin (Tim-interacting protein) enhances its stability (Chou and Elledge, 2006) and Tipin directly interacts with the replication protein A (RPA) (Gotter et al., 2007) which is involved in the DNA replication, repair and cell cycle checkpoint regulation. In the regulation of oxidative stress, *Bmal1* has been reported to play a role (Kondratov et al., 2006). As already been mentioned, *Bmal1*-deficient mice leads to accelerated aging and has been implicated to regulate the ROS homeostasis. Indeed, several tissues of *Bmal1*-deficient mice show increased levels of reactive oxygen species (ROS) and chronic oxidative stress (Kondratov et al., 2006). Furthermore, the disruptions in the circadian rhythms have been linked to the carcinogenesis (Antoch and

Kondratov, 2010) as evident by the accelerated growth of implanted tumors in mice where normal circadian rhythmicity was disrupted by the SCN ablation or by introducing experimental jet-lag (Filipski et al., 2006). *Per2* plays an important role in the inhibition of growth of cancer cells. The overexpression of *Per2* leads to the suppression of sarcoma tumors *in vivo* (Miyazaki et al., 2010) and in the *Per2*-deficient mice, the ϒ-irradiation enhances the tumor growth development and the temporal expression of genes involved in tumor suppression and cell cycle regulation gets deregulated (Fu et al., 2002). Moreover, the overexpression of *Bmal1* inhibits the proliferation of human colorectal cancer cells and increases their sensitivity to the anticancer drug Oxaliplatin *in vitro* and *in vivo* (Zeng et al., 2014), which further suggests that the regulation of the expression of circadian clock genes is linked to the carcinogenesis.

The circadian dysfunction has also been implicated to be both an effect and cause of neurodegenerative diseases (Chauhan et al., 2017). The sleep deprivation has been shown to exacerbate amyloid-β (Aβ) plaque formation and deposition in mice whereas enhanced sleep lessen the Aβ deposition (Kang et al., 2009). The amyloid-β can perturb the molecular clock as evident from disruptions in the period length in the presence of physiologically relevant amyloid-β and can also induce changes to the cellular metabolic state and circadian rhythmicity (Schmitt et al., 2017). The sleep-wake disturbances have also been associated with Parkinson's disease (PD), multiple sclerosis and Huntington's disease (HD) (Barun, 2013; Homolak et al., 2018; Hood and Amir, 2017; Ondo, 2014). A recent study showed that Aβ induces the post-translational degradation of BMAL1 and CBP leading to the modulation of PER2 expression at both mRNA and protein levels (Song et al., 2015). The disturbances in the circadian rhythmicity of body temperature and the melatonin and cortisol release have also been observed in Alzheimer's disease, PD and HD (Hood and Amir, 2017). The *presenilin-2* gene, one of the regulators of Aβ levels, is rhythmically expressed in SCN and in the peripheral tissues, its expression is regulated by CLOCK:BMAL1 via transcriptional and post-transcriptional mechanisms (Bélanger et al., 2006). Furthermore, the single nucleotide polymorphisms in *Bmal1* and *Per1* genes are associated with the increased PD risk as reported by a case-control study in Chinese population (Gu et al., 2015). Altogether, the growing research strongly suggests the implication of circadian clock in the neurodegeneration.

1.2 Brain and muscle ARNT-like protein

Brain and muscle Aryl hydrocarbon receptor nuclear translocator (ARNT)-like protein 1 (BMAL1) is the key regulator for the proper functioning of the clock, demonstrated by the loss of molecular and behavioral circadian rhythmicity and the impairment of locomotor activity in *Bmal1*$^{-/-}$ knockout mice (Bunger et al., 2000). BMAL1 interacts with CLOCK through its DNA-binding bHLH domain and the PAS domains, which are conserved in its paralog transcription factor BMAL2. *Bmal1* (also known as Mop3) is highly expressed in brain, skeletal muscle and heart (Ikeda and Nomura, 1997), while *Bmal2* (also known as Mop9) expresses predominantly in fetal brain and adult liver (Ikeda et al., 2000), suggesting that they are distinct from each other. *Bmal1* has been suggested to be epistatic to *Bmal2* (Shi et al., 2010), such that the knockout of *Bmal1* in mice leads to the downregulation in *Bmal2* levels (Bunger et al., 2000) and results in the functionally double knockout of *Bmal1* and *Bmal2* (Shi et al., 2010). The circadian behavioral and metabolic phenotypes can be partially rescued through the overexpression of *Bmal2* in the *Bmal1*-deficient mice but it does not rescue circadian rhythmicity in most tissues (Shi et al., 2010). Moreover, in the *Bmal1*$^{-/-}$ mice-derived fibroblasts expressing *Bmal1*, high amplitude oscillations of *Per2* and *Rev-erbα* mRNA expression were reported compared to the cells expressing *Bmal2*, where *Per2* and *Rev-erbα* were constitutively expressed with lower mRNA levels demonstrating the non-redundancy in functional roles of *Bmal1* and *Bmal2* and the importance of *Bmal1* as an essential clock component (Xu et al., 2015).

1.2.1 Structure of CLOCK:BMAL1 complex

The heterodimeric complex of the bHLH- and PAS domain-containing transcription factors CLOCK and BMAL1 drives the core TTFL in the mammalian circadian clock (Gekakis et al., 1998). They bind to E-box elements of the promoters of the clock-controlled genes and activate their transcription. BMAL1 consists of a basic helix-loop-helix (bHLH) domain, tandem PAS domains (PAS-A and PAS-B) and a C-terminal disordered region (Figure 1.4A). The crystal structures of the CLOCK:BMAL1 heterodimer containing the bHLH and two tandem PAS domains (PAS-A and PAS-B) (PDB ID: 4F3L) (Huang et al., 2012) and the bHLH:E-box complex (PDB ID: 4H10) (Wang et al.,

2013b) demonstrates the involvement of all three domains in the complex formation and the specificity of CLOCK:BMAL1 recruitment to E-box DNA (Figure 1.4B). The truncated CLOCK:BMAL1 bHLH-PAS-AB dimer was demonstrated to bind the oligonucleotides containing the canonical E-box DNA sequence (CACGTG) from mouse *Per1* and *Per2* promoters with high affinity (nM range) (Huang et al., 2012).

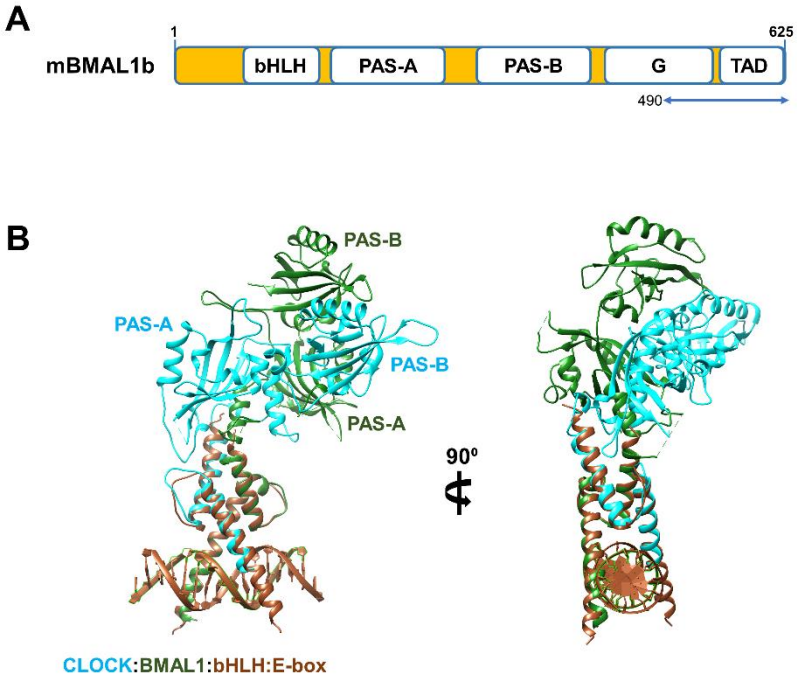

Figure 1.4. BMAL1 and the structures of CLOCK:BMAL1 complex. (A) The domain organization of mouse (m) BMAL1 (isoform mBMAL1b used herein) with a basic helix-loop-helix (bHLH) domain, two PAS (PER-ARNT-SIM) domains (PAS-A, PAS-B), the G-region (Xu et al., 2015) and a transactivation domain (TAD). The previously described (Czarna et al., 2011) ~14 kDa C-terminal BMAL1 construct- BMAL1(490-625) is represented by blue arrow. Adapted from (Garg et al., 2019) (B) The crystal structure of the human CLOCK:BMAL1 bHLH heterodimer with E-box DNA (brown; PDB: 4H10) overlaid with the crystal structure of the mouse bHLH:PAS-AB heterodimer (CLOCK, cyan; BMAL1, green; PDB: 4F3L). Note that the human CLOCK bHLH domain bound to DNA is extended by three helical turns and moved by around 5 degrees which suggests a DNA-induced conformational change. Figure adapted from (Huang et al., 2012; Wang et al., 2013b).

The structure of the CLOCK:BMAL1 bHLH-PAS-AB dimer reveals an asymmetric conformation where each domain of BMAL1 interacts with the corresponding domain of CLOCK (Figure 1.4B), so that BMAL1 bHLH interacts with CLOCK bHLH, and BMAL1 PAS-A (or PAS-B) interacts with

CLOCK PAS-A (or PAS-B). The structure of CLOCK:BMAL1 bHLH:E-Box heterodimer ($bHLH_{CLOCK}$-29-89 aa; $bHLH_{BMAL1}$-66-128 aa) also provides a basis of transcriptional regulation of CLOCK:BMAL1 by phosphorylation. The phospho-mimicking S78E mutant of BMAL1 was shown to abolish the DNA binding and downregulate the transcriptional activity of CLOCK:BMAL1 (Wang et al., 2013b). The study in this thesis is focused on deducing the lacking structural information on the C-terminal disordered region of BMAL1 and its interactions which are crucial for the regulation of CLOCK:BMAL1 transcriptional activity (Hirayama et al., 2007; Kiyohara et al., 2006; Sato et al., 2006) and will provide further mechanistic insights into the clock function.

1.2.2 The C-terminal disordered region of BMAL1 and its interaction with the CBP-KIX and CRY1

BMAL1 contains a transactivation domain (TAD) in the C-terminal disordered region (Figure 1.4A), which is required for circadian cycling. Mutations in the TAD affect the circadian period as demonstrated by the shortening or lengthening of the period upon introducing mutations in the TAD region (Xu et al., 2015). The last 43 residues within the BMAL1 TAD are required to interact with CRY1 for circadian repression as well as for transcriptional activation (Kiyohara et al., 2006; Takahata et al., 2000). The BMAL1-TAD region has been suggested to act as a regulatory switch between a transcriptionally activating 'on' mode and a repressing 'off' mode bound to co-activators or to CRY1, respectively (Kiyohara et al., 2006; Takahata et al., 2000). The BMAL1 region preceding the TAD (termed G-region, Glu429-Ile578) (Figure 1.4A) critically affects the period and the amplitude of the circadian luminescence rhythms of a $Per2^{Luc}$ reporter in rescued $Bmal1^{-/-}$ $Per2^{Luc}$ fibroblasts. The domain swapping of the entire C-terminal region (G- and TAD-regions) of Bmal2 into Bmal1 results in a loss of the ability to restore circadian rhythms of the $Per2^{Luc}$ reporter, suggesting that the C-terminus prevails the ability to functionally distinguish between the two BMAL paralogs (Xu et al., 2015). Furthermore, the mutant mice bearing a homozygous C-terminally truncated BMAL1(1-537) allele lacking the TAD and part of the G-region lose circadian rhythmicity while retaining the locomotor activity. The heterozygous mutant mice, carrying a functional WT allele and a C-terminally truncated BMAL1 allele, also displayed gradual loss of circadian rhythmicity under extended constant darkness condition (Park et al., 2015),

further demonstrating the importance of the C-terminal region of BMAL1 in the regulation of circadian rhythms.

BMAL1 is specifically acetylated at the highly conserved Lys-537 (within the BMAL1 G-region) (Figure 1.5) by its heterodimerization partner CLOCK in a daily rhythmic manner *in vivo* peaking during the repressive phase at about CT15, which enhances the BMAL1-CRY interaction and subsequent transcriptional repression of CLOCK:BMAL1 (Hirayama et al., 2007). Additionally, the BMAL1(K537R) mutant (acetylation-deficient) was demonstrated to lose the ability to rescue the circadian rhythmicity in fibroblasts derived from Bmal1$^{-/-}$ mice (Hirayama et al., 2007). Consistently, the acetyl-lysine mimetic K537Q mutation within the BMAL1 C-terminal fragment [BMAL1(490-625)], containing the TAD and the parts of the G-region (Figure 1.5), increases the binding affinity of purified BMAL1 (aa 490-625) by about 2-fold for CRY1 *in vitro* by unmasking the negative charges in the BMAL1-TAD and allowing for the electrostatic interactions with CRY1 (Figure 1.6A) (Czarna et al., 2011, 2013). The N-terminal BMAL1 regions and K537 acetylation could also allosterically affect BMAL1-TAD binding to the KIX domain, potentially through mechanisms proposed for BMAL1-TAD-CRY1 interactions (Czarna et al., 2011) (Figure 1.6A), but nothing is known so far and has been characterized in this thesis.

Interestingly, CRY1 and CBP compete for binding to the BMAL1 TAD (Xu et al., 2015). An IxxLL motif within the predicted alpha helix located in the BMAL1-TAD (residues 602-606, numbering according to BMAL1b(1-625) isoform used herein) (Figure 1.5) and the seven most C-terminal BMAL1 residues participate in binding of the Cryptochromes (CRY1/2) (Czarna et al., 2011) and of the KIX (kinase inducible domain-interacting) domain of CBP (Xu et al., 2015). The deletion of the last seven residues reduces the BMAL1-CRY1 interaction in co-immunoprecipitation studies (Kiyohara et al., 2006) and also decreases the affinity of BMAL1-TAD for CRY1 and for the KIX domain by 2-3-fold and shortens the circadian period by ~3 h. Moreover, the C-terminal insertion after Ala-600/Leu-606 within BMAL1 TAD was shown to impair circadian rhythmicity and transcriptional activation as well as reduces the interaction with CRY1 (Kiyohara et al., 2006). The double mutation L605A/L606A within the IxxLL motif disrupts the interaction of BMAL1 with KIX domain and with CRY1 and abolishes circadian cycling (Xu et al., 2015). Interestingly, distinct thermodynamic profiles have been reported for CRY1-BMAL1 (endothermic with positive

entropy change) and KIX-BMAL1 interactions (exothermic) (Czarna et al., 2011, 2013; Xu et al., 2015) suggesting the different mechanisms of binding of BMAL1 to KIX and to CRY1.

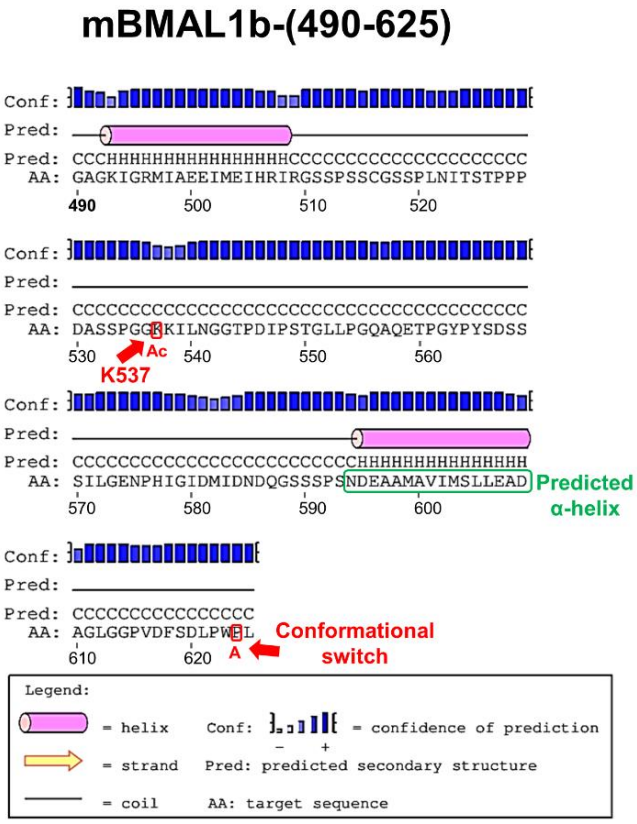

Figure 1.5. Secondary structure prediction of mBMAL1(490-625) (PSIPRED v3.3). Residues K537 (acetylated lysine) and the conformational switch within the distal C-terminus (including *trans* conformation-locking mutation P624A) are shown in red boxes. The predicted α-helical region including the KIX-binding IxxLL motif (Xu et al., 2015) is shown as green box. Figure adapted from (Garg et al., 2019).

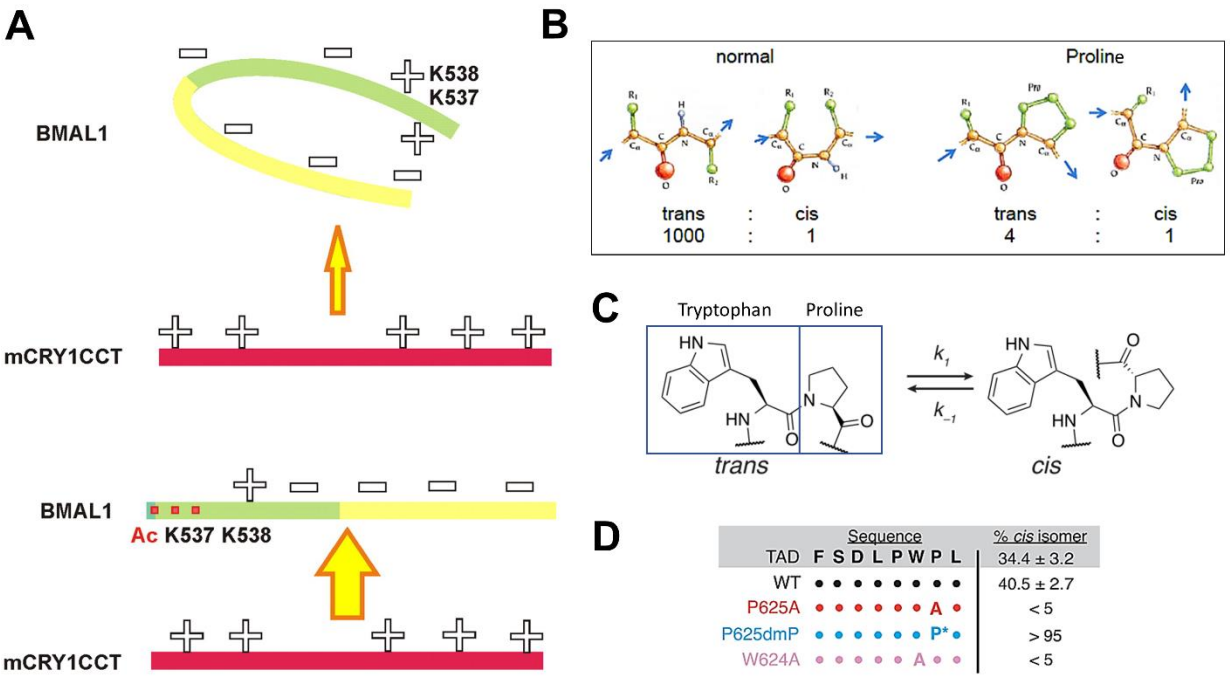

Figure 1.6. Lys-537 acetylation and the conformational switch in the BMAL1 TAD. (A) The regulation of mCRY1 binding by Lys-537 acetylation in the BMAL1 G-region. *Upper*, the negative charges in BMAL1 are masked by Lys-537 in its non-acetylated state through intramolecular interactions, thereby interfering with mCRY1 interaction. *Lower*, the negative charges in BMAL1 are unmasked by Lys-537 acetylation which enhances the binding with mCRY1 by electrostatic interactions. Source: (Czarna et al., 2011) (B) The comparison of occurrence of *cis* and *trans* amide peptide bonds with that of X-Pro imide peptide bond. The probability of occurrence of *cis*-isomer has been estimated to be between 0.1-1.5% in amide peptide bond between amino acids other than Proline. Due to the lower energy difference between *cis* and *trans* isomers for imide (X-Pro) bond, the probability was estimated to be between 30-40% for *cis*-isomer (Stewart et al., 1990). (C) The *cis* and *trans* conformations of Trp623-Pro624 imide bond within BMAL1 TAD. Source: (Gustafson et al., 2017) (D) The representation of the *cis* content of BMAL1 TAD switch peptides for P624A (numbering according to the mBMAL1b isoform used in this thesis) and W623A mutants and the bulky analog 5,5-dimethyl proline (dmP) integrated in place of P624. Source: (Gustafson et al., 2017)

1.2.3 The conformational switch within the BMAL1 distal C-terminus

In addition to the posttranslational modifications, the dynamic behavior of the proteins also play an important role in the regulation of physiological processes (Henzler-Wildman and Kern, 2007). One such dynamic behavior is *cis-trans* isomerization about X-Pro imide bond (Proline-containing imide bond) which functions in the diverse biological processes and play a regulatory role in human physiology and pathology (Gustafson et al., 2017; Lu et al., 2007). The proline isomerization (also dubbed as a ''molecular timer'' (Lu et al., 2007)) is a rare process (frequency

of about 5-6 % based on the structures deposited in Protein data bank) (Stewart et al., 1990) with minimal difference in free energy between *cis*- and *trans*- isomers unlike other amino acids, where *trans* conformation is more energetically favorable (Figure 1.6B). Proline isomerization is a slow process intrinsically which can be catalyzed by peptidyl-prolyl isomerases (PPIases) (Gustafson et al., 2017; Lu et al., 2007). Such intrinsically slow conformational switch has recently been identified to be residing in the distal C-terminus of BMAL1 TAD in the form of Trp623-Pro624 imide bond (Figure 1.5, 1.6C). The *cis*-*trans* isomerization of the BMAL1 TAD about the imide bond (termed as 'TAD switch') has been shown to modulate the mammalian circadian timekeeping (Gustafson et al., 2017) which further highlights the importance of this region in maintaining the circadian rhythmicity. The Trp and Pro of the TAD switch are highly conserved from insects to vertebrates (Gustafson et al., 2017). Locking the switch to either a *cis* or *trans* conformation by incorporating a bulky 5,5-dimethyl proline in place of Pro624 (numbering according to BMAL1b(1-625) isoform used herein) or by mutating Pro624 to Alanine, respectively (Figure 1.6D), affect the circadian period but does not alter the affinity of BMAL1 for KIX domain and for CRY1 (Gustafson et al., 2017).

1.3 KIX domain and its role in the circadian clock

The CREB-binding protein (CBP) and E1A-binding protein (p300) are paralog transcriptional regulators possessing similar multi-domain architectures (Figure 1.7A) and histone acetyltransferase activities (Dyson and Wright, 2016; Ogryzko et al., 1996; Vo and Goodman, 2001). The two proteins are commonly referred to as CBP/p300 as they significantly overlap in their functions. Using the well-folded domains, CBP/p300 interact with numerous transcriptional activators and act as the transcription hub (Giordano and Avantaggiati, 1999). Not only with the transcriptional activators, CBP/p300 also interacts with the basal transcriptional machinery such as TATA-box binding protein, TFIIB and possibly RNA polymerase II (Kee et al., 1996; Nakajima et al., 1997), thereby acting as a bridge between the transcription factors and the basal machinery (Janknecht and Hunter, 1996) and participate in the formation of the transcriptional pre-initiation complex (PIC) (Vo and Goodman, 2001). These interactions of CBP/p300 are mediated through

their multiple different domains such as nuclear receptor interacting domain (RID), interferon-binding domain (IBiD) or nuclear coactivator binding domain (NCBD), cysteine/histidine-rich regions TAZ1 and TAZ2 and the KIX domain (Figure 1.7A). In addition, CBP/p300 contains several other conserved domains such as the histone acetyltransferase (HAT) domain and the bromodomain. As the name suggests, the HAT domain possesses histone acetyltransferase activity and acetylates all four core histones in the nucleosomes (Ogryzko et al., 1996) as well as a variety of non-histone proteins such as mixed lineage leukemia (MLL) protein 1 (Aguilar-Arnal et al., 2015) and p53 (Ito et al., 2001). The bromodomain is an acetyl-lysine specific domain which recognizes acetylated histones and is required for the proper substrate targeting (Delvecchio et al., 2013). The importance of CBP/p300 is demonstrated by the embryonic lethality in mice resulting from the homozygous loss of either CBP or p300 (Kung et al., 2000; Yao et al., 1998). Moreover, CBP has been characterized as an essential regulator of hematopoietic differentiation in mice (Kung et al., 2000). Using the yeast two-hybrid system, the N-terminal fragments of CBP (452-721) and p300 (437-699) (containing the KIX domain and LXXLL motif) were identified to be sufficient to interact with BMAL1 (Takahata et al., 2000).

1.3.1 Structure and interaction partners of the KIX domain

Among multiple functional domains of CBP/p300, one of the important domains of these proteins is a highly conserved region termed as kinase-inducible domain interacting domain (KIX domain) (Figure 1.7). In mouse and humans, the KIX domain of CBP (aa 586-672) and p300 (aa 567-653) vary by 9 amino acids (Figure 1.7B) and consist of three α-helices (α1-α3) with two 3_{10} helices. The KIX domain interacts with a plethora of transcription factors such as breast cancer 1 (BRCA1), c-Jun, FOXO3a, p53, mixed lineage leukemia (MLL) protein 1, c-Myb, CREB and BMAL1 (Thakur et al., 2014) with its two distinct binding sites referred to as MLL- and c-Myb/CREB-pKID-binding sites on the basis of the specificity of transcription factors MLL and c-Myb towards each site (Table 1.1). These two binding sites are typically targeted by the intrinsically disordered regions within transcriptional activation domains (TAD) of the binding partners, which frequently include a ϕxxϕϕ motif (ϕ hydrophobic) and attain folding upon complexation (Gianni et al., 2012; De

Guzman et al., 2006; Parker et al., 1999; Radhakrishnan et al., 1997; Thakur et al., 2014; Zor et al., 2002). The interaction of the KIX domain with various transcription factors is detailed in the following sections.

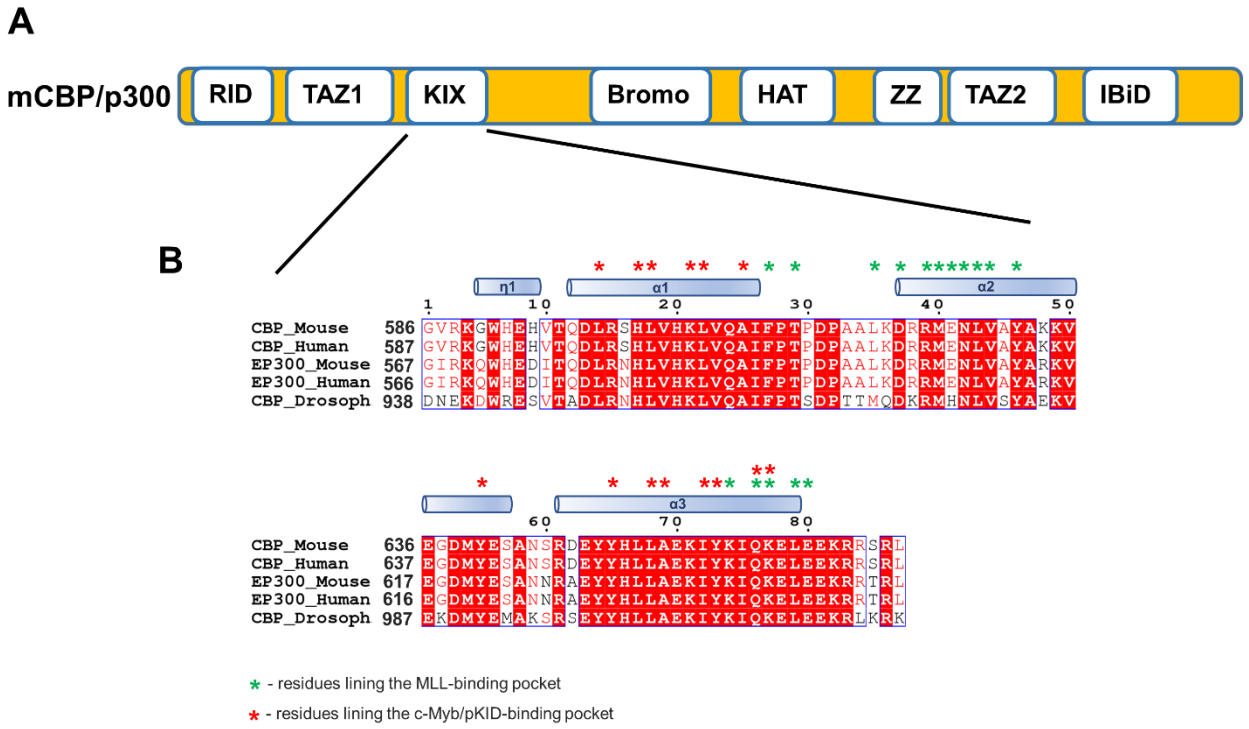

Figure 1.7. Domain architecture of CBP/p300 and sequence alignment of the KIX domain. (A) The domain architecture of mouse (m)CBP/p300 showing that it comprises of several domains such as the nuclear receptor interacting domain (RID), cysteine/histidine regions TAZ1 and TAZ2, the KIX domain, bromodomain, histone acetyltransferase (HAT) domain, ZZ-type zinc finger domain and interferon-binding domain (IBiD). (B) Sequence alignment of the conserved 87 amino acids KIX domain of CBP and p300 [denoted as E1A-binding protein (EP300)]. Residues lining the MLL- and c-Myb/pKID-binding pockets are marked with asterisk. Figure adapted from (Garg et al., 2019).

Table 1.1 The location of interaction of KIX interacting proteins*

Protein (domain)	Location of interaction within KIX domain	Source
MLL1 (TAD)	MLL-site	Ref: (Brüschweiler et al., 2013)
CREB (pKID)	c-Myb/pKID-site	Ref: (Radhakrishnan et al., 1997)
c-Myb (TAD)	c-Myb/pKID-site	Ref: (Zor et al., 2004)
p53 (AD1)	Both sites	Ref: (Lee et al., 2009)
p53 (AD2)	Both sites	Ref: (Lee et al., 2009)
FOXO3a (CR2C)	Both sites	Ref: (Wang et al., 2012)
FOXO3a (CR3)	Both sites	Ref: (Wang et al., 2012)
BRCA1 (BRCT)	c-Myb/pKID-site	Ref: (Lee et al., 2011)
c-Jun (AD)	MLL-site	Ref: (Campbell and Lumb, 2002)

*Adapted from Chelsea L Gustafson's dissertation, 2016

1.3.2 Interaction of KIX domain with MLL1, CREB and c-Myb

The activation domain of c-Myb and the Ser133-phosphorylated kinase-inducible domain (pKID) of CREB utilize the same binding pocket (around the α1 and α3 helices of KIX) for interaction with the KIX domain (Figure 1.8, 1.9), but the mechanisms of binding are proposed to be different that are reflective of their functional properties (Gianni et al., 2012; Parker et al., 1999; Radhakrishnan et al., 1997; Zor et al., 2002, 2004). The CREB-KID has only 1% helicity when unbound unlike c-Myb TAD which is already in partial (~25%) helical conformation in unbound state and both attain folding upon complexation with KIX (Gianni et al., 2012; Parker et al., 1999; Radhakrishnan et al., 1997; Zor et al., 2002, 2004). The phosphorylation of KID at Ser133 enhances its interaction with the KIX domain by ~20-fold over the non-phosphorylated state (Zor et al., 2002). The point mutations Y650A and A654W (residues are highlighted in Figure 1.8) within the shallow groove of c-Myb/pKID binding pocket significantly reduce the binding of the KIX domain to both c-Myb as well as pKID, while Y658F significantly lowers its affinity for pKID but had a minor effect on the interaction with c-Myb (Parker et al., 1999).

Other transcription factors such as MLL1 and c-Jun bind to the MLL-binding pocket within the KIX domain (Figure 1.8, 1.9) and both have been reported to form a ternary complex with pKID and KIX domain (Brüschweiler et al., 2013; Campbell and Lumb, 2002; Goto et al., 2002). Notably,

KIX can bind different transcription factors allosterically to its two binding pockets (Brüschweiler et al., 2013; Goto et al., 2002) (Figure 1.9). For example, the affinity of the Ser133-phosphorylated kinase-inducible domain (pKID) of CREB and of c-Myb to the second KIX binding pocket is enhanced upon binding of MLL1 to the MLL-pocket (Goto et al., 2002). The plasticity of the KIX domain renders it difficult for the crystallographic characterization without covalent tethering of the small molecule 1-10 to the MLL-binding pocket (Wang et al., 2013a). The 2.0 Å crystal structure of KIX(L664C)-1-10 (PDB ID: 4I9O) (Figure 1.8) further confirmed the binding of the compound 1-10 to the MLL-pocket (Wang et al., 2013a). Furthermore, tethering of the small molecule 1-10 to L664 or N627 (mutated to cysteine) on the opposite sides of the MLL-binding pocket of KIX (Figure 1.8) also significantly reduces the MLL1 binding affinity by a factor of about 100 (Wang et al., 2013a), but also imparts positive (1-10-KIX(N627C)) or negative (1-10-KIX(L664C)) cooperativity for pKID binding to the second KIX binding pocket (Wang et al., 2014). To characterize the allosteric binding mechanisms, the tethered compound and the described mutations were proven to be valuable which have been further employed in this thesis for the analyses of BMAL1-KIX interactions.

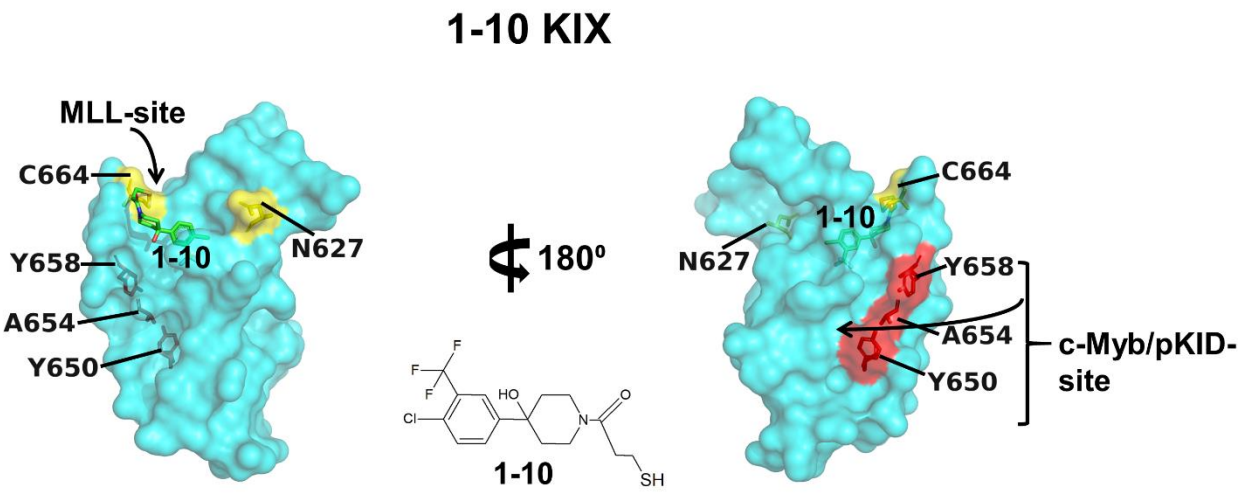

Figure 1.8. Surface representation of the 1-10 tethered KIX(L664C) structure (PDB ID: 4I9O) showing the MLL- and c-Myb/pKID-binding pockets. The key residues are shown in yellow (L664 (C664 in 4I9O) and N627 in the MLL-pocket) and red (Y650, A654, Y658 in the c-Myb/pKID-pocket). Compound 1-10 (green) is tethered to C664 (L664C) and located in the MLL-binding pocket. Figure adapted from (Garg et al., 2019).

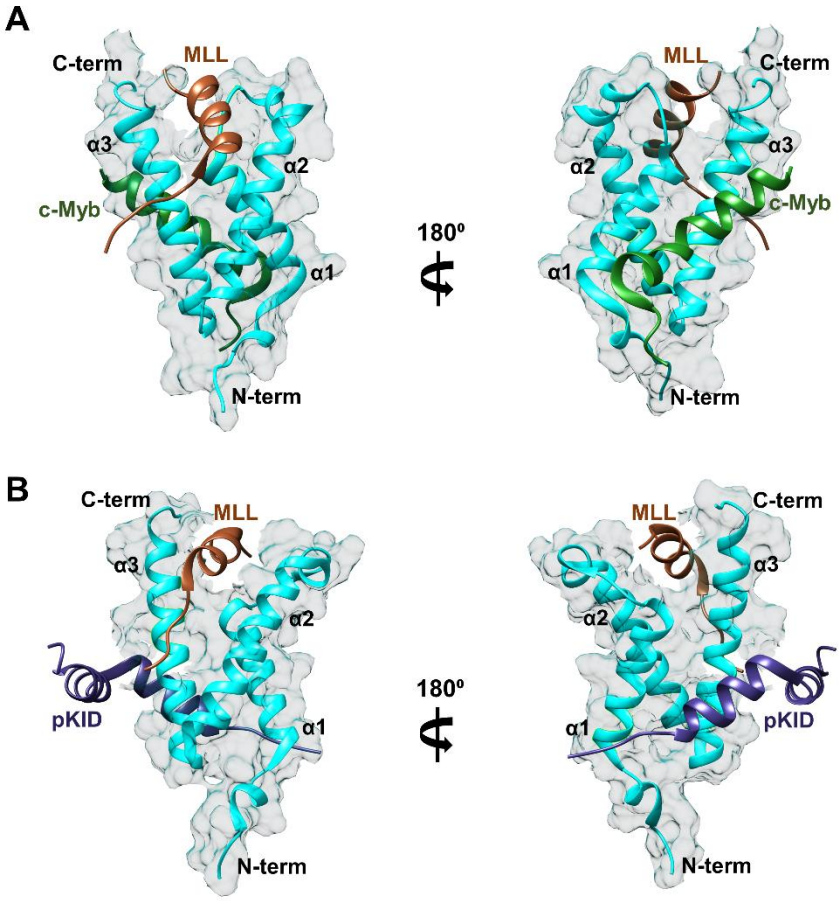

Figure 1.9. Complex of CBP-KIX domain with MLL1, c-Myb and pKID. Structure of the human CBP-KIX domain (in cyan) in complex with transactivation domains (TAD) of MLL1 (2840-2858) and c-Myb (A) and with MLL1 TAD and CREB-pKID (B) at two distinct sites. The three helices in KIX are labeled as α1, α2 and α3. Figures are based on PDB entries 2AGH and 2LXT.

1.3.3 Interaction of KIX domain with FOXO3a and p53

Unlike the specific binding of the c-Myb/pKID and MLL1 to the c-Myb/pKID- and MLL-binding pockets, respectively, the transcription factors FOXO3a (Wang et al., 2012) and p53 (Lee et al., 2009) utilize both binding pockets for interaction with KIX domain. They possess two KIX binding regions with ϕxxϕϕ motifs (ϕ denotes the hydrophobic residue) to target both, the MLL- and the pKID/c-Myb-pockets in a cooperative manner. The physical and functional interaction of p53 with CBP/p300 is required for regulation of DNA binding activity, transactivation and stability of p53

(Grossman, 2001). The transcriptional activation domain (TAD) is located in the N-terminal region of p53 and interacts with multiple domains of CBP/p300 (Ferreon et al., 2009). Herein we will discuss only the interaction of p53 with KIX domain. The p53 TAD (aa 1-61) contains two subdomains AD1 (aa 1-40) and AD2 (41-61) that interact weakly with the KIX domain (detectable only by NMR) compared to the full-length (FL) p53 TAD (K_D ~ 14-27 μM) suggesting the synergistic binding of the two subdomains to KIX (Lee et al., 2009). The binding of p53 TAD to the KIX domain results in the local helical formation within the AD1 and AD2 regions and the FL p53 TAD reportedly interacts simultaneously with both MLL- and c-Myb/pKID-binding pockets of KIX domain. Moreover, mapping of the chemical shift perturbations onto the structure of KIX domain revealed that the isolated AD1 and AD2 subdomains of p53 TAD also interact with both binding pockets of KIX domain (Lee et al., 2009).

FOXO3a contains three conserved regions (CR1-CR3) and a forkhead (FH) domain. It has been shown to interact with the KIX domain through its CR3 region and the C-terminal region of CR2 (termed CR2C), both of which are intrinsically disordered regions and shown to be involved in transactivation (Wang et al., 2012). Additionally, FOXO3a also interacts with TAZ1 and TAZ2 domains of CBP/p300 which further contribute to the transactivation (Wang et al., 2012). Both CR3 and CR2C regions contain ϕxxϕϕ motif to interact with the MLL- and c-Myb/pKID-binding pockets of KIX domain simultaneously. The fusion peptide of CR2C and CR3 (termed as CR2C-CR3) was demonstrated to bind KIX in two different orientations where CR2C occupies the c-Myb/pKID-pocket and CR3 binds to the MLL-pocket in one orientation, while CR2C binds to the MLL-pocket and CR3 binds to the c-Myb/pKID-pocket in the other orientation (PDB entries 2b3l and 2l3b) (Wang et al., 2012). These interactions were shown to deviate from that reported for the MLL1 and pKID interactions with KIX domain. Interestingly, both conformers were found to be similarly populated as shown by the similar broadening of the residues in MLL- and c-Myb/pKID-pockets in HSQC titrations. The double mutant disrupting the MLL-site (I660A/L664A) and the triple mutant disrupting the c-Myb/pKID-site (A654Q/Y650A/Y658A) moderately affect the binding affinity with CR2C-CR3 (weakened by 3-4-fold) consistent with the deviation in interactions of MLL1 and c-Myb/pKID to the respective KIX binding pockets (Wang et al., 2012).

Altogether, this provided valuable insights into the multivalent interactions between coactivators and intrinsically disordered transcription factors.

1.3.4 Interaction of KIX domain with BMAL1

The binding of the KIX domain of CBP/p300 to BMAL1 regulates the transcriptional activity of CLOCK:BMAL1 (Takahata et al., 2000). The KIX-binding regions reside within the predicted α-helix and the seven most C-terminal residues of the BMAL1-TAD (refer to section 1.2.2). The KIX domain binding to the BMAL1-TAD leads to the transcriptional activation of circadian genes by histone H3 K9/K14 acetylation (Etchegaray et al., 2003).

Multiple domains of CBP/p300 may participate in binding to BMAL1 to accentuate its recruitment to CLOCK:BMAL1 and thereby, transcriptional activation, which needs to be further explored. Furthermore, there is a requirement for the structural and mechanistic characterization of BMAL1 and CBP interactions and its potential interplay with other KIX-binding partners which is missing so far and is essential to decode the CBP interaction network as a centrepiece for the regulation of circadian phase shifting and activation of clock genes.

1.3.5 Networking of CBP, BMAL1, MLL1 and CREB in circadian gene regulation

The amount of CBP protein present *in vivo* is limiting. Therefore, binding competition of different transcriptional regulators is crucial to define and regulate the diverse biological functions of CBP (Vo and Goodman, 2001). Interestingly, the KIX ligands MLL1 and CREB also play important roles in the regulation of circadian transcription (Aguilar-Arnal et al., 2015; Katada and Sassone-Corsi, 2010; Lee et al., 2010). MLL1 co-activates circadian genes by daily rhythmic recruitment to CLOCK:BMAL1 and cyclic H3K4 trimethylation, and this MLL1 activity is further enhanced by p300/CBP-dependent acetylation of MLL1 at K1130 and K1133 nearby its CLOCK-binding site (Aguilar-Arnal et al., 2015; Katada and Sassone-Corsi, 2010). CREB-CBP interactions on the other hand are essential for light entrainment of the circadian master clock in the SCN via upregulation of the *per1* clock gene, which contains CLOCK:BMAL1- (E-box) and CREB-binding (Ca^{+2}/cAMP

regulatory elements) sites in its promoter (Gau et al., 2002; Travnickova-Bendova et al., 2002). These observations suggest a functional interplay of CBP, BMAL1, MLL1 and CREB within circadian gene regulation, chromatin modification and light entrainment, which, at a mechanistic level, is far from understood. While the KIX- and CRY-binding BMAL1-TAD regions have been described (Czarna et al., 2011; Xu et al., 2015), the binding sites of the BMAL1-TAD within the KIX domain and the interplay of BMAL1 with other KIX ligands are largely undefined.

1.4 Cryptochromes and their interaction with BMAL1

In the mammalian circadian clock, the cryptochromes (CRYs) act as the potent repressors of the transcriptional activity of the CLOCK:BMAL1 complex (Kume et al., 1999). Further, the importance of CRYs is demonstrated by the shortening or lengthening of the circadian period upon homozygous deletion of *Cry1* or *Cry2*, respectively in the transgenic mouse mutants. Furthermore, the double *Cry1*$^{-/-}$ and *Cry2*$^{-/-}$ mutant mice behave completely arrhythmically in constant darkness (Van Der Horst et al., 1999). The posttranslational modifications such as phosphorylation or acetylation and the stability, degradation and nuclear translocation regulate the repressor activity of cryptochromes. For example, phosphorylation of CRYs by mitogen-activated protein kinase (MAPK) reduces their ability to repress transcriptional activity of CLOCK:BMAL1 (Sanada et al., 2004). Further, BMAL1 acetylation at Lys537 enhances its binding affinity for CRY1 and thereby, CRY-dependent transcriptional repression (Czarna et al., 2011; Hirayama et al., 2007). The interaction of mCRY1 with mPER2 and the E3-ligase FBXL3 controls its ubiquitylation, degradation/stability and nuclear translocation (Gatfield and Schibler, 2007; Yagita et al., 2002). Furthermore, the phosphorylation of mCRY1 by AMP-activated protein kinase (AMPK) also reduces its stability by decreasing mPER2 binding and increasing FBXL3 binding (Lamia et al., 2009) suggesting that the FBXL3 and PER2 have overlapping CRY1-binding sites which were further confirmed by the crystal structures (Schmalen et al., 2014).

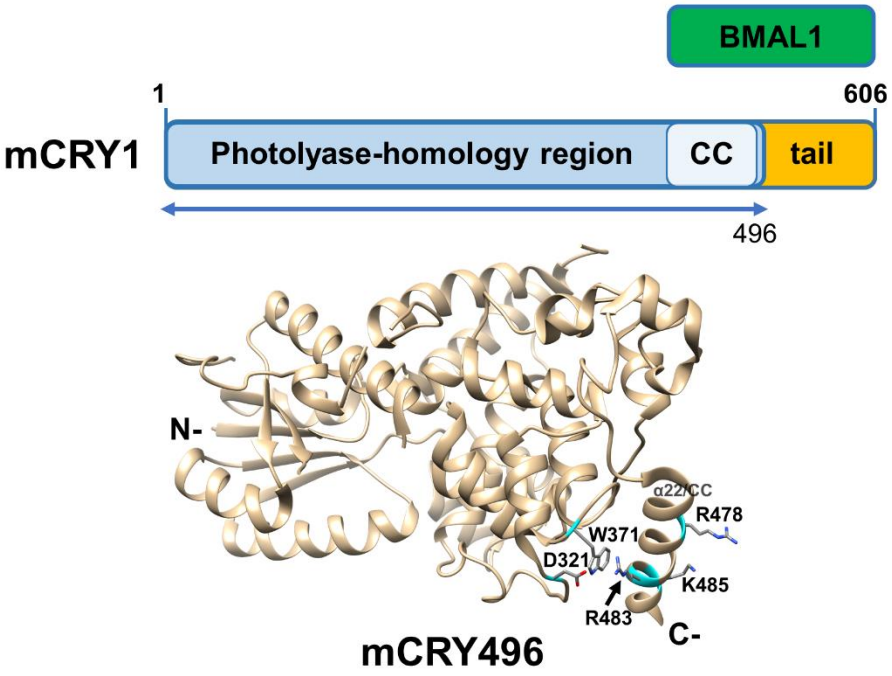

Figure 1.10. Domain architecture of mouse (m) CRY1 and crystal structure of mCRY496. (*upper)* The domain organization of mCRY1 showing the photolyase-homology region (PHR) with the coiled-coil helix (CC) and the C-terminal tail region. The tail region along with the CC-helix participate in binding to the BMAL1 TAD (Czarna et al., 2011, 2013). *(bottom)* The crystal structure of mCRY1(1-496) (= CRY1-PHR) depicted in ribbon form with the amino acid residues that interact with BMAL1 (Arg478, Arg483 and Lys485 within the α22 (CC)) and the residues (Asp321 and Trp371) that stabilize the α22 by interacting with Arg483 are shown as sticks. Figure is based on the PDB entry 4K0R (Czarna et al., 2013).

The cryptochromes contain a conserved photolyase homology region (PHR) with an N-terminal α/β domain and a C-terminal α-helical domain with a predicted coiled coil (CC) helix as well as variable C-terminal extensions (also termed as tails) (Figure 1.10) (Chaves et al., 2011; Sancar, 2003). The coiled-coil helix (CC/α22) along with the tail region is involved in the binding of BMAL1 (Czarna et al., 2011) and in the transcriptional repression of CLOCK:BMAL1 (Chaves et al., 2006). The amino acid residues R478, R483 and K485 within the α22 participate in the interaction with BMAL1 TAD (Czarna et al., 2011) and the position of α22 is stabilized by the interaction of R483 with W371 and the salt bridge formation with D321 (Figure 1.10). The Lys537 acetylation within BMAL1 G-region (Figure 1.4-1.6, section 1.2.2) unmasks the negative charges in BMAL1 and enhances its binding with the positively-charged residues within CC-helix and tail of CRY1 by electrostatic interactions (Figure 1.6) (Czarna et al., 2011). Interestingly, the PHR has

also been suggested to contribute to the BMAL1-binding demonstrated by a 10-fold increase in the affinity of full-length CRY1 for BMAL1 compared to the CRY1 CC-tail fragment (includes CC-helix and tail region) which might be due to the restructuring of the tail region by PHR (Czarna et al., 2013). In this thesis, we would aim to analyze the mBMAL1-mCRY1 interactions on the structural level. Additionally, the effect of *in vitro* $Lys537_{mBMAL1}$ acetylation on the formation of the mBMAL1:mCRY1 complex and thereby, on the transcriptional repression, will be biochemically and structurally characterized.

1.5 Aim of the thesis

The three-dimensional structures of the bHLH-PAS domains of BMAL1, the CBP-KIX domain and the CRY1-PHR (including the CC-helix) have been solved but there is no structural information available on the complex formation of the transactivation domain (TAD) of BMAL1 with the CBP-KIX domain and with full length CRY1. Furthermore, the molecular mechanisms underlying the repression and activation of transcriptional activity of BMAL1:CLOCK upon recruitment of CRY1 or CBP/p300, respectively are not fully understood. So, the first aim of the thesis was to solve the three-dimensional structure of the complexes of the BMAL1-TAD with the CBP-KIX domain and with CRY1. For this purpose, stable constructs of the C-terminal region of BMAL1 forming the complex with KIX and with CRY1 had to be defined by limited proteolysis. Additionally, protocols of expression and purification of recombinant BMAL1 proteins with varying N-terminal length preceding the TAD (including parts of G-region and Lys-537) and of their complexes with the KIX domain and with CRY1 proteins had to be established.

The second aim was to characterize the interactions of the KIX domain with BMAL1 proteins including the C-terminal TAD, parts of the G-region and Lys-537, the binding-induced folding transition of the BMAL1-TAD and the effect of the acetyl lysine mimicking $K537Q_{BMAL1}$ mutation on the BMAL1-KIX interaction. To this end, we used pull-down assays, size-exclusion chromatography, site-directed mutagenesis, static light scattering, circular dichroism spectroscopy and different affinity measurement techniques such as microscale thermophoresis, fluorescence polarization and nano-surface plasmon resonance. Further, small-angle X-ray

scattering (SAXS) was used to gain structural insights into the complex formation of BMAL1 TAD and KIX domain.

The BMAL1 TAD-binding sites within the KIX domain were to be determined based on our biochemical and structural studies. The aim was to unravel the effect on the KIX-BMAL1 TAD interactions upon tethering the KIX domain with the small compound 1-10 in the MLL-binding pocket and to find out whether BMAL1 interacts with KIX using only one or both binding pockets of the KIX domain (MLL- and pKID/c-Myb-pockets). Further, along with CBP, the coactivation of circadian genes by MLL1 via its daily rhythmic recruitment to the BMAL1:CLOCK complex and by chromatin modification has been suggested which is further enhanced by the CBP/p300-dependent acetylation of MLL1 (Aguilar-Arnal et al., 2015; Katada and Sassone-Corsi, 2010). Moreover, MLL1 interacts with CLOCK and with the KIX domain which suggested a possible interplay of BMAL1-TAD/CBP-KIX/MLL1 within circadian gene regulation which was addressed at a preliminary level by pull-down experiments of MLL1-TAD with BMAL1 and the KIX domain. Finally, the results obtained were corelated with the binding modes of other KIX-interacting partners and the CBP- and CLOCK:BMAL1-dependent circadian gene regulation.

2 Materials and Methods

2.1 Materials

2.1.1 Equipments

Instrument	Supplier
Nanodrop 2000 spectrophotometer	Thermo Fisher Scientific (Karlsruhe, Germany)
Äkta purification system	GE Healthcare (München, Germany)
NGC purifier	Bio-Rad (München, Germany)
Äkta Micro purifier	GE Healthcare (München, Germany)
Microfluidizer LM10	Microfluidics Corp (MA, USA)
Sonifier S-450A	Branson Ultrasonics (Eemsen, NL)
Monolith NT.115	NanoTemper Technologies (München, Germany)
Spark 20M plate reader	Tecan (Crailsheim, Germany)
Gel electrophoresis	Bio-Rad (München, Germany)
Mosquito	TTP Labtech Ltd (Hertfordshire, UK)
CD spectrophotometer JASCO J-815	JASCO Deutschland GmbH (Pfungstadt, Germany)
Multitron Incubator shakers	Infors GmbH (Einsbach, Germany)
Wyatt DAWN-DSP	Wyatt Technology (Dernbach, Germany)
UV-Vis Spectrophotometer Hitachi U-1100	Hitachi Europe GmbH (Düsseldorf, Germany)
RUMED crystallization incubator	Rubarth Apparate GmbH (Laatzen, Germany)

2.1.2 Softwares

Software	Developer/Supplier
PyMOL	Schrödinger, LLC, New York
UCSF Chimera	Pettersen EF *et al.*, 2004
SnapGene Viewer	GSL Biotech LLC, Chicago, USA
Vector NTI	Life Technologies, Darmstadt, Germany
Origin	Origin-Lab, Northampton, MA, USA
GraphPad Prism 5.02	GraphPad Software, San Diego, California, USA
NT Analysis	NanoTemper Technologies, München, Germany

2.1.3 Consumables and chemicals

The chemicals were purchased from Carl Roth GmbH & Co. KG (Karlsruhe, Germany), Serva (Heidelberg, Germany), Merck (Darmstadt, Germany), Sigma-Aldrich (München, Germany, now

owned by Merck group), Qiagen (Hilden, Germany), Alfa Aesar (Thermo Fisher Scientific, Karlsruhe, Germany), Roche Diagnostics (Mannheim, Germany), Hampton Research (Aliso Viejo, USA) and Fisher Scientific (Leicestershire, UK). The enzymes were purchased from Sigma-Aldrich (München, Germany), Thermo Fisher Scientific (Waltham, USA), Agilent Technologies (Waldbronn, Germany) and New England Biolabs (NEB) (Frankfurt am Main, Germany). The plasmid isolation, gel extraction and PCR purification kits were purchased from Qiagen (Hilden, Germany), Roche (Mannheim, Germany) and Macherey-Nagel (Düren, Germany). The fluorescent labeling dyes were purchased from NanoTemper Technologies (München, Germany) and Sigma-Aldrich (München, Germany). The chromatography columns and column materials were purchased were purchased from GE Healthcare (München, Germany) and Qiagen (Hilden, Germany). The ultrafiltration devices, cellulose acetate membrane filters and dialysis membranes were purchased from Merck (Darmstadt, Germany), Sigma-Aldrich (München, Germany), Sartorius Stedim Biotech (Göttingen, Germany) and Carl Roth GmbH (Karlsruhe, Germany). The insect cell and bacterial expression flasks were purchased from Corning GmbH (Kaiserslautern, Germany), Sarstedt AG (Nümbrecht, Germany) and DWK Life Sciences GmbH (Wertheim am Main, Germany). The pipette tips, falcon tubes, PCR and reaction tubes and serological pipettes were purchased from Sarstedt AG (Nümbrecht, Germany). The single channel classic pipettes were purchased from Gilson (Offheim, Germany). The cryo loops, crystallization screens, and microtools box were purchased from Hampton Research (Aliso Viejo, CA, USA), Jena Bioscience GmbH (Jena, Germany), Qiagen (Hilden, Germany) and Molecular Dimensions (Suffolk, UK).

2.1.4 Antibiotics

Name	Stock solution	Working concentration
Kanamycin	30 mg/ml	50 µg/ml
Ampicillin	100 mg/ml	100 µg/ml
Chloramphenicol	34 mg/ml	34 µg/ml
Streptomycin	50 mg/ml	50 µg/ml
Gentamicin	7 mg/ml	7 µg/ml
Tetracycline	10 mg/ml	10 µg/ml

2.1.5 Media

Medium	Cell type	Substances	For 1 L
Luria Bertani (LB)	*E. coli*	NaCl Bactotryptone Bacto-Yeast extract Adjusted to pH 7.0 with 5M NaOH	10 g 10 g 5 g
Terrific Broth (TB)	*E. coli*	Bactotryptone Bacto-Yeast extract Glycerol Phosphate buffer- K_2HPO_4 KH_2PO_4	12 g 24 g 4 g 72 mM 17 mM
SOC media	*E. coli*	NaCl $MgSO_4$ KCl $MgCl_2$ Bactotryptone Bacto-Yeast extract Glucose Adjusted to pH 7.2	10 mM 10 mM 2.5 mM 1 mM 20 g 5 g 4 g
Sf-900 II SFM	Insect Cells	Gibco's Serum-free and protein-free formulation	

2.1.6 Strains and cell lines

2.1.6.1 *E. coli* strains

Strain	Genotype	Species
DH5α	F^- ϕ80*lac*ZΔM15 Δ(*lac*ZYA-*arg*F)U169 *rec*A1 *end*A1 *hsd*R17(r_K^-, m_K^+) *pho*A *sup*E44 λ^- *thi*-1 *gyr*A96 *rel*A1	*E. coli*
BL21 DE3	F^- *omp*T *hsd*S_B (r_B^-, m_B^-) *gal dcm* (DE3)	*E. coli*
Rosetta DE3	F^- *ompT hsd*S_B(r_B^- m_B^-) *gal dcm* (DE3) pRARE (Cam^R)	*E. coli*
DH10Bac	F^- *mcr*A Δ(*mrr*-hsdRMS-*mcr*BC) ϕ80*lac*ZΔM15 Δ*lac*X74 *rec*A1 *end*A1 *ara*D139 Δ(*ara-leu*)7697 *gal*U *gal*K λ^- *rps*L *nup*G / bMON14272 / pMON7124	*E. coli*
ccdB survival	F^- *mcr*A Δ(*mrr-hsd*RMS-*mcr*BC) ϕ80*lac*ZΔM15 Δ*lac*X74 *rec*A1 *ara*Δ139 Δ(*ara-leu*)7697 *gal*U *gal*K *rps*L(Str^R) *end*A1 *nup*G *ton*A::P_{trc}-*ccd*A	*E. coli*
Omnimax	F' [*pro*AB^+ *lac*I^q *lac*ZΔM15 *Tn*10(Tet^R) Δ(*ccd*AB)] *mcr*A Δ(*mrr-hsd*RMS-*mcr*BC) ϕ80*lac*ZΔM15 Δ(*lac*ZYA-*arg*F)U169 *end*A1 *rec*A1 *sup*E44 *thi*-1 *gyr*A96 (Nal^R) *rel*A1 *ton*A *pan*D	*E. coli*
XL10 Gold	*Tetr* Δ(*mcrA*),183 Δ(*mcrCB-hsdSMR-mrr*)173 *end*A1 *sup*E44 *thi-1 rec*A1 *gyr*A96 *rel*A1 *lac Hte* [F *pro*AB *lacI*^{q}*Z*Δ*M*15 *Tn*10 (*Tet*^{r}) *Amy Cam*^{r}]	*E. coli*

2.1.6.2 Insect cell lines

Cell line	Purpose	Organism
Sf9	Suitable for transfection of bacmid DNA and isolation and propagation of recombinant baculovirus and expression of proteins	Ovarian cells from *Spodoptera frugiperda* (fall armyworm)
High Five	Baculoviral expression of recombinant proteins	Derived from the ovarian cells of *Trichoplusia ni* (cabbage looper)

2.1.7 Molecular weight standards and markers

Name	Supplier
Roti-Mark Standard Protein Marker	Carl Roth (Karlsruhe, Germany)
Roti-Mark Standard 10-150 Protein Marker	Carl Roth (Karlsruhe, Germany)
Prestained Protein Marker (10-245 kDa)	Applichem GmbH (Darmstadt, Germany)
Roti-Mark Prestained Marker	Carl Roth (Karlsruhe, Germany)
1 kb DNA ladder	Axis Bioscience Genecraft (Köln, Germany)
100 bp DNA ladder	Invitrogen (Thermo Fisher Scientific, USA)
SYBR® Safe DNA gel stain	Thermo Fisher Scientific, USA
Gel Filtration column calibration standard	Bio-Rad Laboratories, München, Germany

2.1.8 Oligonucleotides for cloning, mutagenesis and sequencing

The DNA oligonucleotides in lyophilized form were purchased from Eurofins Genomics GmbH (Ebersberg, Germany).

Nr.	Name	Type*	Sequence (5'-3')
1AG	Fw BamHI BMAL490 Amber	1	AGCCAGGATCCTCTGGAAGTTCTGTTCCAGGGGC
2AG	Rv SalI_BMAL490 Amber	1	AGCTTGTCGACTCACAGCGGCCATGGCAAG
3AG	Rv AflII_BMAL490 Amber	1	TCTGTCTTAAGTCACAGCGGCCATGGCAAG
4AG	Fw BMAL K537Q 3C	1	AAGTTCTGTTCCAGGGGCCCGGAGCAGGAAAAATAGGTCGAATG
5AG	Rv BMAL K537Q ccdb	1	CCCCAGAACATCAGGTTAATGGCGCTACAGCGGCCATGGCAAG
6AG	Fw BMAL517 3C	1	AAGTTCTGTTCCAGGGGCCCGGCTCCAGCCCGCTGAAC
7AG	Fw BMAL530 3C	1	AAGTTCTGTTCCAGGGGCCCGATGCCTCTTCTCCAGGAGGC
8AG	Rv BMAL tga ccd	1	CCCCAGAACATCAGGTTAATGGCGTCACAGCGGCCATGGCAAG

Nr.	Name	Type*	Sequence (5'-3')
9AG	Fw BMAL_1-550_3C	1	AAGTTCTGTTCCAGGGGCCCATGGCGGACCAGAGAATGGAC
10AG	Rv BMAL_1-550_ccd	1	CCCCAGAACATCAGGTTAATGGCGTCAAGTGGAAGGAATGTCTGGAGTC
11AG	Rv BMAL_1-450_ccd	1	CCCCAGAACATCAGGTTAATGGCGTCATGGGTCCCCGCCTTCCAG
12AG	Fw KIX_3C	1	AAGTTCTGTTCCAGGGGCCCGGTGTTCGAAAAGGCTGGCATG
13AG	Rv KIX_ccdb	1	CCCCAGAACATCAGGTTAATGGCGTCATAAACGTGACCTCCGCTTTTC
14AG	LP1	1	GGGCCCCTGGAACAGAACTT
15AG	LP2	1	CGCCATTAACCTGATGTTCTGGGG
16AG	Rv_MLL1_19mer	1	CCCCAGAACATCAGGTTAATGGCGTCATGGAGTATTCTTTAGTACAAAGT
17AG	Fw_MLL1_19mer	1	AAGTTCTGTTCCAGGGGCCCGACTGTGGGAATATCCTGCC
18AG	AcKRS3_fw	2	CGAACAGCAGCGTTCCGGCG
19AG	AcKRS3_rev	2	CAGAAAAAACGCCGCTGAACGCGG
20AG	DuetUP2	2	TTGTACACGGCCGCATAATC
21AG	T7_Prom	2	TAATACGACTCACTATAGGG
22AG	T7_Term	2	CTAGTTATTGCTCAGCGG
23AG	Bac 5'	2	GATTATTCATACCGTCCCAC
24AG	Bac 3'	2	CAAGTTAACAACAACAATTGC
25AG	PGEX fwd	2	GATGCGTTCCCAAAATTAGTTTGT
26AG	PGEX rev	2	GCCCTGACGGGCTTGTCTGCTCC
27AG	BMAL490_AtoT_For	3	CCTCTTCTCCAGGAGGCTAGAAGATTCTAAATGGAG
28AG	BMAL490_AtoT_Rev	3	CTCCATTTAGAATCTTCTAGCCTCCTGGAGAAGAGG
29AG	Fw_C-T_Tem BMAL	3	CTCCCCCTGATGCCTCTTCTCCAGGAGGCAAGAAG
30AG	Rv_C-T_Tem BMAL	3	CTTCTTGCCTCCTGGAGAAGAGGCATCAGGGGGAG
31AG	Fw_C-T_Mut BMAL	3	CTCCCCCTGATGCCTCTTCTCCAGGAGGCTAGAAG
32AG	Rv_C-T_Mut BMAL	3	CTTCTAGCCTCCTGGAGAAGAGGCATCAGGGGGAG
33AG	fw P624A BMAL	3	CTTTAGTGACTTGCCATGGGCGCTGTAGCGCCATTAACC
34AG	rv P624A BMAL	3	GGTTAATGGCGCTACAGCGCCCATGGCAAGTCACTAAAG
35AG	FP_KIX N627C mod	3	CATGGAGTGCCTGGTTGCCTATGCTAAGAAAGTGGAGGGAGACATG
36AG	RP_KIX N627C mod	3	CAACCAGGCACTCCATGCGGCGATCTTTCAGAGCTGCAG
37AG	FP 650YA 654AW CBP	3	TACGCTCATTTATTATGGGAGAAAATCTATAAAATACAAAAAGAACTAG
38AG	RP 650YA 654AW CBP	3	CCATAATAAATGAGCGTATTCATCCCTGCTATTAGCAG
39AG	FP_2_650YA 654AW CBP	3	GAATACGCTCATTTATTATGGGAGAAAATCTATAAAATAC
40AG	RP_2_650YA 654AW CBP	3	TAAATGAGCGTATTCATCCCTGCTATTAGCAGA
41AG	FP CBP 658YA	3	GAAAATCGCTAAAATACAAAAAGAACTAGAAGAAAAGCG
42AG	RP CBP 658YA	3	GTATTTTAGCGATTTTCTCTGCTAATAAATGATAGTATTCATCC
43AG	fw_L664C_CBP	3	CTATAAAATACAAAAAGAATGCGAAGAAAAGCGGAGGTCACG
44AG	rv_L664C_CBP	3	CGTGACCTCCGCTTTTCTTCGCATTCTTTTTGTATTTTATAG
45AG	FP_mutMLL1_CtoA	3	CTGTTCCAGGGGCCCGACGCTGGGAATATCCTGCCTTCAG
46AG	RP_mutMLL1_CtoA	3	CTGAAGGCAGGATATTCCCAGCGTCGGGCCCCTGGAACAG

*1 = For cloning, 2 = for sequencing, 3 = for mutagenesis

The SLIC overhangs complementary to 3C- and ccdb-regions are coloured in blue

2.1.9 Vectors

Vector	Organism	Fusion Tag	Protease cleavage site
pET28a	*E. coli*	N-term 6xHis	TEV
pGEX6p2	*E. coli*	N-term GST	PreScission
pCoofy1	*E. coli*	N-term 6xHis	PreScission
pCoofy3	*E. coli*	N-term 6xHis-GST	PreScission
pCoofy4	*E. coli*	N-term 6xHis-MBP	PreScission
pCDF-pylT	*E. coli*	N-term 6xHis	PreScission
pCoofy27	Insect cells	N-term 6xHis	PreScission
pCoofy28	Insect cells	N-term 6xHis-GST	PreScission
pFastBac HT B	Insect cells	N-term 6xHis	TEV

2.1.10 Cloned Plasmids

The following constructs are prepared for *E. coli* and baculoviral expression-

Insert	Vector	Primers used	Source
mBMAL1-490 (490-625) K537Q	pGEX6p2		H.Breitkreuz
mBMAL1-517 (517-625)	pCoofy1	5AG, 6AG	A.Garg
mBMAL1-517 (517-625)	pCoofy3	5AG, 6AG	A.Garg
mBMAL1-530 (530-625)	pCoofy1	5AG, 7AG	A.Garg
mBMAL1-530 (530-625)	pCoofy3	5AG, 7AG	A.Garg
mBMAL1 (490-625) K537Amber, P532S	pCoofy1_modified	4AG, 5AG	A.Garg
mBMAL1 (490-625) K537Amber, P532S	pCDF-pylT	1AG, 2AG	A.Garg
mBMAL1 (530-625) K537Q	pCoofy1	5AG, 7AG	A.Garg
mCBP (586-672) KIX	pCoofy1	12AG, 13AG	A.Garg
mCBP (586-672) KIX	pCoofy3	12AG, 13AG	A.Garg
hMLL1-19mer (2840-2858)	pCoofy3_modified	16AG, 17AG	A.Garg
hMLL1-19mer (2840-2858)	pCoofy4	16AG, 17AG	A.Garg
mCRY1 FL N-term His	pFastBac HT B		H.Breitkreuz
mCRY1 (1-496) C-term His	pFastBac		I.Schmalen
mCRY1 (1-496) N-term His	pFastBac		I.Schmalen

2.2 Methods

2.2.1 Cloning procedures

DNA templates

The plasmid carrying the gene corresponding to the full-length mouse CBP (Plasmid # 32908) was purchased from Addgene (MA, USA). The BMAL1 constructs were subcloned from mouse BMAL1(490-625). The full-length human MLL1 gene was generously gifted by Prof. Rolf Marschalek, Goethe-University of Frankfurt, Germany. The plasmids pCDF-pylT and pBK-AcKRS-3 for BMAL1 acetylation were kindly provided by Dr. Jason Chin, MRC Laboratory of Molecular Biology, Cambridge, UK.

Cloning in pCoofy vectors

The cloning in pCoofy vectors is based on sequence ligation-independent cloning (SLIC) (Li and Elledge, 2007) utilizing the principle of *in vitro* homologous recombination which relies on annealing of single-stranded DNA overhangs in insert and vector. The pCoofy series of vectors are tailor-made pETM, pTT and pFastBac vectors generated by the core facility at Max Planck-Institute of Biochemistry, Martinsried and carry a 3C (PreScission) protease-cleavage site and a toxic ccdB gene which also serve as the binding sites for primers. The ccdB technology (Bernard et al., 1994) helps in achieving zero background from the colonies carrying the parental vector.

Polymerase chain reaction (PCR) for vector linearization

For SLIC reaction, the pCoofy vectors mentioned in the section 2.1.9 were linearized using oligonucleotides LP1 and LP2 (14AG, 15AG, Section 2.1.8) which anneal at 3C protease site and C-terminus of ccdB gene, respectively to delete the ccdB gene upon linearization and amplification. The PCR reaction and amplification program are described in Table 2.1 and Table 2.2.

After PCR amplification, 5 µl of the product was analyzed by agarose gel electrophoresis (1% w/v agarose) in 1x TAE buffer (40 mM TRIS, pH 8.0, 0.1% acetic acid, 1 mM EDTA) and the remaining was ethanol-precipitated. Briefly, the PCR product was added to 800 µl absolute

ethanol. As pellet may not be visible during further precipitation steps, 1 µl of dextran blue (0.5 % dextran blue, 0.1 M NaCl, 20 mM Na-EDTA, 20 mM TRIS, pH 7.8) was also added to stain the pellet blue. The mixture was kept at -20°C for 1-2 h or at -80°C for 20 min followed by centrifugation at 14,500 rpm for 15 min. The supernatant was discarded, and the pellet was washed with chilled 70% ethanol. The pellet was air-dried and resuspended in 30 µl ddH_20.

Table 2.1 PCR reaction for vector linearization

Component	Stock Concentration	Amount
LP1	10 µM	2 µl
LP2	10 µM	2 µl
Phusion HF Buffer	5x	10 µl
dNTP	2 mM	5 µl
Template		50-150 ng
NEB Phusion polymerase		0.5 µl
ddH_2O	make-up the volume to 50 µl	

Table 2.2 Program for PCR amplification

Step	Temperature	Time	Cycles
1.	98°C	2 min	
2.	98°C	30 sec	
3.	55°C	30 sec	
4.	72°C	30 sec per kb	30x to step 2
5.	72°C	5 min	
6.	4°C	∞	

Polymerase chain reaction for insert amplification

The specific gene of interest (GOI) was amplified using oligonucleotides with the overhangs complementary to the oligonucleotides used for vector linearization and to the overhangs generated in the vector upon linearization (section 2.1.8). The reaction was prepared and PCR-amplified as described in table 2.3 and 2.4. After amplification, 5 µl of the product was analyzed by agarose gel electrophoresis (2% w/v) and the remaining amount was either ethanol-precipitated or purified via PCR purification kit (Macherey-Nagel, Düren, Germany).

Table 2.3 PCR reaction for insert amplification

Component	Stock Concentration	Amount
Forward Primer	10 µM	2 µl
Reverse Primer	10 µM	2 µl
Phusion HF Buffer	5x	10 µl
dNTP	2 mM	5 µl
Template		50-150 ng
NEB Phusion polymerase		0.5 µl
ddH_2O	make-up the volume to 50 µl	

Table 2.4 Program for PCR amplification

Step	Temperature	Time	Cycles
1.	98°C	2 min	
2.	98°C	30 sec	
3.	50°C	30 sec	
4.	72°C	30 sec per kb	30x to step 2
5.	72°C	5 min	
6.	4°C	∞	

SLIC reaction

The linearized vector and the amplified insert were used for the SLIC reaction as described in table 2.5. The vector amount was kept constant and the amount of the insert required was calculated using the NEBiocalculator (NEB, Frankfurt am Main, Germany) or by using the ligation reaction formula-

$$Insert\ required\ (ng) = \frac{Insert}{vector} molar\ ratio \times amount\ of\ vector\ (ng) \times \frac{Insert\ size\ (kb)}{vector\ size\ (kb)}$$

The reaction was incubated for 45 min at 37°C and transformed in competent *E. coli* cells. The colonies were picked up and tested for false positives via PCR in which each colony was used as the template DNA. The positive clones were grown in SOC media and the plasmid was extracted using the plasmid isolation kit (Qiagen, Hilden, Germany) and confirmed by sequencing (GATC, Eurofins Genomics, Ebersberg, Germany).

Table 2.5 SLIC reaction

Component	Stock concentration	Amount
Linearized vector		100 ng
PCR amplified insert		calculated according to insert:vector ratio
RecA buffer	10x	1 µl
RecA	2 µg/ml	1 µl
ddH_2O	make up the volume to 10 µl	

Cloning in pCDF-pylT vector

To acetylate $K537_{mBMAL490}$, the amber mutant of mBMAL1 was cloned into pCDF vector carrying the pylT gene. The pylT gene encodes for the $tRNA_{CUA}$ amber suppressor i.e tRNA with CUA anticodon which directs the incorporation of acetyl-lysine in response to the amber codon when paired with acetyl-lysyl-tRNA synthetase (AckRS-3) (Neumann et al., 2008, 2009). For cloning, the pCDF-pylT vector was processed for 90 min at 37°C using BamHI and SalI restriction enzymes (NEB, Frankfurt am Main, Germany) for linearization as described in table 2.6. The reaction was loaded on the agarose gel (1% w/v) and the linearized vector was extracted from the gel using gel extraction kit (Macherey-Nagel, Düren, Germany). The BMAL490 amber mutant gene was amplified using oligonucleotides with the overhangs corresponding to the restriction enzymes used (Section 2.1.8, primers-1AG and 2AG). The preparation of reaction and the PCR program are described in table 2.7 and 2.8. The PCR product was digested with DpnI for 1 h at 37°C followed by purification using PCR purification kit (Macherey-Nagel, Düren, Germany). The purified insert DNA was double digested by restriction enzymes BamHI and SalI for 90 min at 37°C as described in table 2.9 and the reaction was further purified using PCR purification kit.

Table 2.6 Vector processing using restriction enzymes

Component	Stock Concentration	Amount
Vector		2 µg
BamHI		1 µl
SalI		1 µl
CutSmart buffer	10x	5 µl
ddH_2O	make-up the volume to 50 µl	

Table 2.7 Insert PCR amplification

Component	Stock Concentration	Amount
Primer BamHI (1AG)	10 µM	2 µl
Primer SalI (2AG)	10 µM	2 µl
Phusion HF Buffer	5x	10 µl
dNTP	2 mM	5 µl
Insert template		50-150 ng
NEB Phusion polymerase		1 µl
ddH_2O	make-up the volume to 50 µl	

Table 2.8 PCR protocol for insert amplification

Step	Temperature	Time	Cycles
1.	98°C	2 min	
2.	98°C	30 sec	
3.	55°C	30 sec	
4.	72°C	30 sec per kb	30x to step 2
5.	72°C	5 min	
6.	4°C	∞	

Table 2.9 Double digestion reaction for amplified insert

Component	Stock Concentration	Amount
PCR amplified insert		1 µg
BamHI		1 µl
SalI		1 µl
CutSmart buffer	10x	5 µl
ddH_2O	make-up the volume to 50 µl	

The processed vector and insert were used for the ligation reaction as described in table 2.10. The amount of vector used for the reaction was kept constant and the required amount of insert was calculated using NEBiocalculator. The reaction mixture was incubated overnight (~17 h) at 16°C and transformed into the competent *E. coli* cells. The colonies were tested, and the positive clones were picked, and the plasmid was isolated as described above. The clones were confirmed by sequencing (GATC, Eurofins Genomics, Ebersberg, Germany).

Table 2.10 Ligation reaction

Component	Stock concentration	Amount
Processed vector		100 ng
Processed insert		calculated according to insert:vector ratio
Ligase buffer	10x	2 µl
T4 DNA Ligase (NEB)	2 µg/ml	1 µl
ddH_2O	make up the volume to 20 µl	

Transformation of competent cells

The *E. coli* cells were made transformation-competent using buffers TFBI (100 mM RbCl, 50 mM $MnCl_2$, 30 mM potassium acetate, 10 mM $CaCl_2$, 15% glycerol, adjusted to pH 5.8 and sterile-filtered) and TFBII (10 mM MOPS, 10 mM RbCl, 75 mM $CaCl_2$, 15% glycerol, adjusted to pH 6.8 with KOH and sterile filtered) using the protocol described in the QIAgenes *E. coli* handbook (Qiagen) and stored at -80°C. Prior to DNA transformation, the cells were thawed on ice and 50-150 ng of plasmid were added to 50 µl competent *E. coli* cells. The mixture was incubated for 30 min on ice followed by the heat shock at 42°C for 45 sec and further kept on ice for 5 min. The cells were grown in 800 µl of SOC medium at 37°C for 1 h followed by centrifugation at 6,000 rpm for 5 min. The pellet was resuspended in ~200 µl of SOC media and spread on plates containing LB agar and the appropriate antibiotic (Section 2.1.4) and incubated over night at 37°C.

2.2.2 Site-directed mutagenesis

In site-directed DNA mutagenesis, the specific targeted DNA sequence is changed via substitutions, insertions or deletions of the individual nucleotide (point mutation) or multiple nucleotide changes by appropriate synthetic oligonucleotides containing the desired mutation, while the complete double-stranded circular plasmid is amplified by means of a DNA polymerase. The mutagenesis PCR was carried out according to the modified quick-change method (Liu and Naismith, 2008) using the primers containing primer-primer (pp) complementary sequences at 5' end and the extended non-overlapping (no) sequences at 3' end. The desired mutation can either be introduced through the non-overlapping sequence or the primer complementary sequence.

The mutagenesis primers were designed according to the melting temperature (T_m) calculation using SnapGene Viewer (GSL Biotech LLC, Chicago, USA) which uses the nearest neighbor thermodynamic algorithm (SantaLucia and Hicks, 2004). Here, we used the Pfu Ultra DNA Polymerase (NEB, Frankfurt am Main, Germany) with the appropriate buffer. The PCR reaction setup and the program used are described in table 2.11 and 2.12. The PCR product is digested with DpnI for 2 h at 37°C for the removal of parental DNA template and transformed in competent *E. coli* cells as described in the above section. The colonies were picked and grown in SOC media. The plasmid is isolated using plasmid isolation kit (Qiagen, Hilden, Germany) and confirmed by sequencing (GATC, Eurofins Genomics, Ebersberg, Germany).

Table 2.11 PCR reaction for mutagenesis

Component	Stock Concentration	Amount
Forward Primer	100 µM	1 µl
Reverse Primer	100 µM	1 µl
Pfu Ultra AD Buffer	10x	5 µl
dNTP	2 mM	5 µl
Template		100 ng
Pfu Ultra polymerase		1 µl
ddH_2O	make-up the volume to 50 µl	

Table 2.12 PCR program for mutagenesis

Step	Temperature	Time	Cycles
1.	95°C	5 min	
2.	95°C	1 min	
3.	$(T_m\text{-}5°C)_{no}$	1 min	
4.	72°C	15 min	16x to step 2
5.	$(T_m\text{-}5°C)_{pp}$	1 min	
6.	72°C	30 min	
7.	4°C	∞	

2.2.3 Insect cell culture

Bacmid preparation

For protein expression in the insect cells, we used Bac-to-Bac baculovirus expression system (Invitrogen, Darmstadt, Germany) based on the site-specific transposition properties of the Tn7 transposon. The mouse CRY1 clones in pFastBac were obtained from Helena Breitkreuz and Ira Schmalen (Wolf's lab) and the mouse BMAL1 genes were cloned in pCoofy27 and pCoofy28 (section 2.1.9) which are the tailor-made pFastBac vectors as described in section 2.2.1. The pFastBac vectors contain an expression cassette under the control of the *Autographa californica* multiple nuclear polyhedrosis virus polyhedrin promoter for high-level expression and include a mini-Tn7 transposition element. The transformation of pFastBac plasmid into the competent *E. coli* cells of strain DH10Bac (Invitrogen, Karlsruhe) allows the integration of the gene via transposition mechanisms with the bacmid DNA present in these cells (Luckow et al., 1993). The DH10Bac cells contain the bacmid DNA (bMON14272) (includes the DNA segment encoding for lacZα with the mini-attTn7 attachment site and the kanamycin resistance marker) and the helper plasmid which encodes for the transposase and provide the transposition proteins during transposition reaction. The recombinant bacmid DNA is generated by transposition of the mini-Tn7 element (from pFastBac plasmid) to the attachment site (on bacmid DNA), which introduces the expression cassette upstream of the lacZα gene. As a result, expression of the lacZα gene is interrupted, which is determined by the blue/white selection. In the still intact lacZα gene, the beta-galactosidase enzyme processes the chromogenic substrate X-Gal in the presence of inducer IPTG, thereby producing a blue compound. The white colonies contain the bacmid DNA with successful transposition of the target gene and disruption of the lacZα gene. The pFastBac plasmid was transformed as described in section 2.2.1 with the appropriate antibiotics followed by a 4 h incubation (180 rpm, 37°C). Subsequently, the pellet is resuspended in the SOC media after centrifugation, diluted in 1:10, 1:100 and 1:1000 ratio with SOC media and plated on DH10Bac LB selection plates (1% Tryptone, 0.5% Yeast extract, 1% NaCl, 1.5% Agar, 50 µg/ml kanamycin, 7 µg/ml gentamicin, 10 µg/ml tetracycline, 100 µg/ml X-Gal, and 40 µg/ml IPTG). The blue and white colonies could be distinguished after a 48-h incubation period.

To verify the white phenotype after blue-white selection, 5 white colonies per batch and a blue colony (as a negative control) were streaked on a DH10Bac LBS plate with a sterile 10 µl pipette tip. The pipette tip was then placed in 5 ml SOC media with appropriate antibiotics and grown overnight (~ 17 h) at 37°C. The recombinant bacmid DNA was isolated by isopropanol precipitation. The buffers from plasmid miniprep kit (Qiagen) were used for bacmid isolation. Specifically, the overnight culture was centrifuged at 4,000 rpm for 10 min and each cell pellet was gently resuspended in 300 µl of P1 buffer and transferred to the 1.5 ml tubes. Subsequently, 300 µl of P2 buffer was added and the tubes were gently inverted for around 5 times to allow the alkaline lysis of the bacterial cells. If the P1 buffer contains lysis blue, the sample will turn blue. The reaction was neutralized with the addition of 300 µl of N3 buffer which resulted in the formation of the white precipitate. The tubes were gently inverted until the blue colour has disappeared followed by centrifugation at 14,000 rpm for 15 min and the supernatant was carefully transferred to the new 2 ml tubes. The 700 µl of 100% isopropanol was added to the tubes containing the supernatant and gently inverted. This was followed by a centrifugation step at 14,000 rpm for 10 min. After decanting the supernatant, the DNA pellet was washed with 200 µl cold 70% ethanol. After another centrifugation step for 5 min at 14,000 rpm, the supernatant was completely removed with a pipette, the pellet was air-dried under the sterile bench and resuspended in 20 µl of filter sterile water by tapping 10 times on the sterile bench. The isolated bacmids were immediately used for transfection in insect cells.

Generation and amplification of baculovirus stocks

The first recombinant baculovirus was generated by transfection of recombinant bacmid DNA into the insect cells. The virus was amplified and used for infecting the insect cells to produce recombinant protein on large-scale. Specifically, the isolated bacmid DNA was mixed with 200 µl Sf-900 II medium and 3 ml/well of total $1x10^6$ Sf9 insect cells were allowed to adhere for 15 min at 27°C in a 6-well plate (Greiner) for each clone in duplicate. The 100 µl of Sf-900 II medium was mixed with 10 µl of Cellfectin II transfection reagent (Invitrogen) and added to tubes containing the bacmid DNA. Then, mixture of the bacmid DNA and transfection reagent is divided in two

parts and added drop-by-drop to each well. The plate is incubated for 48-60 h at 27ºC and the supernatant containing baculoviral particles was collected from the wells. This baculovirus stock (P1) was used for the viral amplification to obtain higher titer virus (section 2.2.4).

2.2.4 Protein expression and purification

2.2.4.1 Protein expression in insect cells

For protein expression in insect cells, the P1 baculovirus was amplified to obtain high titer virus.

Full-length mouse CRY1

For expression of full-length mouse CRY1, a two-stage viral amplification was performed (termed P2 and P3). The 10 ml of Sf9 cells ($1x10^6$ cells/ml) were infected with 1 ml of P1 baculovirus in 100 ml Erlenmeyer flask. The flask was shaken (27ºC, 90 rpm) until the day of proliferation arrest (DPA) which is determined by arrest in growth of the cells (usually within 24 h of infection) and the virus P2 was collected after 60-72 h of attaining DPA and used for further amplification. The 250 ml of Sf9 cells at the density of $0.4x10^6$ cells/ml were infected with 500 µl of P2 baculovirus and shaken at 27ºC for 96 h followed by centrifugation at 2,000 rpm for 15 min. The P3 virus was collected from the supernatant and used for expression test and large-scale expression and purification.

The required amount of P3 virus was determined by infecting 10 ml High Five cells ($1x10^6$ cells/ml) with varied amounts of P3 baculovirus at 27ºC as described in table 2.13. The cells were harvested after 72-96 h after infection and loaded on SDS-PAGE and stained with Coomassie blue for visualization (section 2.2.7).

For large-scale recombinant protein expression, upto 1.5 L of High Five cells ($1x10^6$ cells/ml) were infected with ~15 ml of P3 virus in 3 L Fernbach flasks (Corning) and the cells were grown at 27ºC, 90 rpm for 72 h. The cells were harvested by centrifugation (4,000 rpm, 5 min) and the pellet was snap-frozen in liquid nitrogen and stored at -80ºC until further use.

Mouse CRY1-(1-496)

For expression of the C-terminally truncated mouse CRY1, only one-stage amplification of baculovirus was performed as the virus obtained was of sufficiently high titer to induce protein expression. For viral amplification, 50 ml Sf9 cells ($0.3x10^6$ cells/ml) were infected with 500 µl P1 baculovirus in a 250 ml Erlenmeyer flask and shaken for 96 h at 27°C. The cells were centrifuged and supernatant containing P2 baculovirus was collected and stored at 4°C until further usage.

For determination of optimal P2 virus required for protein expression, 50 ml High Five cells ($0.5x10^6$ cells/ml) were infected with three different amounts of P2 virus (100 µl, 200 µl and 400 µl, table 2.13) followed by shaking at 27°C for 72-96 h. The samples were taken from the expression flasks after every 24 h and analyzed by SDS-PAGE. The large-scale protein expression was carried out by baculoviral infection at 400 µl P2 virus/100 ml of High Five cells. The cells were grown for 72 h (27°C, 90 rpm) and harvested by centrifugation at 4,000 rpm for 5 min. The pellet was frozen in liquid nitrogen and stored at -80°C until further usage.

Table 2.13 Defining optimal viral amounts required for protein expression

Construct	Final viral stock	Condition	Amount
mCRY1 FL	P3 virus	1:100	50 µl
		1:100	500 µl
		undiluted	50 µl
		undiluted	250 µl
		undiluted	500 µl
		undiluted	1 ml
mCRY1-(1-496)	P2 virus	undiluted	100 µl
		undiluted	200 µl
		undiluted	400 µl

2.2.4.2 Protein expression in *E. coli*

For analysis of the protein expression and solubility, a small-scale expression test was carried out wherein the expression *E. coli strains* (BL21 DE3 or Rosetta DE3, section 2.1.6), temperature and media were varied. The 30 ml TB medium or LB medium supplemented with appropriate

antibiotics was inoculated with 1 ml pre-culture (grown overnight from freshly transformed colonies) and grown at 37°C until the absorbance at 600 nm reaches ~0.6-0.8. The protein expression was induced with 0.1 mM or 0.5 mM isopropyl 1-thio-β-D-galactopyranoside (IPTG) and expression temperatures were varied for test expression (18°C, 25°C or 30°C). The final expression conditions for large-scale protein expression are described in table 2.14.

The large-scale recombinant protein expression was carried out as described for the expression tests. Specifically, 5 L Erlenmeyer flasks were used, and 2 L TB medium was inoculated with 30 ml overnight grown pre-culture.

Table 2.14 Final conditions for large-scale protein expression

Construct	Expression strain	Expression condition
GST-BMAL1-(490-625)	BL21 DE3	30°C, 4-5 h, 0.1 mM IPTG
GST-BMAL1-(490-625)K537Q	Rosetta DE3	18°C, 16-18 h, 0.1 mM IPTG
GST-BMAL1-(490-625)P532S	Rosetta DE3	18°C, 16-18 h, 0.5 mM IPTG
His-BMAL1-(490-625)	Rosetta DE3	18°C, 16-18 h, 0.5 mM IPTG
His-BMAL1-(490-625)K537Q	Rosetta DE3	18°C, 16-18 h, 0.5 mM IPTG
His-BMAL1-(517-625)	Rosetta DE3	30°C, 4-5 h, 0.5 mM IPTG
His-BMAL1-(530-625)	Rosetta DE3	30°C, 4-5 h, 0.5 mM IPTG
His-BMAL1-(530-625)P624A	Rosetta DE3	30°C, 4-5 h, 0.5 mM IPTG
His-KIX	Rosetta DE3	25°C, 4-5 h, 0.5 mM IPTG
His-KIX L664C	Rosetta DE3	25°C, 4-5 h, 0.5 mM IPTG
His-KIX N627C	Rosetta DE3	25°C, 4-5 h, 0.5 mM IPTG
His-KIX Y658A	Rosetta DE3	25°C, 4-5 h, 0.5 mM IPTG
His-KIX Y650A A654W	Rosetta DE3	25°C, 4-5 h, 0.5 mM IPTG
His-GST-MLL19	Rosetta DE3	25°C, 4-5 h, 0.5 mM IPTG
KIX-MLL19	Rosetta DE3	25°C, 4-5 h, 0.5 mM IPTG

2.2.4.3 Protein purification

All purification steps were carried out using Äkta purification system (GE Healthcare) and NGC purifier (BioRad). The cold temperature (typically 4°C) was maintained throughout the lysis and purification procedures. The identity of the proteins was confirmed by Mass spectrometry (Proteomics core facility, IMB Mainz).

Purification of BMAL1-(490-625):KIX complex

The individual cell pellets of recombinantly overexpressing His_6-KIX or GST-BMAL1-(490-625) were homogenously resuspended in lysis buffer (50 mM Tris-Cl, pH 7.2, 250 mM NaCl, 10% Glycerol, 5mM β-Mercaptoethanol and 20 mM Imidazole) and mixed together. Prior to lysis, 1 mM phenylmethylsulfonyl fluoride (PMSF), 2 µg/ml DNase I (Sigma) and powdered lysozyme were added, and the cells were lysed using microfluidizer (Microfluidics Corp LM10, 3x 12,000 psi). The lysate supernatant after the centrifugation (19,000 rpm, 30 min) was loaded on a 5 ml Ni^{+2} sepharose affinity column (HisTrap FF, GE Healthcare) with a flow rate of 1.5 ml/min. The column was washed with 10 column volumes (CV) of wash buffer (50 mM Tris-Cl, pH 7.2, 250 mM NaCl, 5% glycerol, 5 mM β-Mercaptoethanol (β-Me) and 20 mM imidazole) followed by 5-10 CV of high-salt wash (wash buffer+750 mM NaCl) and 5-10 CV of lysis buffer. The protein complex was eluted with a 100 ml linear gradient of 20-500 mM imidazole and 1 ml fractions were collected which were analyzed by SDS-PAGE. After analysis, the fractions were pooled and tags were cleaved by overnight (~17 h) incubation in batch at 4°C with 1:100 (w/w, protease:protein ratio) PreScission protease. The cleaved protein was loaded on a 5 ml GSTrap FF column (GE Healthcare) to trap GST and the flow through was collected. After loading, the column was washed with 10 CV of lysis buffer and GST was eluted from the column using 20 mM glutathione. The flow through collected was concentrated by ultrafiltration concentrator (Merck) with a cut-off of 3 kDa and further subjected to size-exclusion chromatography using Superdex 75 16/60 column (GE Healthcare) pre-equilibrated with the SEC buffer (25 mM HEPES, pH 7.2, 2 mM DTT, 40 mM NaCl and 5% glycerol) and 1 ml fractions were collected. The protein fractions were analyzed by SDS-PAGE and GST contamination was further cleaned up using multiple GSTrap columns before concentrating by ultra-filtration followed by snap freezing in liquid nitrogen and stored at -80°C until further use.

To avoid multiple GST clean-up steps, both KIX and BMAL1-(490-625) constructs were recombinantly overexpressed as hexahistidine tag-fused proteins. The buffers used are described above. Briefly, after lysis and centrifugation, the lysate was loaded on a 5 ml HisTrap FF column and the protein complex was eluted using a 100 ml linear gradient of 20-500 mM imidazole. The tags were cleaved by overnight incubation with 1:100 (w/w) PreScission protease (for His_6-KIX)

and 1:70 (w/w) of TEV (Tobacco Etch Virus) protease (for His_6-BMAL1-(490-625)). The cleaved protein was concentrated with ultrafiltration concentrator (3 kDa cutoff) and further cleaned up using size-exclusion chromatography pre-equilibrated with the SEC buffer. The purified protein complex was snap-frozen in liquid nitrogen and stored at -80°C.

Purification of BMAL1-(530-625) and mutants

This protocol applies to wild-type BMAL1-(530-625) and BMAL1-(530-625)P624A mutant. The cell pellets overexpressing the His-tagged BMAL1 constructs were homogenously resuspended in lysis buffer (50 mM Tris, pH 7.2, 250 mM NaCl, 10% glycerol, 20 mM imidazole and 5 mM β-Me) supplemented with 1 mM PMSF, 0.5 mM AEBSF, benzonase nuclease (Protein production core facility, IMB Mainz) and lysozyme and lysed by sonication (Branson sonifier S-450A, 9 mm tip, 50% amplitude, output power 5, 4x) with constant stirring at 4°C. The cell lysate was centrifuged (19,000 rpm, 30 min) and loaded on a 5 ml Ni^{+2} sepharose column. The column was washed with wash buffer (25 mM Tris, pH 7.2, 5% glycerol, 150 mM NaCl, 20 mM imidazole and 5 mM β-Me) followed by high salt wash (750 mM NaCl) and ATP wash (wash buffer supplemented with 2 mM ATP, 50 mM KCl and 10 mM $MgSO_4$). The column was washed again with wash buffer before eluting the protein with a 100 ml linear gradient of 20-500 mM imidazole. The His-tag was cleaved with PreScission protease in a 1:50 (w/w) protease-to-protein ratio overnight at 4°C during dialysis against the dialysis buffer (50 mM Tris, pH 7.5, 100 mM NaCl, 5 mM β-Me, 5% glycerol). For dialysis, 3 kDa cutoff dialysis membrane (Carl Roth) was used. The proteins were left uncleaved for assays where the His-tag was required. After dialysis, the protein was loaded on a second HisTrap column to trap the protease, cleaved tag and uncleaved fusion protein) and the flow through was collected. The flow through was loaded on a 5 ml Q-Sepharose anion-exchange column (HiTrap Q HP, GE Healthcare), washed with AEX buffer A (50 mM Tris, pH 7.5, 50 mM NaCl, 5% glycerol and 5 mM β-Me) and eluted with a 100 ml linear gradient to 1 M NaCl. The protein was finally purified by SEC (Superdex 75 16/60, GE Healthcare) using the buffer containing 25 mM HEPES pH 7.2, 100 mM NaCl and 5% glycerol. The purified proteins were snap-frozen and stored at -80°C until further use.

For purification of the BMAL1-(530-625)K537Q mutant, similar protocol was followed as described for the wild-type BMAL1 and the P624A mutant with the exception that the protein eluate from Ni^{+2} sepharose column was subjected directly for further purification by SEC (Superdex 75 16/60, GE Healthcare).

Purification of CBP KIX-(586-672) and mutants

This protocol was followed for purification of the wild-type CBP-KIX domain and the KIX(L664C), N627C, and Y658A mutants. After resuspension of the pellets overexpressing wild-type His-tagged KIX or mutants in the lysis buffer (50 mM Tris pH 7.2, 250 mM NaCl, 10% glycerol, 5 mM β-Me and 20 mM imidazole) supplemented with 1 mM PMSF, 0.5 mM AEBSF, 2 µg/ml DNase I or benzonase nuclease, and powdered lysozyme, the cells were passed through microfluidizer (LM10, Microfluidics corp.) one time at a pressure of 15,000 psi and a second time at a pressure of 12,000 psi and the lysate was clarified by centrifugation at 19,000 rpm for 30 min. The clarified lysate was loaded on a 5 ml Ni^{+2} sepharose column (HisTrap FF, GE Healthcare) and washed with 10 CV of wash buffer (50 mM Tris pH 7.2, 150 mM NaCl, 5 mM β-Me, 20 mM imidazole and 5 % glycerol) followed by 5-10 CV of high salt wash (750 mM NaCl) and 4-6 CV of ATP wash (wash buffer+2 mM ATP). Before elution, the column was washed with 5 CV of wash buffer and eluted with a 100 ml linear gradient of 20-500 mM Imidazole. The protein eluate was dialyzed against the buffer containing no imidazole (wash buffer minus imidazole) and the His_6-tag was cleaved by PreScission protease in a 1:50 (w/w) protease:protein ratio. The cleaved protein mixture was passed through a second Ni^{+2} sepharose column followed by washing with the wash buffer. The flow through and wash fractions were collected and concentrated using ultrafiltration concentrators (Merck) with a 3 kDa cutoff. For nanoSPR measurements, the protein was left uncleaved. The concentrated protein was further subjected to purification by SEC (Superdex 75 16/60 or Superdex 75 10/300, GE Healthcare) pre-equilibrated with SEC buffer (25 mM HEPES pH 7.2, 100 mM NaCl and 5% glycerol). For KIX L664C and N627C mutants, an additional 2 mM DTT was added in the SEC buffer. The purified protein was concentrated, snap-frozen and stored at -80°C.

Purification of KIX(Y650A/A654W) mutant

For purification of the His_6-tagged KIX(Y650A/A654W) double mutant, the protocol was same as described for the wild-type KIX with the exception that prior to lysis, buffer was supplemented with one tablet of EDTA-free Pierce^{TM} protease inhibitor cocktail (ThermoFisher Scientific) and 0.1% Triton X-100. For cleavage of the His-tag, eluate from the Ni^{+2} sepharose column was incubated additionally for 30 min at room temperature with the PreScission protease prior to overnight dialysis.

Purification of BMAL1-(530-625):KIX and BMAL1-(517-625):KIX complexes

The BMAL1-(530-625):KIX and BMAL1-(517-625):KIX complexes were purified by co-lysis of the cells overexpressing individual His_6-tagged BMAL1-(530-625) or BMAL1-(517-625) proteins for respective complexes together with the cells overexpressing the KIX protein. The purification procedure followed was similar as described for the KIX proteins. Briefly, prior to co-lysis, the lysis buffer (50 mM Tris, pH 7.2, 250 mM NaCl, 10% glycerol, 5 mM β-Me and 20 mM imidazole) was supplemented with 1 mM PMSF and powdered lysozyme and the resuspended cells were co-lysed using microfluidizer (2x- 15,000 psi and 10,000 psi). The clarified lysate was loaded on a 5 ml HisTrap FF column (GE Healthcare) and after following the washing steps (as outlined in KIX purification), the protein was eluted with a linear gradient to 500 mM imidazole. The tags were cleaved by adding the PreScission protease in a 1:10 protease:protein ratio during overnight dialysis against buffer containing no imidazole (wash buffer minus imidazole), and further subjected to a second Ni^{+2} sepharose column (5 ml HisTrap FF, GE Healthcare). The flow through was collected, concentrated and finally purified by SEC using a Superdex 75 16/60 column (GE Healthcare) using the buffer containing 25 mM HEPES pH 7.2, 150 mM NaCl, 2 mM DTT and 5% glycerol. The purified protein complex was used freshly for setting up the crystallization trials and remaining protein was snap-frozen and stored in -80°C until further use.

For purification of the BMAL1-(530-625)P624A:KIX and BMAL1-(530-625)P624A:KIX(L664C) complexes, similar protocol as described for the wild-type complex was followed with an exception that for co-lysis, the resuspended cells overexpressing the BMAL1-(530-625)P624A mutant were mixed with the cells overexpressing either wild-type KIX protein or KIX(L664C) mutant for the respective complexes. Same buffers were used for the purification.

Purification of MLL1-(2840-2858)

The His_6-GST-tagged MLL1-(2840-2858) was purified using the similar protocol as outlined for the KIX proteins. Briefly, the homogenously resuspended cells overexpressing the His_6-GST-MLL1-(2840-2858) protein were lysed using microfluidizer and the clarified lysate was loaded on a 5 ml HisTrap FF column (GE Healthcare) followed by washing with the wash buffer, high salt wash and ATP wash steps. The bound protein was eluted with a linear gradient to 500 mM imidazole, concentrated using ultrafiltration concentrators (Merck) with a cutoff of 10 kDa and further purified by SEC using a Superdex 75 16/60 (GE Healthcare) column pre-equilibrated with buffer containing 25 mM HEPES pH 7.2, 150 mM NaCl, 5% glycerol and 2 mM DTT). The final purified protein was concentrated, snap-frozen and stored in -80°C.

Purification of CRY1:BMAL1-(490-625)K537Q complex

The N-terminal His_6-tagged full-length CRY1 was expressed in insect cells as described in section 2.2.4.1 and His_6-BMAL1-(490-625)K537Q in *E. coli* as described in section 2.2.4.2. The cell pellets (BMAL1 = 2 x weight of CRY1) were resuspended in lysis buffer (50 mM Tris pH 7.2, 250 mM NaCl, 5% glycerol, 5 mM β-Me and 20 mM imidazole) supplemented with 1 mM PMSF and 0.5 mM AEBSF and lysed using microfluidizer. The *E. coli* cells were passed twice through the microfluidizer at a pressure of 15,000 psi and 10,000 psi. For lysis of the insect cells, buffer was supplemented additionally with 1 tablet of EDTA-free protease inhibitor cocktail (Roche) and the cells were lysed by passing thrice through the microfluidizer at a reduced pressure of 5,000 psi. The cell lysates were mixed together and clarified by centrifugation at 27,000 rpm for 45 min.

The clarified lysate was loaded on a 5 ml Ni^{+2} sepharose column (HisTrap FF, GE Healthcare) using Äkta purification system (GE Healthcare) at a slow flow rate of 1 ml/min, washed with 5-10 CV of wash buffer (50 mM Tris pH 7.2, 150 mM NaCl, 5% glycerol, 20 mM imidazole and 5 mM β-Me), 5-10 CV of high salt wash buffer (750 mM NaCl) and 5 CV of ATP wash buffer (wash buffer supplemented with 2 mM ATP). The protein was eluted from the column with a linear gradient to 500 mM imidazole. The eluate was diluted 10 times with no salt buffer (50 mM Tris pH 7.5, 5% glycerol and 2 mM DTT) and loaded on an anion exchange column (5 ml Q HP, GE Healthcare). The AEX was performed along a 100 ml linear gradient of 25 mM to 1M NaCl and the complex was eluted at the conductivity of ~ 17.5 mS/cm. The pure fractions were pooled, concentrated using ultrafiltration concentrator (50 kDa cutoff, Merck) and subjected to SEC using a Superdex 200 16/60 column (GE Healthcare) using the SEC buffer (25 mM HEPES pH 7.2, 150 mM NaCl, 2 mM DTT, and 5% glycerol). Finally, the pure protein complex was concentrated, snap-frozen and stored in -80°C.

2.2.5 Column calibration

The SEC columns (Superdex 75 16/60, Superdex 75 10/300, Superdex 200 16/60 and Superdex 200 10/300, GE Healthcare) were calibrated using gel filtration molecular weight standard (Bio-Rad, München, Germany): Thyroglobulin (670 kDa), bovine γ-globulin (158 kDa), chicken ovalbumin (44 kDa), equine myoglobin (17 kDa) and Vitamin B12 (1.35 kDa).

2.2.6 Protein purity and concentration

Assessment of the purity of proteins was based on SDS-PAGE analysis and the ratio of absorbance at 260 nm and 280 nm (A_{260}/A_{280}) determined during SEC and concentration measurement from NanoDrop spectrophotometer. The extinction coefficients were calculated using ProtParam webserver and the protein concentrations were determined by absorbance at 280 nm and extinction coefficients.

2.2.7 Polyacrylamide gel electrophoresis

For analysis of the proteins, sodium dodecyl sulphate-polyacrylamide gel electrophoresis (SDS-PAGE) was used. For this purpose, either conventional gels (Tris-SDS gels) or 10% Bis-Tris gels were used as described in the table 2.16 and 2.17. The conventional gels were run using 1x Tris-glycine buffer and Bis-Tris gels were run using either 1x MES or MOPS buffer (table 2.15) for efficient low-molecular weight or high-molecular weight proteins separation, respectively.

Table 2.15 SDS-PAGE Buffers

Running Buffer	Composition
1x MES (final pH: 7.3)	50 mM MES
	50 mM Tris
	0.1% SDS
	1 mM EDTA
1x MOPS (final pH: 7.7)	50 mM MOPS
	50 mM Tris
	0.1% SDS
	1 mM EDTA
1x Tris-glycine (final pH: 8.3)	25 mM Tris
	192 mM Glycine
	0.1% SDS

Table 2.16 Recipe for ten 10% Bis-Tris gels

Component	Stacking gel (4%)	Resolving gel (10%)
1 M Bis-Tris, pH 6.7	5 ml	18 ml
30% Acrylamide-bisacrylamide	2.66 ml	20 ml
10% APS	160 µl	360 µl
TEMED	20 µl	30 µl
ddH_2O	12.16 ml	22 ml

Table 2.17 Recipe for two Tris-SDS gels

Component	Stacking gel 4%	Resolving gel (for 2 gels)				
		10%	12%	14%	16%	18%
ddH_2O	5.98 ml	4 ml	3.33 ml	2.66 ml	2.0 ml	1.33 ml
1.5 M Tris-Cl, pH 8.8		2.5 ml	2.5 ml	2.5 ml	2.5 ml	2.5 ml
1 M Tris-Cl, pH 6.8	2.5 ml					
30% Acrylamide-bisacrylamide	1.33 ml	3.33 ml	4 ml	4.66 ml	5.33 ml	6 ml
10% SDS	100 µl	100 µl	100 µl	100 µl	100 µl	100 µl
10% APS	80 µl	60 µl	60 µl	60 µl	60 µl	60 µl
TEMED	10 µl	5 µl	5 µl	5 µl	5 µl	5 µl

Coomassie Blue staining

The gels were soaked in the staining solution (0.1% Coomassie Blue R-250, 30% methanol, 10% acetic acid) until uniformly stained blue in colour. The excess staining solution was removed, and the gels were rinsed once with water and destained using destaining solution (30% Ethanol, 10% acetic acid) until the background is clear and bands started to appear.

Silver staining

The gel was fixed for 2 h in a fixative solution followed by washing thrice for 5 min with washing solution. After fixing, the gel was sensitized for 1 min in fresh sensitizer (prepared immediately before use) and rinsed four times for few seconds with water. Further, the gel was incubated for 15 min in freshly prepared cold staining solution in dark and rinsed afterwards four times for a few seconds with water. This was followed by incubation in the fresh developing solution. When bands start to become visible, developing was stopped by adding the fixative solution and incubated for 20 min followed by washing with 1% acetic acid for 30 min. The solutions used for silver staining are described in table 2.18.

Table 2.18 Solutions for silver staining

Solution	Components	Stock concentration	Final concentration
Fixative solution	Methanol	100%	50%
	Acetic acid	100%	12%
Washing solution	Ethanol	100%	50%
Sensitizer	$Na_2S_2O_3$	2%	0.02%
Staining solution	$AgNO_3$	powder	0.1%
Developing solution	Na_2CO_3	10%	2%
	$Na_2S_2O_3$	2%	0.0004%
	Formalin	100%	0.04%
Storage solution	Acetic acid	100%	1%

2.2.8 Western blotting

For western blot analysis, the protein samples were resolved on Bis-Tris gels as described in Section 2.2.7. After separation, the proteins from the gel were transferred onto 0.2 µm

polyvinylidene fluoride (PVDF) membrane for 50 min at 12 V in a semi-dry transfer system (Bio-Rad) or for 90 min at 30 V using wet tank transfer system at 4°C using transfer buffer consisting of 25 mM Tris, 192 mM glycine, 0.01% SDS and 20% methanol. For preliminary visualization, the PVDF membrane was stained with Ponceau S solution (0.5% Ponceau S in 1% acetic acid) for 1 min followed by washing with ddH_2O. The membrane was destained with additional ddH_2O and washed twice with 1x TBST buffer (20 mM Tris pH 7.5, 150 mM NaCl and 0.1% Tween 20) for 10 min followed by washing once with 1x TBS buffer (20 mM Tris pH 7.5, 150 mM NaCl) for 10 min. After washing, the membrane was blocked for 1 h at room temperature (RT) with 0.5% blocking reagent solution (Qiagen) followed by washing twice with 1x TBST buffer and once with TBS buffer for 10 min each. The membrane was incubated with 1:2000 (vol/vol) horseradish peroxidase (HRP)-conjugated anti-Penta His antibody in 1x blocking buffer (Qiagen) for 1 h at RT. After washing the membrane twice with TBST and once with TBS for 10 min, the bound HRP-conjugated antibodies were detected by chemiluminescence by incubating the membrane for 1 min with ECL detection reagents (GE Healthcare) and the signal was quantified and captured using Gel Doc XR+ imaging system (Bio-Rad).

2.2.9 Limited proteolysis

The limited proteolysis experiment was performed by mixing 40 µl of 1 mg/ml protein with 12 µl protease solution and incubated on ice. The proteases: Trypsin, Chymotrypsin, Subtilisin, Elastase and GluC were diluted from a 1 mg/ml stock in 20 mM HEPES pH 7.5, 50 mM NaCl and 10 mM $MgSO_4$ and used at three different concentrations (0.1 mg/ml, 0.01 mg/ml, 0.001 mg/ml). The samples were collected after 30 min, 60 min and overnight (~17 h) and the reaction was stopped by boiling the samples with SDS protein-loading buffer for 10 min. The cleavage products were resolved by SDS-PAGE and stained with Coomassie for visualization. The N- and C- terminal boundaries were determined by Mandy Rettel (Proteomics core facility, EMBL Heidelberg) by performing an in-gel acid hydrolysis. Specifically, the protein bands were cut from the gel and the cysteines were reduced with DTT and alkylated with IAA. The microwave-assisted acid hydrolysis was performed on the cut bands with 3M HCl for 10 min followed by the peptide clean-up. The

peptides were then injected on the LC-MS/MS system (Orbitrap Velos Pro). The data was searched using Mascot search engine against the Uniprot_*E. coli* and Uniprot_Mouse databases.

2.2.10 Tethering of KIX(L664C) and KIX(N627C) with compound 1-10

For affinity measurements by nano-SPR, FP and MST, the purified KIX(L664C) and KIX(N627C) proteins were tethered with the compound 1-10 following the published protocol (Wang et al., 2013a). Specifically, the protein was buffer exchanged into sodium phosphate buffer, pH 6.8 using a 5 ml HiTrap Desalting column (GE Healthcare), tethered with 10 times molar excess of the compound 1-10 and incubated overnight at 4°C. After centrifugation at 14,000 rpm for 10 min, the protein was further buffer exchanged to 25 mM HEPES buffer pH 7.2, 100 mM NaCl and 0.05% Tween20 for FP and MST measurements and 25 mM HEPES pH 7.2, 100 mM NaCl and 5% glycerol for measurements by nano-SPR.

2.2.11 Mass spectrometry for tethering analysis

The samples (1-10 tethered/untethered KIX(L664C) and KIX(N627C)) were diluted 10-fold with 30% acetonitrile (LC-MS grade, Roth) and analyzed by direct infusion Mass Spectrometry on a Synapt G2-S HDMS mass spectrometer (Waters Corporation). The time-of-flight (TOF) analyzer of the mass spectrometer was externally calibrated with a sodium formate mixture from m/z 50 to 1990. Spectra were acquired at 25,000 resolution (FWHM) using a 1 s scan time. Mass spectrometric raw data were analyzed manually using the MassLynx V4.1 Software (Waters Corporation). The MS measurements were performed in collaboration by Prof. Stefan Tenzer and Dr. Ute Distler, Core facility for mass spectrometry, Institute of Immunology, JGU Mainz.

2.2.12 GST Pull-down assay

The His_6-GST-tagged human MLL1-(2840-2858) [denoted as MLL19] was expressed in *E. coli* and purified as described in sections 2.2.4.2 and 2.2.4.3. A concentration of 4 µM His_6-GST-tagged

MLL19 (bait), 20 µM complex or individual BMAL1-(530-625) and KIX proteins (prey) and ~20 µL glutathione agarose (Sigma-Aldrich, München, Germany) were used for pull-down in a reaction volume of 200 µl in the buffer containing 25 mM HEPES, pH 7.2, 150 mM NaCl, 5% glycerol and 2 mM DTT. The reactions were washed three times with the above buffer following the overnight rotation at 4°C. The protein was eluted with SDS protein-loading buffer and boiled for ~5 min followed by SDS-PAGE.

2.2.13 Fluorescent labeling of proteins

For fluorescence polarization and microscale thermophoresis experiments, the purified N-terminally His_6-tagged wild-type BMAL1-(530-625) or mutants P624A and K537Q were labeled with the Red-tris NTA His-tag labeling kit (NanoTemper technologies, München) according to the manufacturer's protocol in a buffer containing 25 mM HEPES, pH 7.2, 100 mM NaCl and 0.05% Tween 20. Specifically, a 100 nM Red-tris NTA dye solution was mixed with 200 nM His_6-tagged BMAL1 protein in 1:1 ratio (vol/vol) (final concentration:100 nM) and incubated at room temperature under dark conditions for 30 min followed by centrifugation at 15,000 g for 10 min.

2.2.14 Microscale Thermophoresis

Microscale thermophoresis (MST) is an optical approach to measure binding-induced changes in the thermophoretic mobility of molecules which is highly sensitive to changes in charge, size of the molecule, hydration shell and alterations in conformation. It is based on the thermophoresis which is the motion of molecules in a temperature gradient induced by an infrared laser coupled into the fluorescence excitation and emission path and this motion is detected and monitored by the fluorescence from the attached fluorophore. MST measurements were performed in the standard treated capillaries on a Monolith NT.115 instrument (NanoTemper technologies, München). The His_6-tagged BMAL1 proteins were labeled as described in section 2.2.13 in a final concentration of 100 nM. The unlabeled and untagged protein (wildtype (WT) KIX domain and mutants) was titrated in the final concentration range of 160 µM-0.0049 µM in a 1:1 ratio

(vol/vol) with the labeled BMAL1 protein (constant, 50 nM final concentration) in buffer containing 25 mM HEPES pH 7.2, 100 mM NaCl and 0.05% Tween 20 in a total reaction volume of 20 µl, incubated at room temperature for 30 min and filled in the standard capillaries for measurements. The measurements were done following the manual instructions at 90% LED (based on the initial fluorescence intensity) and 60% MST power (Infrared laser power) with a 30 s laser-on time and 5 s laser-off time. The red LED-filter combination (excitation 605-645 nm, emission 680-685 nm) was used for fluorescence excitation and emission according to the properties of Red-tris NTA dye. The experiments were repeated 3-4 times. The normalized fluorescence values were plotted on the Y-axis against the untagged protein (titrant) concentration on the X-axis. The data was analyzed using a one-site binding model in GraphPad Prism with or without the Hill function to obtain the K_D values.

2.2.15 Fluorescence Polarization

The fluorescence polarization (FP) principle lies in the fact that the degree of polarization of a fluorophore is inversely proportional to the rotation of the molecule. In fluorescence polarization, one of the binding partners is fluorescently labeled and the fluorophore is excited with the linearly polarized light. The rotation of the labeled molecule due to Brownian motion slows down upon binding with another molecule and decreases the degree of depolarization. In FP experiments, the polarized fluorescence is measured through an emission polarizer either parallel or perpendicular to the plane of polarization of the exciting light and the difference in the intensities of parallel ($I_{\parallel}$) and perpendicular ($I_{\perp}$) emitted light is normalized to the total fluorescence intensity as described in equation-

$$FP = (I_{\parallel} - I_{\perp}) / (I_{\parallel} + I_{\perp})$$

Experimentally, the unlabeled molecules (KIX WT/mutants) were titrated in the final concentration range of 0.04-80 µM with the labeled His_6-tagged BMAL1 protein (labeling

described in section 2.2.13) in a 1:1 ratio (vol/vol) in a total volume of 20 µl, thereby keeping the concentration of labeled BMAL1 protein constant at 50 nM. The reactions were incubated at room temperature for 30 min and transferred to a 384-well flat black low volume plate (Corning, Kaiserslautern, Germany). The measurements were carried out with a Spark 20M plate reader (Tecan, Crailsheim, Germany) in polarization mode at 25°C using excitation and emission wavelengths for the NT-647 dye at 625 nm and 665 nm, respectively. The dissociation constants (K_D) were obtained by fitting the concentration-dependent change in polarization using a non-linear regression function and a one-site specific fit in GraphPad Prism.

2.2.16 Nano-Surface Plasmon Resonance

The nano-Surface Plasmon Resonance (nanoSPR) is a label-free technique where the protein-functionalized gold nanorods were used as the sensing elements which can respond to the binding events near its surface. The detailed procedure for gold nanorod preparation, functionalization with His-tagged proteins and affinity determination is described below.

Gold nanorod preparation, characterization and functionalization for nanoSPR

Cetyl trimethylammonium bromide (CTAB) stabilized gold nanorods were synthesized as described in previous reports (Ahijado-Guzmán et al., 2014). Two batches of nanoparticles were prepared that had bulk resonance wavelengths (λ_{res}) centered at 650 nm (batch 1) and 730 nm (batch 2), respectively. Particles from batch 1 had a diameter of 27.2 ± 3.2 nm and a length of 65.4 ± 4.7 nm, whereas particles from batch 2 had a diameter of 33.2 ± 3.7 nm and a length of 91.4 ± 7.0 nm, as determined by transmission EM. Both particle batches led to similar signal/noise ratios, and their application in nanoSPR experiments resulted in similar K_D values. To enable binding to the His-tagged protein receptors, the CTAB layer around the particles was replaced by NTA, and the His tags of the receptor proteins were complexed with nickel, adapting an established protocol (Ahijado-Guzmán et al., 2017).

Optical dark-field spectroscopy and nanoSPR measurements

For functionalization, the prepared NTA particles were divided into small batches. Each batch was independently functionalized in solution with a different Ni-His_6-tagged protein receptor (i.e. with Ni-His_6-BMAL1-(530-625) WT and mutants (K537Q, P624A)) for interaction with the untagged KIX domain or with Ni-His_6-KIX WT and mutants (untethered/1-10 tethered KIX(L664C), untethered/tethered KIX(N627C), KIX(Y658A), or KIX(Y650A/A654W)) for the interaction with untagged BMAL1-(530-625)P624A, thus making a library of nanoparticle-protein receptor conjugates. These batches of functionalized nanoparticle receptor conjugates were flushed and sequentially immobilized in the microfluidic flow cell and the position of each single nanosensor was recorded after each deposition step as described (Ahijado-Guzmán et al., 2014), thereby, creating a position-encoded sensor substrate. The flow cell was generously washed with buffer (25mM HEPES pH 7.2, 100mM NaCl and 5% glycerol) before and after each particle deposition step to remove the unbound particles and proteins.

For recording the single particle spectra, the optical dark-field spectroscopy setup was used as described in detail (Ye et al., 2018a). Each nanoparticle-receptor sensor has a characteristic plasmon resonance wavelength (λ_{res}), which will have a spectral shift ($\Delta\lambda_{res}$) upon binding of biomolecules near the nanoparticle surface (Ahijado-Guzmán et al., 2014). To obtain satisfactory statistics of the responses over many sensors, an imaging detection method was used, that allowed for the sequential investigation of many particles within the field of view simultaneously as described (Ye et al., 2018a). The immobilized nanoparticle-receptors were illuminated under dark-field geometry and only the scattered light of the nanoparticles entered the spectrometer at a given time to spectrally resolve each nanoparticle spectra.

To carry out a titration experiment, 100 µL of a given concentration of ligand solution (untagged KIX or BMAL1-(530-625)P624A proteins) was flushed into the flow-cell at a flow rate of 50 µl/min, and the spectral shift ($\Delta\lambda_{res}$) of every particle (80-200 particles for each protein receptor) was recorded every 60-90 s at this ligand concentration until an equilibrium value ($\Delta\lambda_{max}$) was reached. This process was repeated for 8-10 different ligand concentrations (0.045-

25 µM). The normalized wavelength shifts or coverage, Θ = $\Delta\lambda/\Delta\lambda_{max}$ was plotted as a function of ligand concentration according to the following equation-

$$\frac{\Delta\lambda}{\Delta\lambda_{max}} = [ligand]/K_D + [ligand]$$

and the dissociation constants (K_D) were obtained using a one-site binding model in GraphPad Prism.

2.2.17 Circular Dichroism (CD) Spectroscopy

Circular Dichroism (CD) is defined as the differential absorption of left (A_L) and right (A_R) circularly polarized light by optically active molecules and can be expressed as-

$$\Delta A = A_L - A_R$$

ΔA is a function of wavelength. The circular dichroism can also be explained in terms of degree of ellipticity, θ, related to optical rotation and polarimetry, and can be interconverted from ΔA as-

$$\Delta A = \theta/32.98$$

CD spectroscopy is an absorption-based technique which can predict the secondary structural components and folding of the proteins. In CD spectroscopy, the left and right circularly polarized light are differently absorbed by chiral components in the protein. The extinction coefficients for left and right circular polarized light are defined as ε_L and ε_R, respectively. The molar circular dichroism can be expressed and converted from ΔA using the following equation-

$$\Delta\varepsilon = (\varepsilon_L - \varepsilon_R) = \Delta A/cl$$

where c is the molar concentration of the sample and l (in cm) is the pathlength of the cuvette used for measurements. The purified proteins were diluted to a final concentration of 10 µM-20

µM in 20 mM sodium phosphate buffer, pH 7.2 and the CD spectra were recorded with a Jasco-815 spectropolarimeter (JASCO Deutschland GmbH, Germany) using a quartz cuvette of 0.1 cm pathlength. The measurements were performed in the continuous scan mode with accumulation of six scans for each measurement at 4°C for BMAL530, KIX WT and mutants and at 20°C for the complexes. The data was collected at every nm from 185 nm to 250 nm at a scan speed of 50 nm/min. For calculated spectra of the complex, the CD spectra from individual BMAL530 and KIX proteins were averaged. For conversion of the machine units (in millidegrees, θ) to mean residue ellipticity (MRE, $[\theta]_R$) from mean residue weight (MRW), pathlength (l, in cm) and protein concentration (c, in mg/ml), the following equation was used-

$$MRE = \theta * (0.1 * MRW)/lc$$

The mean residue weight (MRW) is calculated from molecular weight of the protein (MW, in Da) and number of amino acid residues (N_{res}) as-

$$MRW = MW/N_{res}$$

The data were deconvoluted and the protein secondary structure was calculated using the CONTIN algorithm in the DichroWeb server (Whitmore and Wallace, 2004) with the reference dataset 6 (Sreerama and Woody, 2000).

2.2.18 Static Light Scattering

Static light scattering (SLS) was performed to determine the monodispersity and molecular weight of a protein. For experiments, the sample was passed through a size exclusion chromatography column and the light scattering analysis was performed on the material eluted

from the column which is coupled to a photometer monitoring the light scattering (LS), ultraviolet absorbance (UV) and refractive index (RI). Specifically, the scattering measurements were performed with a DAWN-DSP photometer (Wyatt Tech., Dernbach, Germany) equipped with a HPLC HP 1100 pump (Hewlett Packard, CA, USA; λ = 632.8 nm). As a standard, bovine pancreas ribonuclease was used, and the data analysis was performed using ASTRA software, employing the Rayleigh ratio:

$$R_\theta = [2\pi^2 n_0^2 (dn/dc)^2 / A\lambda^4].M.C$$

where n_0 is the buffer's refractive index, dn/dc is the change in the refractive index from buffer to the presence of protein and set to 0.18 ml/g (typical value for proteins), A is the Avogadro's number, λ is the wavelength of laser, M is the molecular weight and C is the concentration of the protein. The SLS measurements were conducted by Prof. Elmar Jaenicke, Institute for Molecular Biophysics, JGU Mainz.

2.2.19 Crystallization

Initial screening

The initial crystallization experiments were setup in 96 well (2 or 3-subwell) sitting drop plates (TTP Labtech, UK and Jena Biosciences, Germany) using self-made or commercially available screens. Typically, a 100 nl protein solution was mixed with 100 nl reservoir solution using a Mosquito® crystal liquid handler (TTP Labtech, UK) and the plates were kept in RUMED vibration-free incubators (Rubarth Apparate GmbH, Germany) for crystallization screening at two temperatures (20°C and 4°C) and imaged for crystals manually using stereo microscope (Leica microsystems GmbH, Wetzlar, Germany).

Scale-up and optimization

The crystal hits obtained were routinely optimized by varying one or several different parameters such as pH of the buffer, precipitant concentration, salt concentration and protein concentration

for reproducing and obtaining better diffracting crystals. The optimization of the initial hits was performed in 24-well hanging drop Linbro plates with 18 mm or 22 mm circular cover slips (Jena Biosciences, Germany).

Crystallization of 1-10-KIX(L664C), data collection and processing

For crystallization, the purified KIX(L664C) protein was tethered with the compound 1-10 as described in section 2.2.10. Briefly, the protein was buffer exchanged in sodium phosphate buffer pH 6.8 using 5 ml HiTrap Desalting column (GE Healthcare), tethered with 10 times molar excess of the compound 1-10, then further cleaned up and buffer-exchanged using a Superdex S75 10/300 column (GE Healthcare) in the buffer containing 25mM HEPES buffer, pH 6.5 and 100 mM NaCl. The crystals were grown by hanging drop vapor diffusion at 20ºC in 1.8 M ammonium sulphate, 0.1 M Tris-HCl pH 7.0 or 0.1 M HEPES pH 7.5. The obtained crystals were cryoprotected in a solution containing 20% ethylene glycol and flash frozen in liquid nitrogen. The data were collected at the European Synchrotron Radiation Facility (ESRF), Grenoble (ID29 MX beamline) equipped with the Pilatus 6M-F detector. The images were processed using XDS program package and Coot and CCP4 suite were used for model building and refinement.

For co-crystallization of 1-10 tethered KIX(L664C) protein with the BMAL1 peptide, the purified KIX(L664C) protein was freshly tethered with the compound 1-10 as described in section 2.2.10. The BMAL1 peptide (593-SNDEAAMAVIMSLLEADAGLG-613) was dissolved in the KIX buffer (25 mM HEPES pH 6.5, 100 mM NaCl) and incubated in 5-fold molar excess with 1-10-KIX(L664C) for 30 min at room temperature and 1 h on ice and the crystals were grown by hanging drop vapor diffusion at 20ºC in 2.2 M ammonium sulphate and 0.1 M HEPES pH 7.5. The crystals were cryoprotected in a solution containing 20% ethylene glycol and flash frozen in liquid nitrogen. The data were collected at the Swiss Light Source (SLS), PSI, Villigen, Switzerland (X10SA (PXII) beamline) equipped with the Pilatus 6M detector.

2.2.20 Small-angle X-ray scattering (SAXS)

In Small-angle X-ray scattering (SAXS), the protein solution is exposed to X-rays (λ around 0.10-0.15 nm) and the intensity of the X-rays scattered is measured as a function of momentum transfer, s, which is defined as-

$$s = \frac{4\pi}{\lambda} \sin\theta$$

where 2θ is the scattering angle between the incident and the scattered radiation. The SAXS measurements of protein solutions were carried out in batch mode in the concentration range of 0.1-11 mg/ml to check for the interference between protein molecules at different concentrations and to obtain high-quality data. The data were collected on the SAXS beamline P12 (Blanchet et al., 2015) at PETRA III, DESY, Hamburg with an X-ray wavelength of 1.24 Å. For merging the data, the PRIMUS Qt program in the ATSAS 2.8.4 software package (Franke et al., 2017) was used and the radius of gyration (R_g) was determined from small q-regions of the scattering data using the Guinier approximation. The molecular weights and their credibility intervals were determined using a Bayesian inference approach (Hajizadeh et al., 2018) implemented in the ATSAS 2.8.4 software. The pairwise-distribution function [P(r)] was computed using GNOM (Svergun, 1992) which gives the maximum dimension of the macromolecule. The GNOM output file was used by the *ab initio* shape-determination programs-GASBOR (Svergun et al., 2001) and DAMMIF (Franke and Svergun, 2009), which generated 10 independent low-resolution envelopes that were averaged together using DAMAVER (Volkov and Svergun, 2003) and refined using DAMMIN (Svergun, 1999).

To calculate the theoretical scattering profiles from published KIX structures (PDB 4I9O, 2LXS) and for fitting them to the experimental SAXS data, the programs FoXS (Schneidman-Duhovny et al., 2016) and CRYSOL (Svergun et al., 1995) were used. The SREFLEX program (Panjkovich and Svergun, 2016) was used to further improve the agreement of the NMR structure of the KIX domain (from PDB ID: 2LXS, eliminating MLL1 peptide) to the experimental SAXS data calculated for 1-10-KIX by estimating flexibility of the high-resolution structure. To improve the fit of the 1-10-KIX crystal structure to the SAXS envelope, residues G586, V587 and E666-L672, which were

missing in the crystal structure of 1-10-KIX(L664C) (PDB ID: 4I9O), were modeled using MODELLER v9.20 (Webb and Sali, 2014). The program Chimera (Pettersen et al., 2004) was used for the conversion of SAXS envelopes into maps (command: molmap) and for the superposition of maps of the KIX:BMAL530-, KIX:BMAL517- and KIX:BMAL490 complexes onto each other (tool: 'Fit in Map'). The Fit-in-Map tool was also used to fit the SAXS envelopes obtained for KIX and BMAL530 into the SAXS envelope of the BMAL530:KIX complex and to fit the KIX structures into the SAXS map of 1-10-KIX.

3. Results

3.1 Purification of CBP-KIX domain and mutants

3.1.1 Expression and purification of wild-type CBP-KIX domain

The purification of the KIX domain of mouse CBP (586-672) has been described in previous reports where an additional cation-exchange purification step was included (Wang et al., 2013a). In this thesis, as almost pure protein was obtained after Ni^{+2}-affinity chromatography, the requirement of ion-exchange chromatography was excluded. The expression and solubility of KIX domain was tested as His_6- or His_6-GST-fusion protein (Figures 3.1A and 3.1B) in *E. coli* Rosetta DE3 strain (see Materials and methods, section 2.2.4).

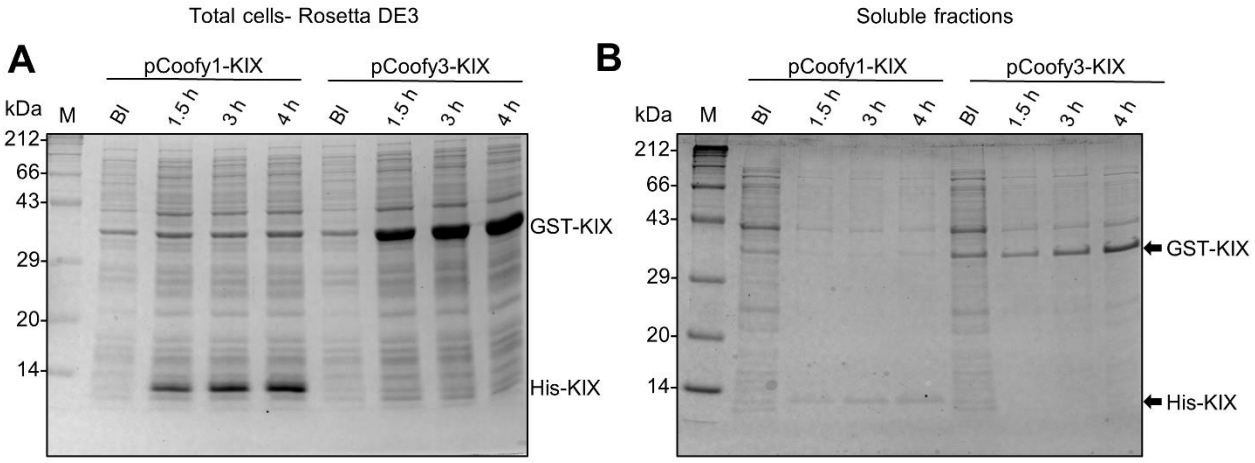

Figure 3.1. The expression and purification of mouse CBP KIX domain. (A, B) Test expression of mouse (m) CBP-KIX as His_6-fusion (~ 12 kDa) and His_6-GST-fusion protein (~ 39 kDa) at 25°C in TB medium analyzed before sonication as total cells (A) and the soluble supernatant fractions after sonication (B). The samples were taken at 1.5 h, 3h, and 4h as marked above the lanes. M=Protein Marker, BI=before induction.

The His_6-tagged KIX domain was further purified using Ni^{+2}-affinity chromatography and size-exclusion chromatography (SEC) as described in section 2.2.4 and the purity of eluted protein

was analyzed on 10% Bis-Tris gels (Fig. 3.2A and 3.2B). For binding affinity measurements and pull-down assays, the His-tag was cleaved using PreScission protease and purified using SEC (Superdex 75 16/60) (Figures 3.2C and 3.2D). The identity and molecular weight of the purified proteins were confirmed by mass spectrometry (Figure 3.3). The mass spectrometry measurements were performed by Dr. Wen Zhang and Dr. Hans Joachim Räder, Max Planck Institute of Polymer Research, Mainz.

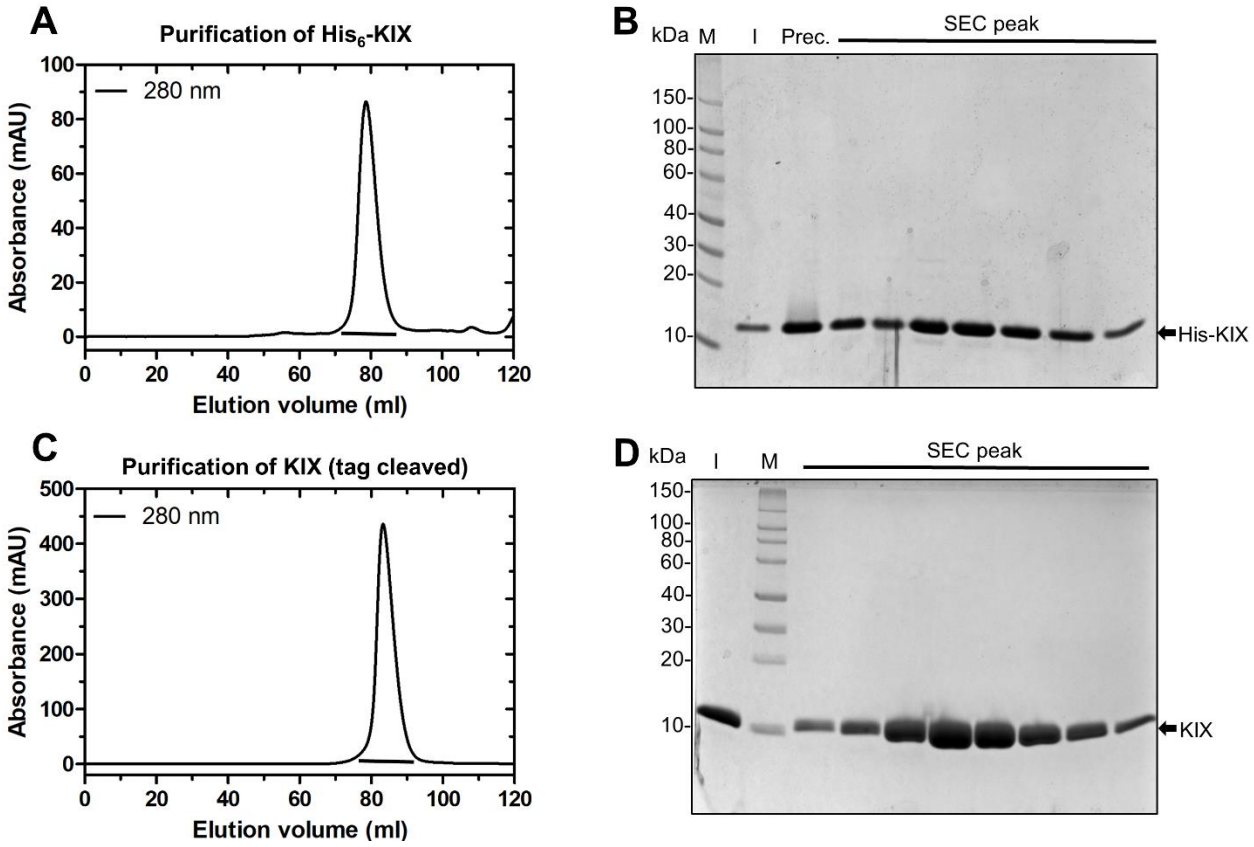

Figure 3.2. The purification of mouse CBP KIX domain. The size-exclusion chromatogram using Superdex 75 16/60 and the respective SDS-PAGE analysis of purified mCBP KIX as His_6-fusion protein (A, B) and after tag-cleavage by PreScission protease (C, D) showing a single peak at 78 ml and 83 ml, respectively visualized by UV absorbance at 280 nm. The line indicates the peak fractions. I=Input sample injected on the size-exclusion column, M=Protein Marker.

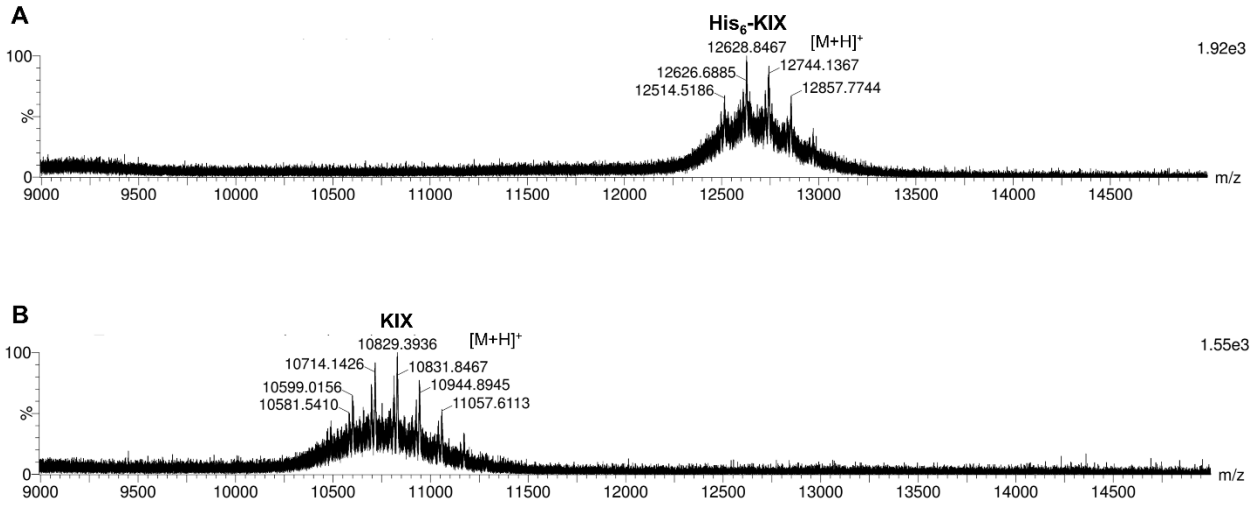

Figure 3.3. MALDI-TOF-MS analysis of (A) His_6-KIX and (B) KIX domain proteins. The mass peaks are plotted as a function of m/z ratio. The molecular mass at 12.6 kDa for His_6-tagged KIX and 10.8 kDa for KIX domain agree with the theoretically calculated values (His_6-KIX, 12.26 kDa; KIX, 10.49 kDa). The matrix used was α-Cyano-4-hydroxycinnamic acid (α-CHCA).

3.1.2 Purification of KIX mutants and tethering with compound 1-10

To determine the binding affinity and binding sites of BMAL530 to and within the KIX domain and to carry out the formation of complex between BMAL530 and KIX mutants, the KIX mutants needed to be purified individually. Two mutants in the MLL-binding pocket- KIX(L664C) and KIX(N627C) - and two mutants in the c-Myb/pKID-binding pocket- KIX(Y658A) and the double mutant KIX(Y650A/A654W) - were generated and purified.

Purification of KIX N627C and KIX L664C

To determine the allosteric binding of different ligands to the MLL- and pKID/c-Myb-binding pockets of KIX, the KIX domain was tethered with the small compound 1-10 to the cysteines mutated in place of N627 and L664 lying at the border of the MLL-binding pocket (Wang et al., 2014). The tethering with 1-10 stabilizes the dynamic conformation of the KIX domain and enabled it to be crystallographically characterized (Wang et al., 2013a). The compound 1-10 sits within the MLL-binding pocket and has been reported to reduce the binding of MLL1 by ~ 100-

fold (Wang et al., 2013a). In this thesis, a similar approach was followed. The mutations N627C and L664C were introduced by modified quick-change mutagenesis as described in section 2.2.2. Both the mutants were expressed as His_6-fusion proteins in Rosetta DE3 *E. coli* strain similar to the wild-type KIX domain and purified (see Materials and methods). The protein was first enriched on the Ni^{+2}-affinity column and the His_6-tag was cleaved during overnight dialysis for microscale thermophoresis (MST) and fluorescence polarization (FP) measurements. For affinity measurements by nano-Surface Plasmon Resonance (nano-SPR), the His_6-tag was retained. During initial purification tests, the His_6-tagged KIX proteins (no cleavage of tag) showed the tendency to precipitate during lysis and dialysis. To minimize the precipitation, the dialysis was avoided, and the protein obtained from Ni^{+2} affinity column was further purified by SEC on the same day (Figure 3.4). The SEC chromatogram showed the elution of the single peak (79 ml for His_6-KIX-N627C and 78 ml for His_6-KIX-L664C) at the volume similar to wild-type His_6-KIX domain (78 ml). For determining the purity, the fractions were analyzed by SDS-PAGE using 10% Bis-Tris gels.

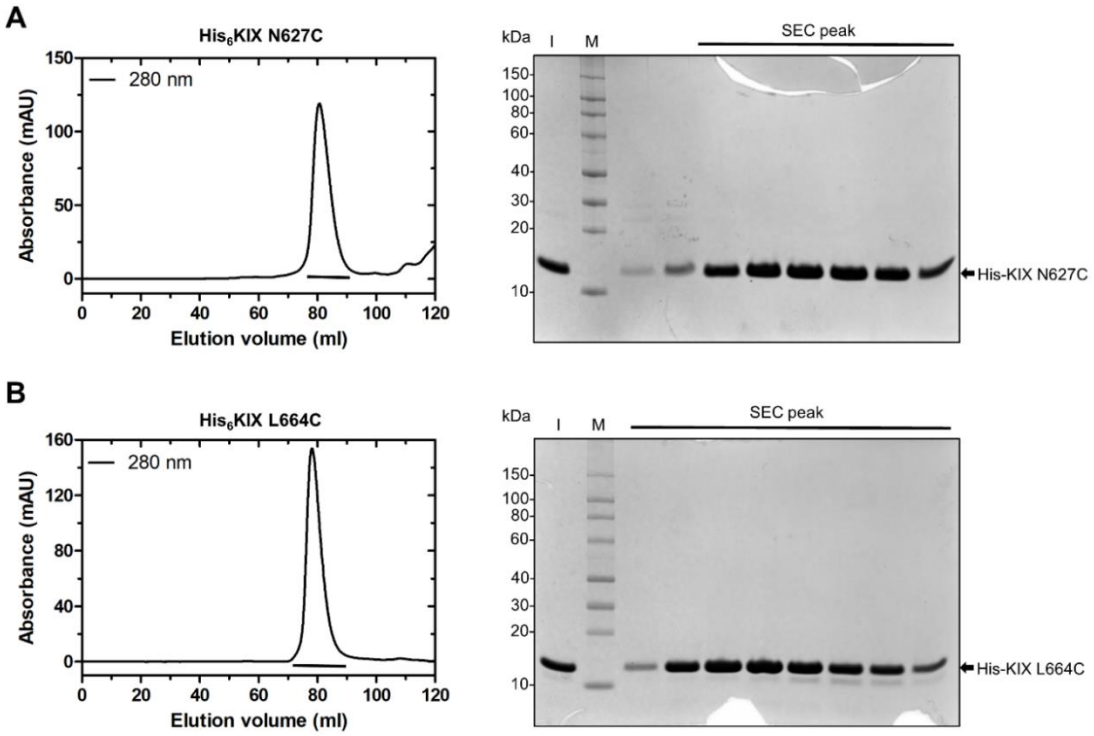

Figure 3.4 Purification of KIX(N627C) and KIX(L664C) mutants. The His_6-tagged KIX(N627C) (A) and KIX(L664C) (B) proteins were purified using Superdex 75 16/60 SEC column. The SEC chromatograms showed the single peak elution at 79 ml and 78 ml for KIX(N627C) and KIX(L664C) proteins, respectively as visualized by UV absorbance at 280 nm.

The fractions marked by black lines were analyzed on 10% Bis-Tris gels. M=protein marker; I=input protein injected on the SEC column.

Tethering of KIX(L664C) and KIX(N627C) with compound 1-10

For the purpose of crystallization and dissecting the BMAL1-KIX interactions, the purified KIX(L664C) and KIX(N627C) proteins were tethered with small compound 1-10 (see Materials and Methods, section 2.2.10). Following the overnight tethering, the protein was either desalted using HiTrap desalting column or gel-filtered using Superdex 75 10/300 column (Figure 3.7A) in the appropriate buffer. The completeness of the tethering, determined by ESI mass spectrometry, was found to be >97% for KIX(L664C) (Figure 3.5) and >99% for KIX(N627C) (Figure 3.8). The comparison of the spectra of untethered and compound 1-10 tethered KIX(L664C) (Figure 3.6) and KIX(N627C) proteins (Figure 3.9) for the +8-charge state indicated the correct mass shift of 367.05 Da induced by the compound 1-10. The 1-10 tethered KIX(L664C) protein was setup for crystallization at 20°C in the previously reported conditions (Wang et al., 2013a) at the concentration of 4.5 mg/ml. The crystals were obtained after overnight incubation (Figure 3.7B) and the diffraction data of 1.6 Å resolution was collected (Figure 3.7C). The data was indexed to the space group $P4_3\,2_1\,2$ with a = 48.22 Å, b = 48.22 Å and c = 85.64 Å. The structure was solved which further confirmed the incorporation of the compound 1-10 (Figure 3.7D-E). The superposition of the solved structure of 1-10-KIX with the published crystal structure (PDB ID: 4I9O) indicated no deviation (Figure 3.7F) other than slightly improved resolution (1.6 Å compared to 2.0 Å of the published structure). ESI mass spectrometry measurements were performed by Prof. Stefan Tenzer and Dr. Ute Distler, Institute of Immunology, JGU Mainz and diffraction data collection and the structure of 1-10-KIX was solved by Dr. Roberto Orru (Wolf group).

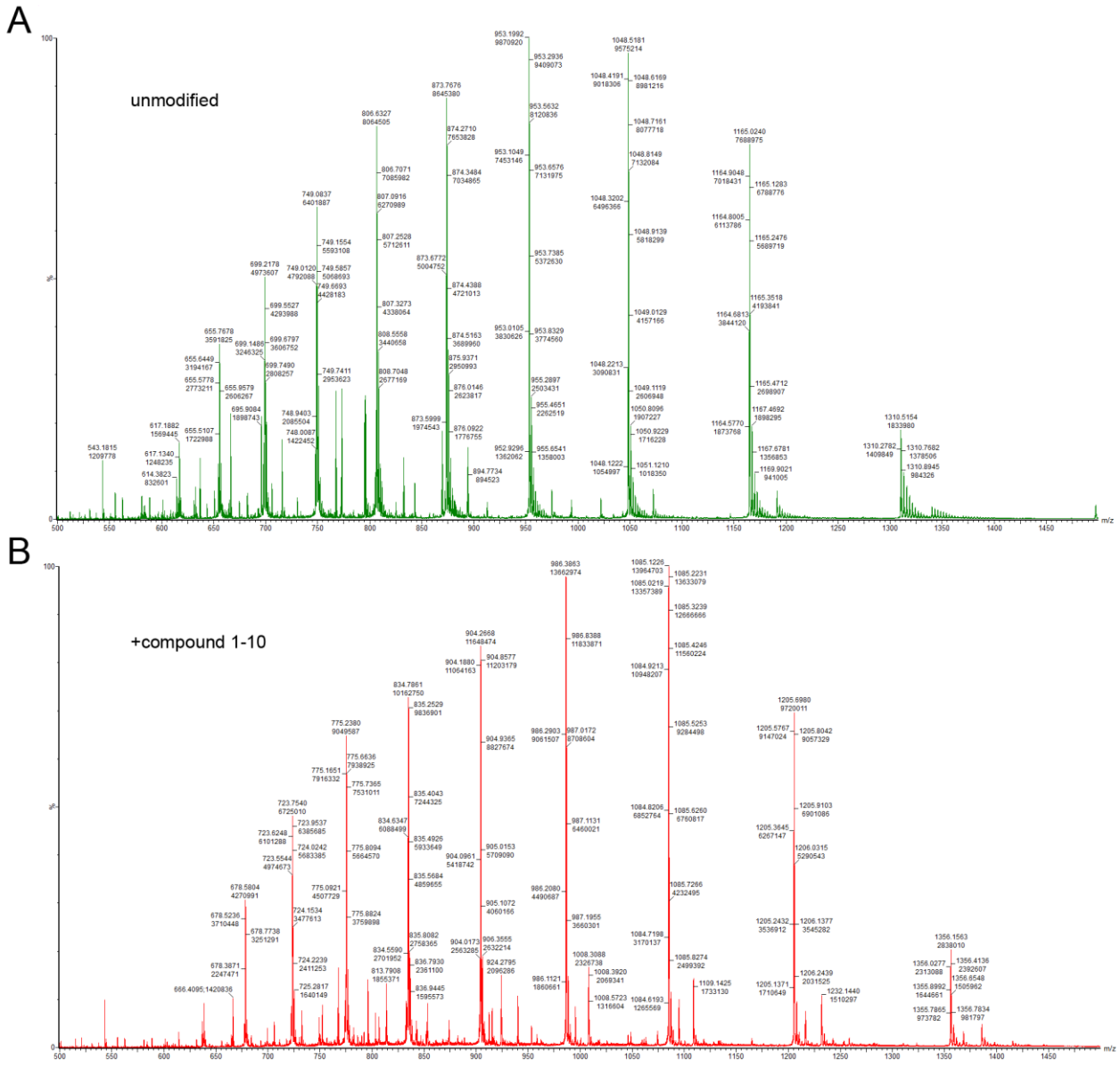

Figure 3.5 Tethering of KIX(L664C) with compound 1-10. ESI mass spectrometry (MS) of untethered (A) and compound 1-10 tethered (B) KIX(L664C) protein. The modification level was >97 % as determined by MS analysis. Adopted from (Garg et al., 2019).

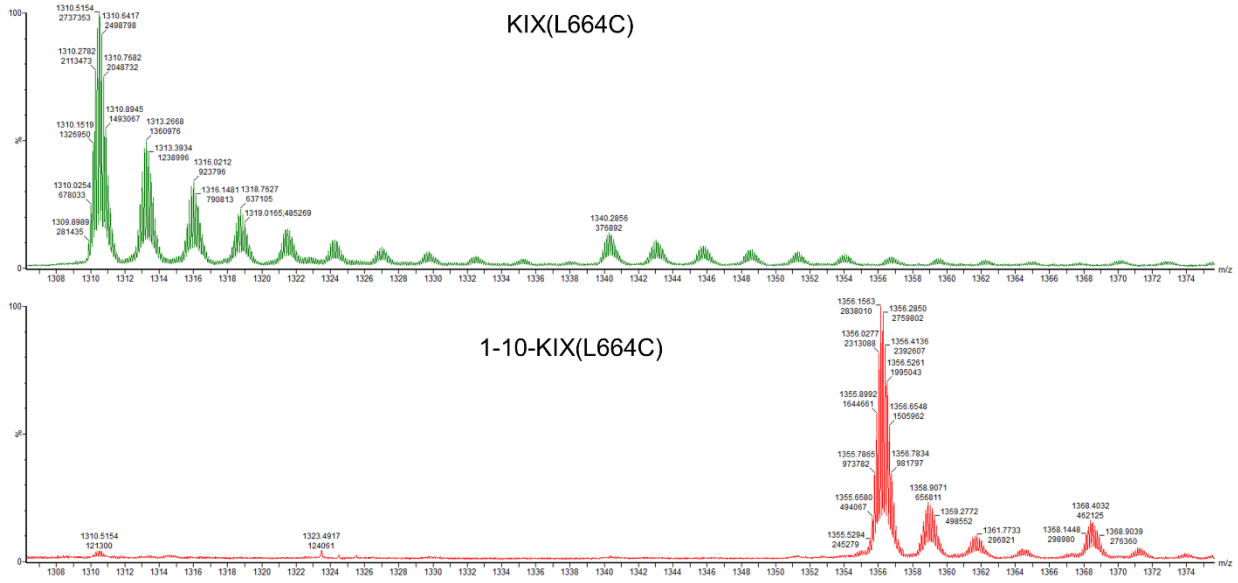

Figure 3.6 Tethering of KIX(L664C) with compound 1-10. The unmodified (upper panel) and modified (lower panel, tethered with compound 1-10) KIX(L664C) proteins for the +8-charge state, indicating the correct mass shift of 367.05Da.

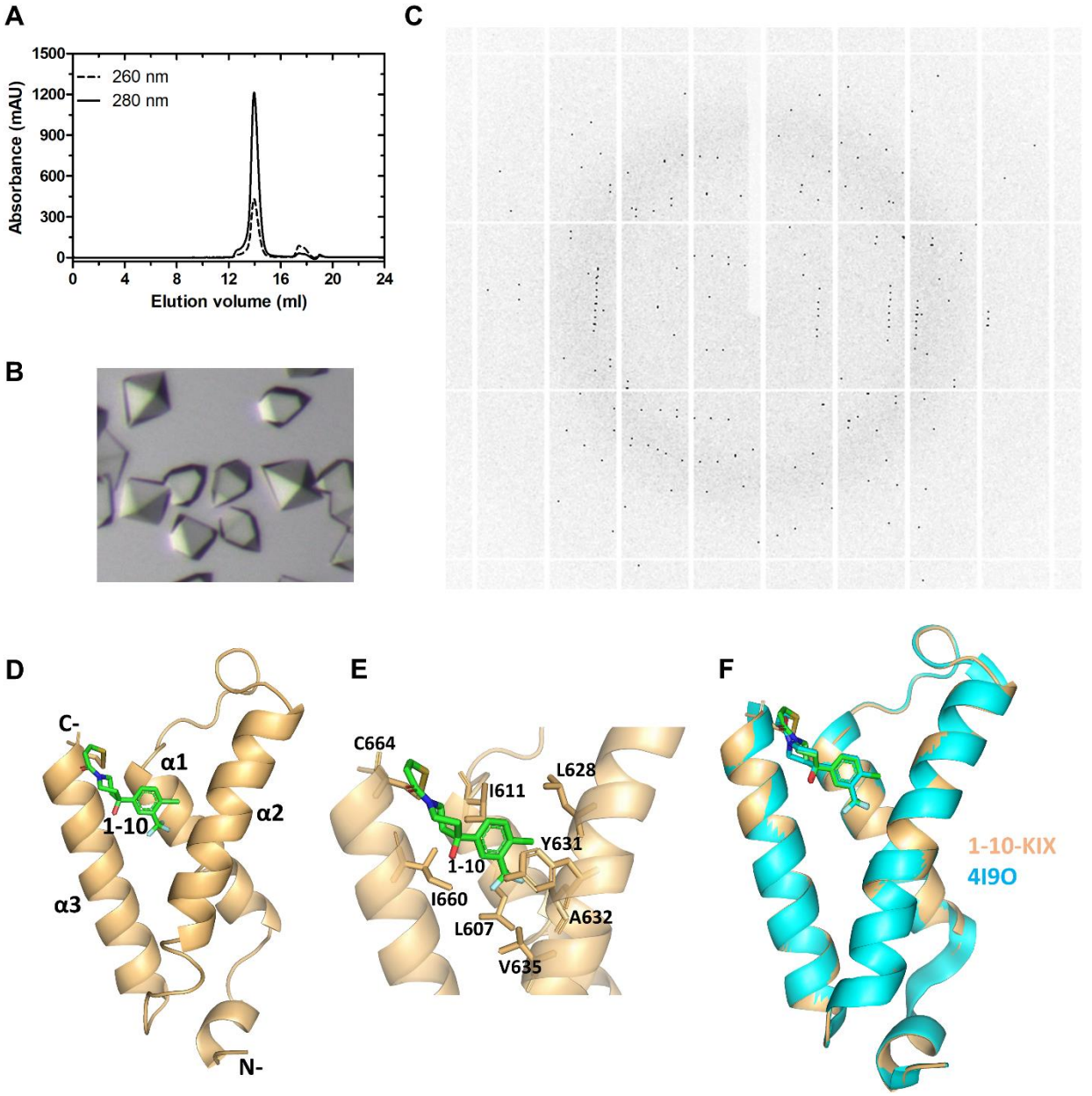

Figure 3.7 1-10 tethering of KIX(L664C), crystallization and X-ray diffraction. (A) The purified KIX(L664C) protein was tethered with compound 1-10 and gel-filtered using size-exclusion column (S75 10/300). (B) The crystals were obtained in 0.1 M HEPES pH 7.5, 2.2 M Ammonium sulfate within one day. (C) The diffraction image obtained from the crystals diffracting to 1.6 Å. (D) The solved structure to 1.6 Å resolution further confirmed the bound 1-10 compound (green) in the MLL-binding pocket. (E) The interactions between compound 1-10 (green) and the side chains of KIX(L664C) (light orange) at the binding surface within 4 Å. (F) The superposition of the solved structure of 1-10-KIX (light orange) with the published structure (PDB: 4I9O) (cyan) revealed no differences.

Table 3.1 X-ray data collection and refinement statistics of 1-10-KIX(L664C) (related to Figure 3.7)

Data Collection	**1-10-KIX(L664C)**
	CBP-KIX (aa 586-672) Compound 1-10 (Wang et al., 2013a)
Beamline	ESRF ID29
Space group	$P4_3\,2_1\,2$
Wavelength (Å)	0.9791
Cell dimensions	
a, b, c (Å)	48.22, 48.22, 85.64
α, β, ϒ (°)	90, 90, 90
Resolution range*	32.02 - 1.603 (1.66 - 1.603)
Unique reflections*	13432 (1300)
Completeness (%)*	96.72 (94.89)
Wilson B-factor (Å^2)	22.38
Refinement	
Resolution range	32.02 - 1.603
Reflections	
Used in the refinement*	13431 (1300)
Used for R-free*	1342 (130)
R_{work} (%)*	19.36 (23.31)
R_{free} (%)*	21.91 (27.45)
Ramachandran values	
Favored region (%)	98.68
Allowed region (%)	100
Outliers (%)	0.00
Average B-factor (Å^2)	30.52
R.m.s.d bonds (Å)	0.008
R.m.s.d angles (°)	1.02

* The values in parenthesis correspond to the highest resolution shell.

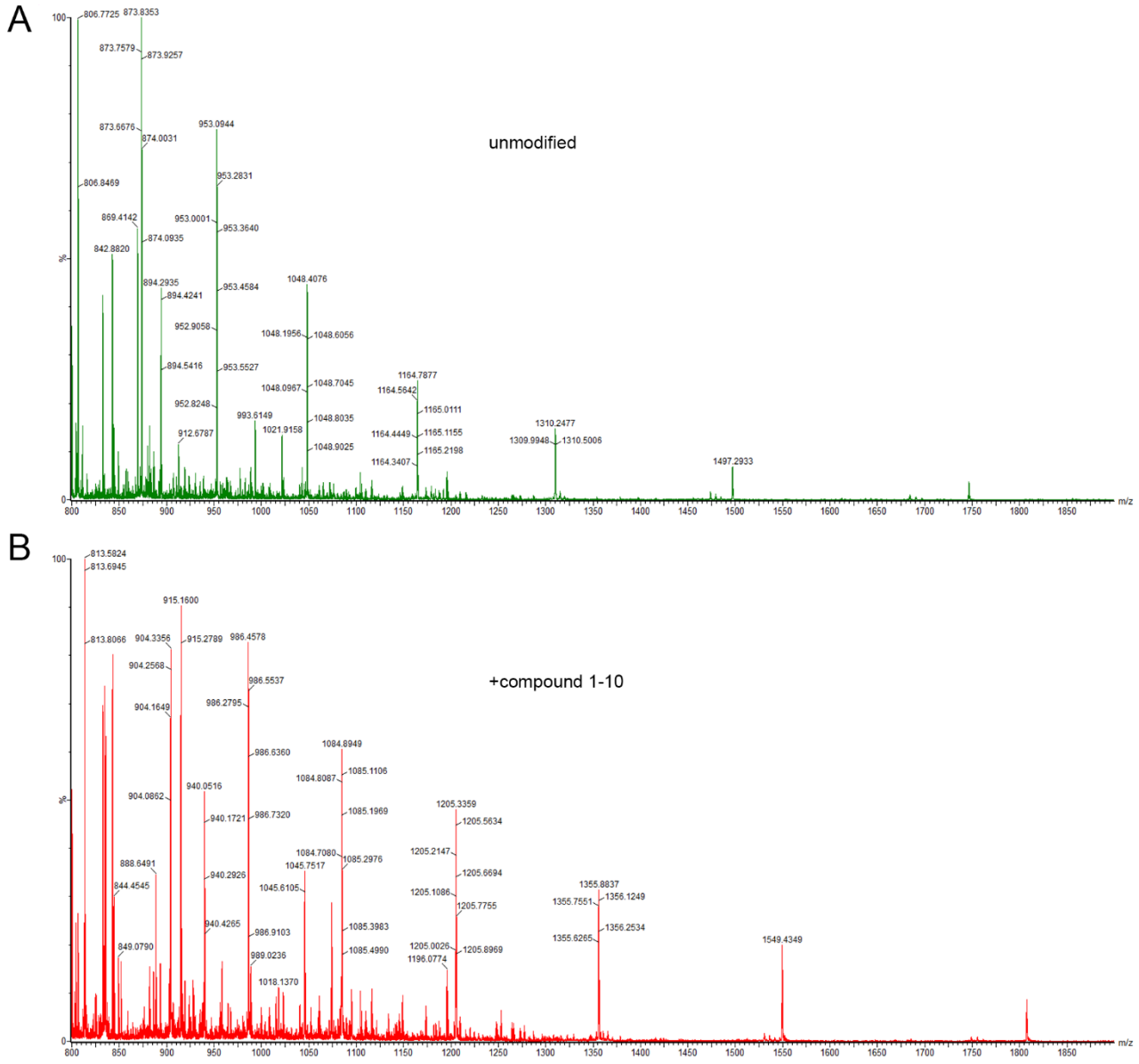

Figure 3.8 Tethering of KIX(N627C) with compound 1-10. ESI-MS spectrum of untethered (A) and compound 1-10 tethered (B) KIX(N627C) protein. The modification level was >99 % as determined by MS analysis. Adopted from (Garg et al., 2019).

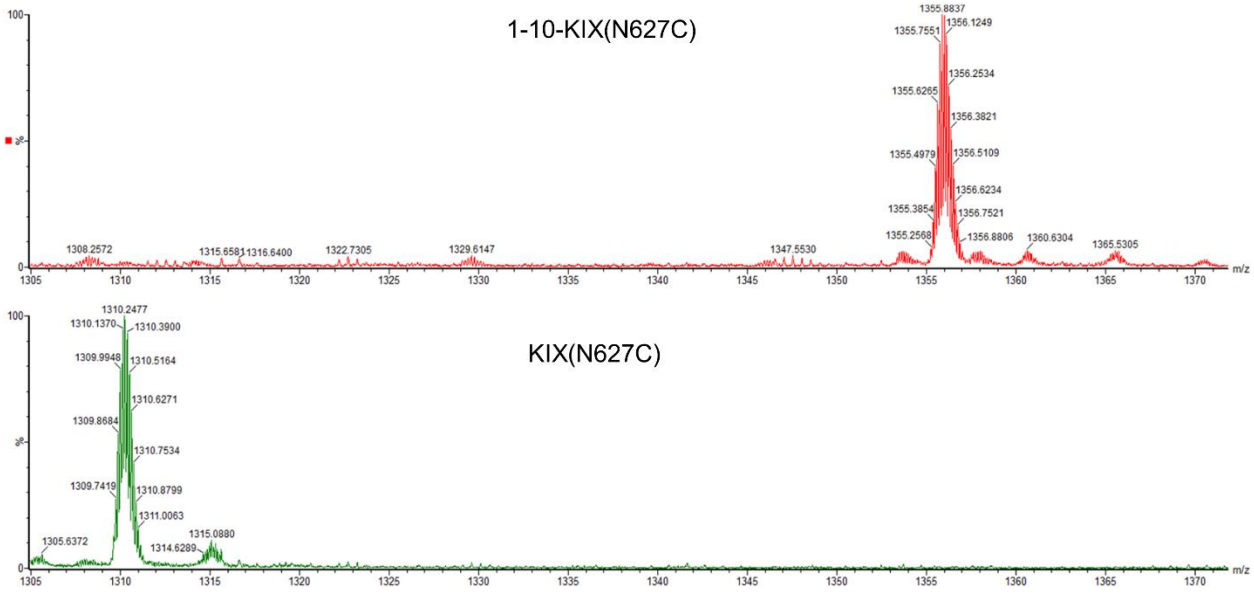

Figure 3.9 Tethering of KIX(N627C) with compound 1-10. The modified (upper panel, tethered with compound 1-10) and unmodified (lower panel) KIX(N627C) proteins for the +8-charge state, indicating the correct mass shift of 367.05Da.

Purification of KIX(Y658A) and KIX(Y650A/A654W)

To further map the binding site of BMAL1 within the KIX domain, mutations were also introduced in the second pKID/c-Myb-binding pocket. The residues Y650, A654 and Y658 were mutated in this study. The mutation of these residues is known to disrupt the binding of c-Myb and CREB-pKID (Parker et al., 1999) and has been physiologically characterized to play a role in hematopoiesis (Kasper et al., 2002). In this thesis, we introduced the Y658A mutation and a double mutation Y650A/A654W. The His_6-fusion proteins were expressed similar to the wild-type KIX domain and purified. Notably, the double mutation Y650A/A654W resulted in a reduced solubility during purification. To tackle the insolubility problem, 0.1% Triton-X was added during the lysis. Both the proteins were purified by Ni^{+2} affinity chromatography followed by SEC using Superdex 75 16/60 column. For MST measurements, the His_6-tag was cleaved using PreScission

protease during overnight dialysis prior to SEC as described in section 2.2.4. The SEC chromatogram for both the mutants showed a single peak elution at the volumes similar to the MLL-binding pocket mutants (L664C and N627C) and wild-type KIX domain which was further analyzed by SDS-PAGE (Figure 3.10). For determining the structural integrity of the purified mutant proteins, CD spectroscopy was performed, which showed that the mutants were well folded and contain structural elements similar to the wild-type KIX domain (Figure 3.11, table 3.2).

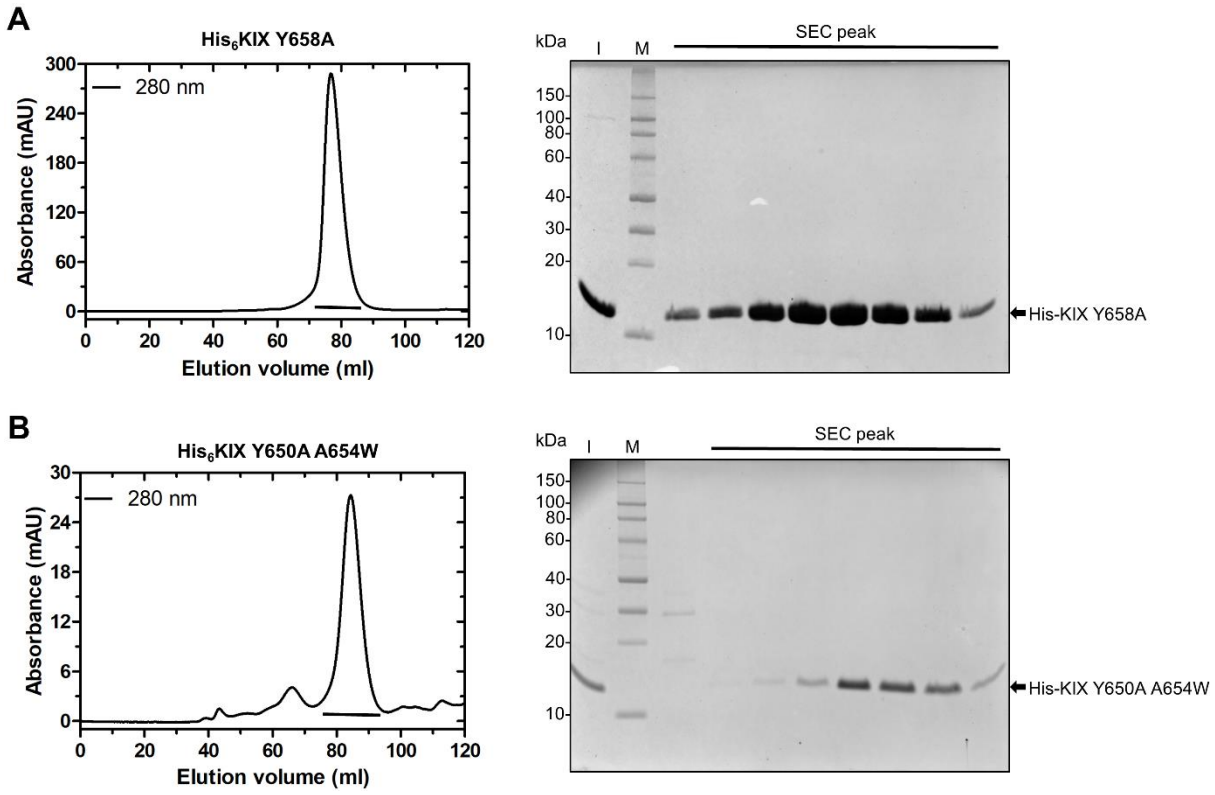

Figure 3.10 Purification of KIX(Y658A) and (Y650A/A654W) mutants. The His_6-fusion proteins were expressed in *E. coli* Rosetta DE3 strain and purified using Ni^{+2} affinity chromatography and SEC. The SEC chromatogram from Superdex 75 16/60 column showed single peak elution for His_6-KIX(Y658A) (A) and the double mutant His_6-KIX(Y650A/A654W) (B). The fractions corresponding to the peak area marked by black lines are analyzed using 10% Bis-Tris gels and used for nano-SPR measurements. M=protein marker; I=input protein injected on the SEC column.

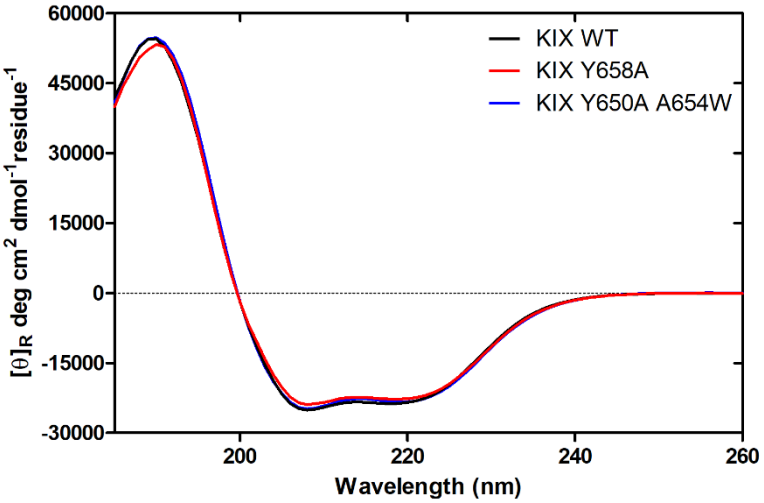

Figure 3.11 The CD spectra of KIX domain proteins with mutations in the c-Myb/pKID-binding pocket. The presence of α-helical structures similar to the WT KIX are indicated by the CD spectra of KIX(Y658A) and KIX(Y650A/A654W) and showed that the mutants retained their secondary structure. The deconvolution (table 3.2) showed that both mutants possess secondary structural contents nearly identical to WT KIX. The molar ellipticity per residue (MRE, $[\theta]_R$) (Y-axis) is plotted against the wavelength (X-axis). Spectra were deconvoluted using the CONTIN algorithm with reference dataset 6 (Sreerama and Woody, 2000) in the DichroWeb server (Whitmore and Wallace, 2004). Adopted from (Garg et al., 2019).

Table 3.2 Deconvolution of CD spectra of KIX WT and mutants KIX(Y658A) and KIX(Y650A/A654W) related to Figure 3.11.

	Helix[a]	Strand[a]	Turns	Unordered	N.r.m.s.d.[b]
KIX WT	0.579	0.062	0.182	0.177	0.016
KIX(Y658A)	0.595	0.074	0.157	0.174	0.070
KIX(Y650A/A654W)	0.568	0.075	0.237	0.120	0.020

[a] Helix and Strand: include regular and distorted helices and strands.

[b] N.r.m.s.d. = Normalized root mean square deviation.

3.1.3 MLL19 expression and purification

The mixed-lineage leukemia (MLL) transactivation domain (TAD) is known to bind to the MLL-binding pocket of the KIX domain (refer to Introduction, section 1.3). It has been reported that the presence of the 19-mer MLL1-TAD peptide (human, aa 2840-2858, termed MLL19) at the MLL-binding site enhances the binding of c-Myb as well as CREB-pKID to the second binding pocket of the KIX domain (Brüschweiler et al., 2013; Goto et al., 2002). Furthermore, MLL19 folds upon complexation with the KIX domain (Brüschweiler et al., 2013). To test the formation of ternary complex between BMAL1-TAD, MLL1-TAD and KIX, either the MLL1-TAD:KIX complex or individual MLL1-TAD needed to be purified. The MLL19 peptide was cloned as His_6-MBP- and His_6-GST-fusion constructs and their expression and solubility was tested in Rosetta DE3 *E. coli* strain in TB medium. The expression tests showed that the MLL19 was better soluble when expressed at 25°C for 5 hours compared to 18°C overnight (Figure 3.12A, left panel). The MLL19 was also co-expressed with KIX domain to aid in the purification of the MLL19:KIX complex. The His_6-GST-fused MLL19 construct (cloned in pCoofy3$_{mod}$-modified for Ampicillin resistance) was chosen for co-expression with KIX (pCoofy1-Kan^R) due to different antibiotic selectivity. Both MLL19 and KIX were found to be soluble when co-expressed at 25°C (Figure 3.12A, right panel).

The purification of MLL19:KIX complex was initially tested either with the cells co-expressing both the proteins or with co-lysis of the cells individually overexpressing His_6-GST-MLL19 and His_6-KIX. Co-expression and co-lysis of His_6-GST-MLL19 and His_6-KIX resulted in aggregation of MLL19 (not shown). To avoid the aggregation of the MLL19 or KIX proteins, the His_6-GST-MLL19 protein was individually purified. The SEC chromatogram resulted in a single peak elution at 59 ml corresponding to ~60 kDa while the theoretical molecular weight of His_6-GST-MLL19 is 30.1 kDa indicating the dimerization of MLL1 during SEC (Figure 3.12B).

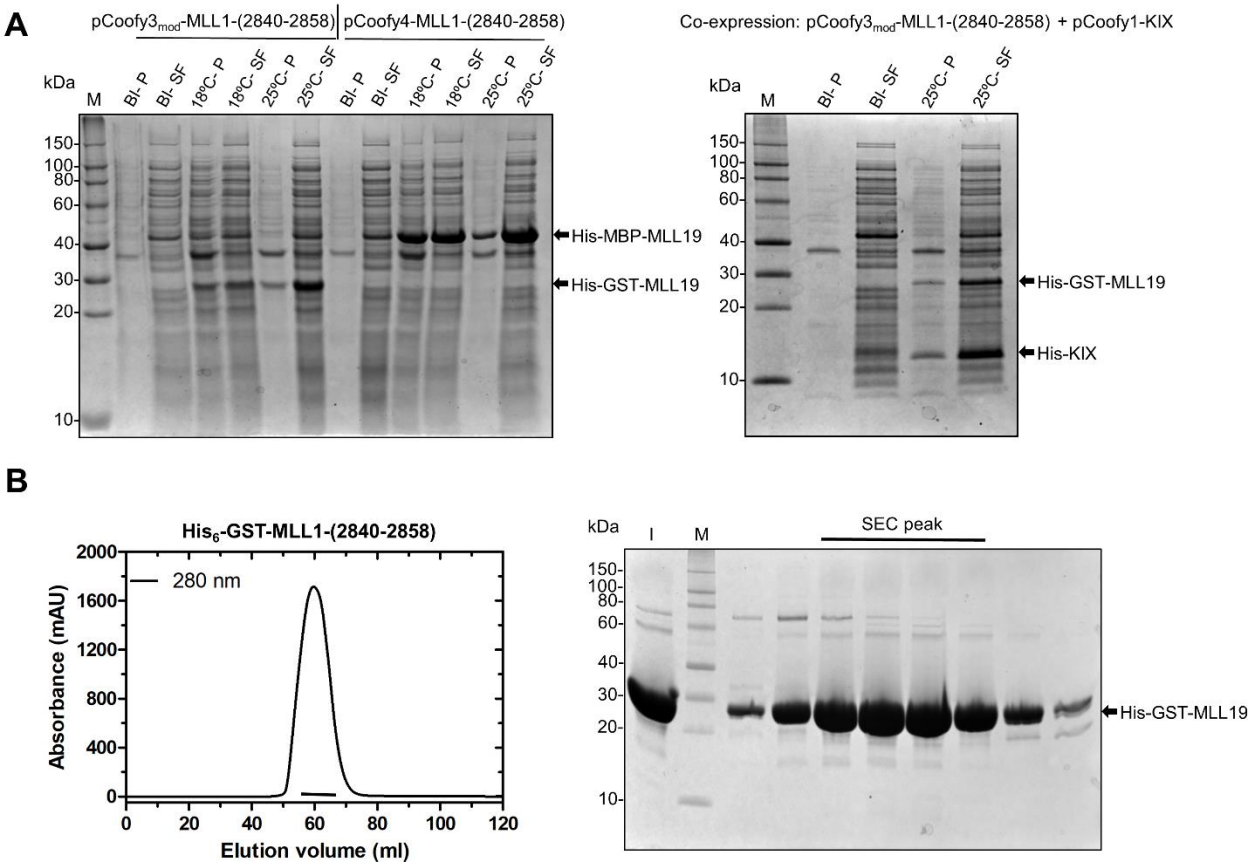

Figure 3.12 Expression and purification of human MLL1-(2840-2858) [termed MLL19]. The expression and solubility of MLL19 was tested as His_6-MBP and His_6-GST-fusion proteins at 18°C and 25°C in TB medium (A, left panel). Both fusion proteins showed better solubility at 25°C. For purification of the MLL19:KIX complex, co-expression of His_6-GST-MLL19 and His_6-KIX was tested at 25°C. Both proteins were well expressed and found to be soluble (A, right panel). Co-expression and co-lysis of His_6-GST-MLL19 and His_6-KIX resulted in aggregation (data not shown). Therefore, His_6-GST-MLL19 was individually purified for interaction studies with purified KIX and BMAL1. (B) Size-exclusion chromatogram of His_6-GST-MLL19 from Superdex 75 16/60 column shows a single peak at 59 ml (~60 kDa) visualized by UV absorbance at 280 nm, indicating the dimer formation. The peak fractions marked by black line were analyzed by SDS-PAGE using 10% Bis-Tris gel (right panel). BI=before induction; SF=soluble fraction; P=pellet after lysis and centrifugation; M=protein marker; I=input protein injected on the SEC column.

3.2 Defining BMAL1:CBP-KIX complexes and crystallization attempts

3.2.1 Purification of BMAL1(490-625):KIX complex

The different constructs of mouse BMAL1 with variable N-terminal length (BMAL1-(577-625) and BMAL1-(490-625)) were first cloned based on the secondary structure prediction by Helena

Breitkreuz and Anna Czarna (Czarna et al., 2011). The BMAL1-(490-625) [termed BMAL490] fragment includes the BMAL1-TAD, Lys537, and parts of the BMAL1 G-region. Prior to establishing of the protocol for purification of the BMAL1:KIX complex in this thesis, the initial purification attempts and tests for complex formation were performed with GST-tagged BMAL490. After the tag cleavage, the pure complex could not be obtained due to the stickiness of GST to BMAL1. To get rid of this problem and improve the purification of the complex for crystallization, the expression and solubility of His_6-fused BMAL490 was tested at 30°C and 18°C in TB medium (Figure 3.13B). The BMAL490:KIX complex was purified (Figures 3.13C and 3.13D) and setup for crystallization trials at 20°C and 4°C, but no complex crystals were obtained.

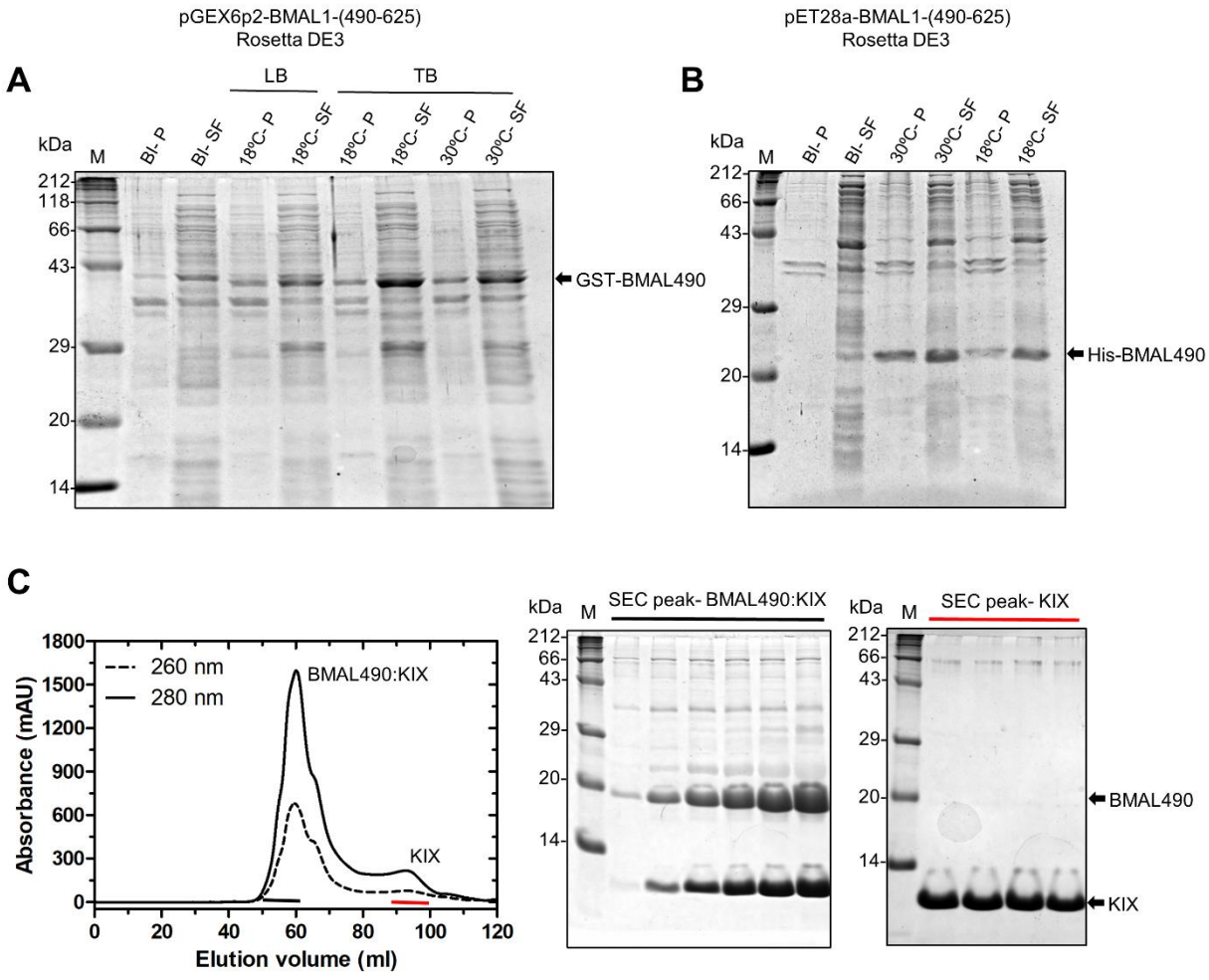

Figure 3.13.: *See next page for figure legend*

Figure 3.13. *(Previous page)* The expression of BMAL1-(490-625) and purification of its complex with KIX domain. The expression and solubility of BMAL490 was tested as GST-fusion (A) and His_6-fusion protein (B) at different temperatures (18°C and 30°C). BI-P=before induction-pellet; BI-SF=before induction-soluble fraction; M=protein marker (C) The size-exclusion chromatogram using Superdex 75 16/60 showing the peaks of complex elution at 60 ml and elution of excess KIX at 94 ml. The eluted fractions analyzed by SDS-PAGE are marked by black (for complex) and red lines (for excess KIX). The black line also indicates the peak fractions used for crystallization trials. The delay in the elution of KIX as compared to Figure 3.2 is due to the artifact of the different size-exclusion column used. M=Protein Marker.

To further define the stable constructs for crystallization, the limited proteolysis was performed with the purified BMAL490:KIX complex using different proteases (Figures 3.14A-3.14C) which yielded two stable fragments of BMAL1 in GluC-proteolysed samples (marked with asterisk, Figure 3.14C). The digestion with 1:1000 Subtilisin dilution, with Elastase, and with 1:100 and 1:1000 dilutions of Chymotrypsin yielded the proteolytic product same as the upper band obtained with GluC-digested samples (marked by plus, Figure 3.14B and 3.14C). At higher concentrations of Trypsin, Subtilisin and Chymotrypsin, BMAL1 was completely degraded. The KIX domain was found to be very stable during the proteolysis experiments. Only at high concentrations of Trypsin and Subtilisin or in the conditions where either BMAL490 was completely or at least C-terminally degraded, the KIX domain was susceptible to degradation. As two distinct stable fragments were obtained in 1:10 GluC dilution at 30 min and 60 min incubation time, they were chosen for further analysis by mass spectrometry. The boundaries of the stable fragments of BMAL1 resulting from Glu-C were determined to be 517-625 and 517-596 (Figure 3.14D) using in-gel acid hydrolysis and mass spectrometry. The C-terminally proteolyzed BMAL1 fragment 517-596 was not followed up as C-terminal residues are important for interaction with the KIX domain (Xu et al., 2015).

Besides the stable BMAL1 construct (517-625) [BMAL517] obtained from proteolysis, another construct with slightly shorter N-terminus (530-625) was designed based on secondary structure prediction and by truncation of Proline-rich region (Figure 1.5 and 3.14E). Both the constructs were tested for expression and solubility in parallel as His_6-GST and His_6-fusion proteins at two different temperatures (18°C and 30°C) in TB medium (Figure 3.15A and 3.15B). The expression

at both temperatures yielded soluble protein with slightly better solubility at 30°C which was further utilized for large-scale expression and purification.

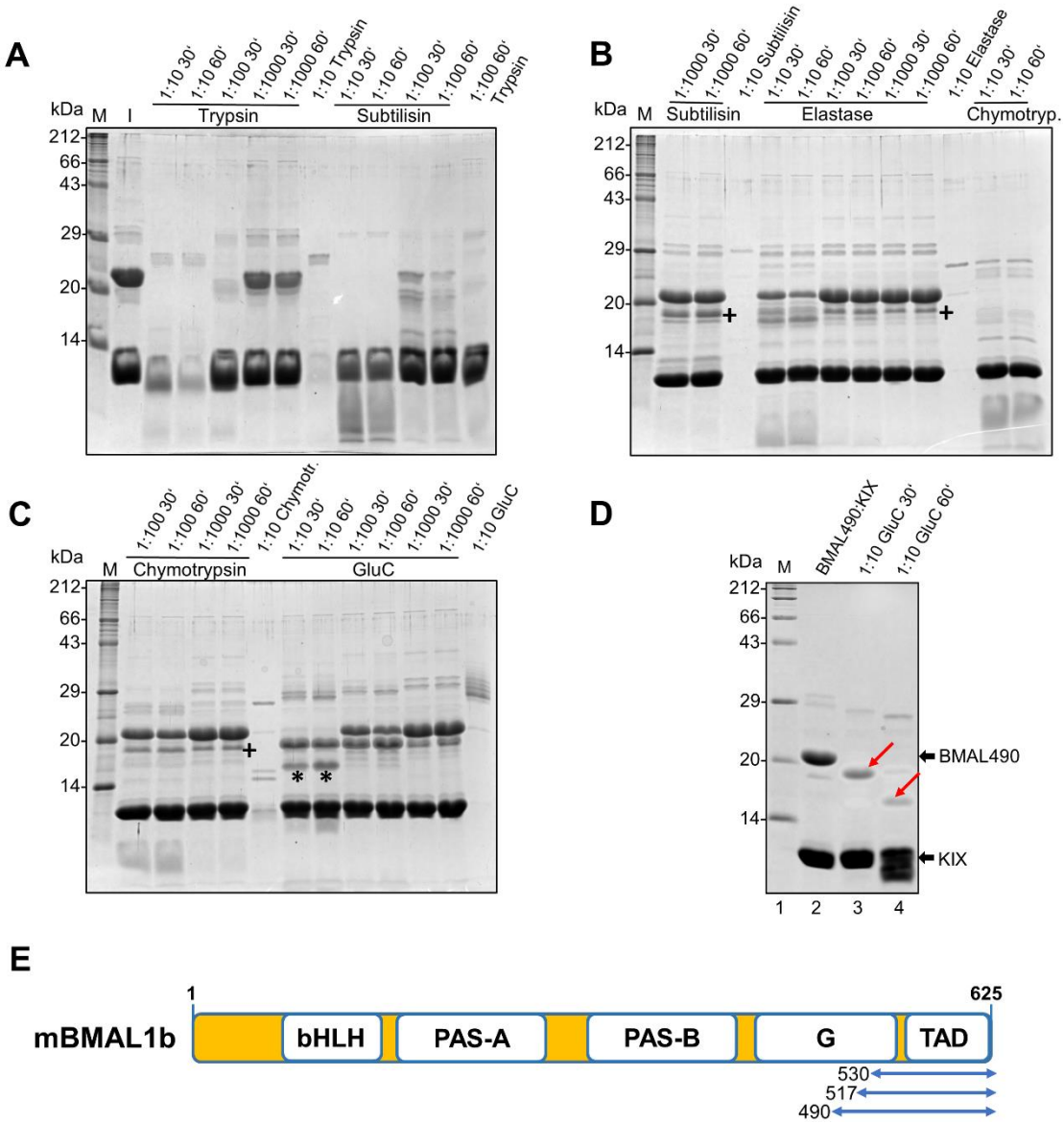

Figure 3.14 (A,B,C) Limited proteolysis of BMAL490:KIX complex. The protein was incubated with different proteases for 30 min and 60 min on ice. The ratio above each lane indicates the dilution of 1 mg/ml protease. The plus marks the proteolytic fragment of same size as the upper band obtained in GluC-digested samples (marked by asterisks). (D) The limited proteolysis experiment was repeated for asterisks marked lanes with 1:10 dilution of GluC at 30 min and 60 min and further processed for mass spectrometry. The arrow in the lane 3 marks the N-terminally degraded BMAL1 (aa 517-625) and the arrow in the lane 4 marks the N-terminally- as well as C-terminally degraded BMAL1 (aa 517-596), which was not followed up. (E) The BMAL1 constructs designed based on the limited proteolysis and secondary structure prediction- (BMAL1-(517-625) and BMAL1-(530-625)) are represented by blue arrows.

3.2.2 Purification of BMAL1

For binding affinity measurements and BMAL1:KIX complex formation, individual BMAL1 proteins were purified. As described in section 3.2.1, based on secondary structure prediction and limited proteolysis with BMAL490:KIX complex, two C-terminal BMAL1 constructs were designed, namely BMAL517 (aa 517-625) and BMAL530 (aa 530-625). Both constructs were cloned as N-terminal His_6-GST- and His_6-fusions and expressed in Rosetta DE3 (Figure 3.15A and 3.15B).

To tackle the problem of conformational dynamicity, the P624A mutation was introduced within the distal C-terminus of BMAL1 which locks it into the *trans* conformation and does not undergo *cis-trans* isomerization (refer to Introduction, section 1.2.3). The BMAL530(P624A) mutant was expressed in Rosetta DE3 *E. coli* strain like wild-type BMAL530. The individual BMAL1 proteins were prone to degradation during the initial Ni^{+2}-affinity purification step with BMAL530(P624A) mutant being more stable than the wild-type BMAL530 during the purification steps. To resolve the degraded products from the main protein, an additional anion-exchange chromatography (AEX) step was performed and the protein was eluted along the NaCl gradient (see Materials and Methods). The final purification step was performed by SEC using a Superdex 75 16/60 column. The SEC chromatogram showed a single peak elution at the volume of 74 ml and 76 ml for wild-type His_6-BMAL530 and His_6-BMAL530(P624A), respectively (Figure 3.15C and 3.15D). The identity and completeness of the protein was confirmed by in-gel GluC digestion followed by mass spectrometry. Additionally, for nano-SPR experiments, the His_6-tag was cleaved following the purification from Ni^{+2}-affinity column during the overnight dialysis which was followed by AEX and SEC. The BMAL530 and KIX domain have similar molecular weight (11.5 kDa and 12 kDa for His_6-fusion proteins, respectively and 9.7 kDa and 10.4 kDa after cleaving of the tag) but the elution volumes of BMAL530 proteins were found to differ from the elution of wild-type KIX (at ~94 ml) using the same column. This difference was attributed to the elongated shape of BMAL530 determined from small-angle X-ray scattering (SAXS) analysis (section 3.3). The static light scattering (SLS) analysis (section 3.3) and expected molecular weights calculated from SAXS confirmed the BMAL530 protein to be monomeric. The secondary structure of wild-type KIX and BMAL530 proteins was characterized using CD spectroscopy which showed BMAL530 as intrinsically disordered and unstructured in agreement with previous reports (Czarna et al.,

2011). KIX was determined to be mostly helical (Figure 3.16, table 3.3) consistent with the known NMR and crystal structures (Radhakrishnan et al., 1997; Wang et al., 2013a; Zor et al., 2004).

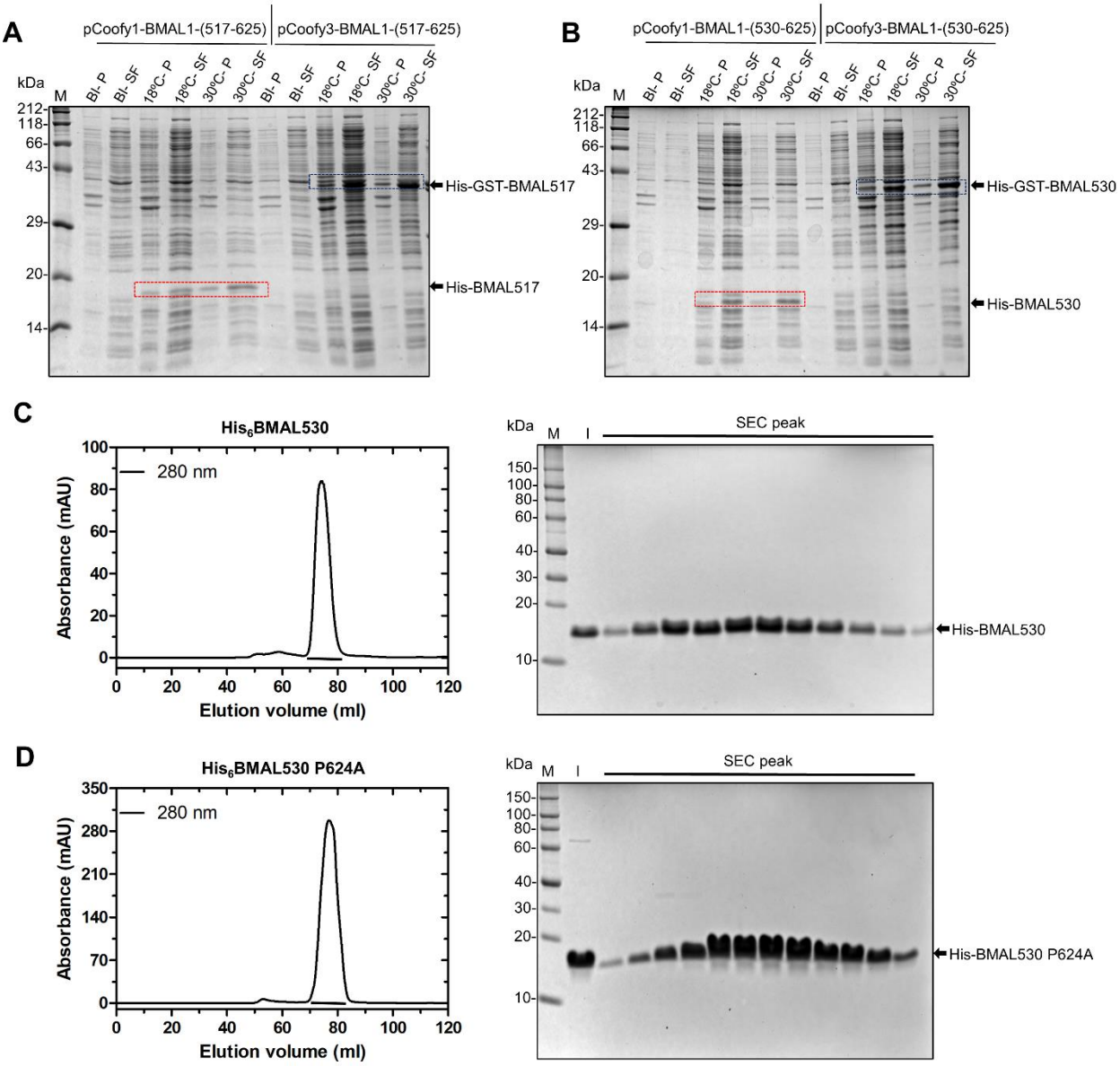

Figure 3.15 Expression and purification of BMAL530 proteins. The expression and solubility of BMAL517 (A) and BMAL530 (B) were tested as His_6- and His_6-GST fusion proteins at 18°C and 30°C in TB medium. The expressed His_6-fusion proteins are marked with red boxes. The SEC chromatograms of wild-type His_6-BMAL530 (C) and His_6-BMAL530(P624A) (D) from Superdex 75 16/60 column showed a single peak elution at 74 ml and 76 ml, respectively which differs from the elution volume of KIX domain (at 94 ml) using the same column. This difference is due to the elongated shape of BMAL1 which is also evident from aberrant running behavior in SDS-PAGE and further confirmed from SAXS analysis (described in section 3.3). The peak fractions marked by black line were analyzed using 10% Bis-

Tris gels. M=protein marker; I=input protein injected on the SEC column; BI-P=before induction-pellet; BI-SF=before induction-soluble fraction.

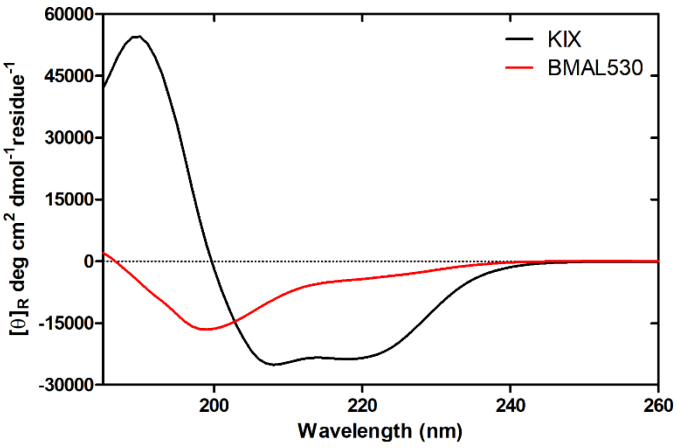

Figure 3.16 CD spectroscopy measurements of BMAL530 and KIX proteins. The CD spectra of wild-type BMAL530 and KIX proteins showed a mostly disordered conformation for BMAL1 and a well-folded α-helical structure for the KIX domain consistent with the previous reports (Radhakrishnan et al., 1997; Wang et al., 2013a; Zor et al., 2004). Adopted from (Garg et al., 2019).

Table 3.3 Deconvolution of CD spectra of wild-type BMAL530 and KIX proteins

	Helix[a]	Strand[a]	Turns	Unordered	N.r.m.s.d.[b]
BMAL530	0.083	0.104	0.111	0.702	0.032
KIX	0.579	0.062	0.182	0.177	0.016

[a] Helix and Strand: include regular and distorted helices and strands.
[b] N.r.m.s.d. = Normalized root mean square deviation.

3.2.3 BMAL517:KIX complex

Of the two BMAL1 constructs [(517-625) and (530-625)] tested for expression and solubility, the BMAL1-(517-625) [termed BMAL517] was tested for complexation with KIX domain and crystallization. The BMAL517:KIX was purified using His_6-fused BMAL517 and KIX constructs using Ni^{+2}-affinity chromatography and SEC (see Materials and methods, section 2.2.4). Due to incomplete cleavage of the His-tag, the SEC chromatogram resulted in two partially overlapping

peaks (Figure 3.17A) which were analyzed by SDS-PAGE and only the fractions containing pure cleaved BMAL517:KIX complex were subjected to analytical Superdex 75 10/300 column (Figure 3.17B). During this step, the complex eluted at 10 ml corresponding to 40 kDa but the theoretical molecular weight of the complex is 21.3 kDa indicating the dimer formation. But due to the elongated shape of BMAL1 C-terminal fragments, as evident from former study (Czarna et al., 2011) and from the aberrant running behavior of BMAL517 (theoretical MW, 10.97 kDa), the possibility of advanced elution volume of the complex due to the extended shape of BMAL1 could not be excluded and hence, was further confirmed by SAXS analysis (section 3.3.7). Nevertheless, the pure BMAL517:KIX obtained after analytical SEC was setup for crystallization trials which did not result in any complex crystals. The difficulty in obtaining crystals of the BMAL1(517):KIX complex might be due to the conformational dynamicity of KIX and BMAL1 proteins as well as the proline-rich region present at the distal N-terminus of the BMAL517 construct used.

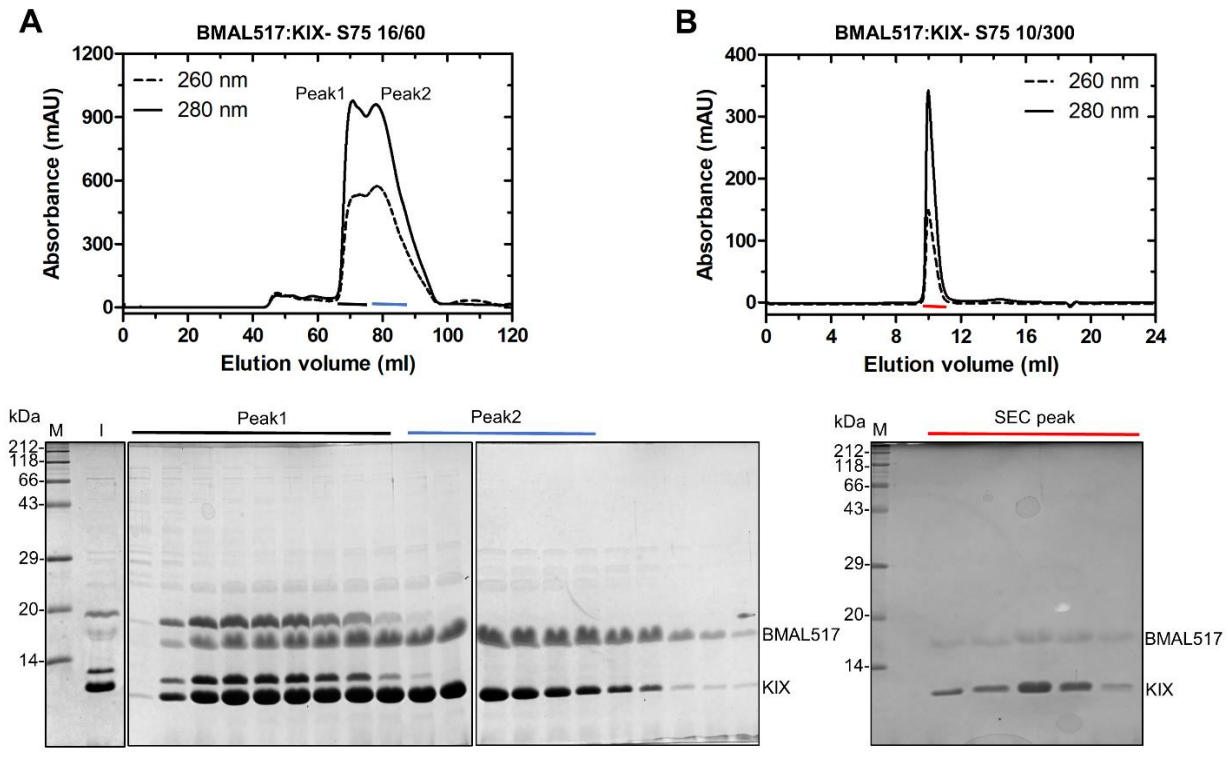

Figure 3.17 The purification of BMAL517:KIX complex. (A) The size exclusion chromatogram of BMAL517:KIX complex purification using Superdex 75 16/60 column showing two overlapping peaks-one containing impurities from uncleaved BMAL517 and KIX proteins marked by black line and other peak showed to elute pure BMAL517:KIX complex marked by blue line. The fractions marked by blue line were used for further SEC using Superdex 75 10/300

column (B), analyzed by SDS-PAGE and used for crystallization trials. The fractions corresponding to peak from S75 10/300 column are marked by red line. M=protein marker; I=input protein injected on the column.

3.2.4 BMAL530:KIX complex

As the purified BMAL517:KIX complex did not result in crystal formation, the BMAL1-(530-625) [termed BMAL530] construct, designed by truncation of a proline-rich N-terminal region from the BMAL517 construct, was tested for complex formation with the KIX domain and for crystallization. Due to stickiness of GST described in section 3.2.1, the BMAL530:KIX complex was purified using His_6-fusion proteins as described in section 2.2.4. The final purification step by size-exclusion chromatography using Superdex 75 16/60 column yielded two distinct peaks of the complex and excess KIX (Figure 3.18A) at 73 ml and 94 ml, respectively. The delay in the elution of the KIX protein as compared to the SEC peaks shown in Figure 3.2 is due to the artifact of the different size-exclusion column used for purification as also described in Figure 3.13 and does not correspond to the different oligomerization state of the proteins as confirmed by calibration of the columns. The fractions were analyzed by SDS-PAGE and the ones corresponding to the BMAL530:KIX complex were set-up for crystallization trials at the concentration of 13 mg/ml and 25 mg/ml. No crystal hits were obtained from both concentrations.

Further, to solve the problem of conformational dynamicity, the BMAL530(P624A) mutant (refer to sections 1.2.3 and 3.2.2) was tested for complex formation with the KIX domain and subsequent crystallization. The BMAL530(P624A):KIX complex was purified as described for the wild-type protein complex using His_6-fused constructs. As described for the wild-type BMAL530:KIX complex, the SEC chromatogram from the Superdex 75 16/60 column resulted in two peaks at 73 ml and 94 ml corresponding to the complex and excess KIX, respectively (data not shown). The purified protein complex was setup for crystallization trials which did not result in any crystallization hits.

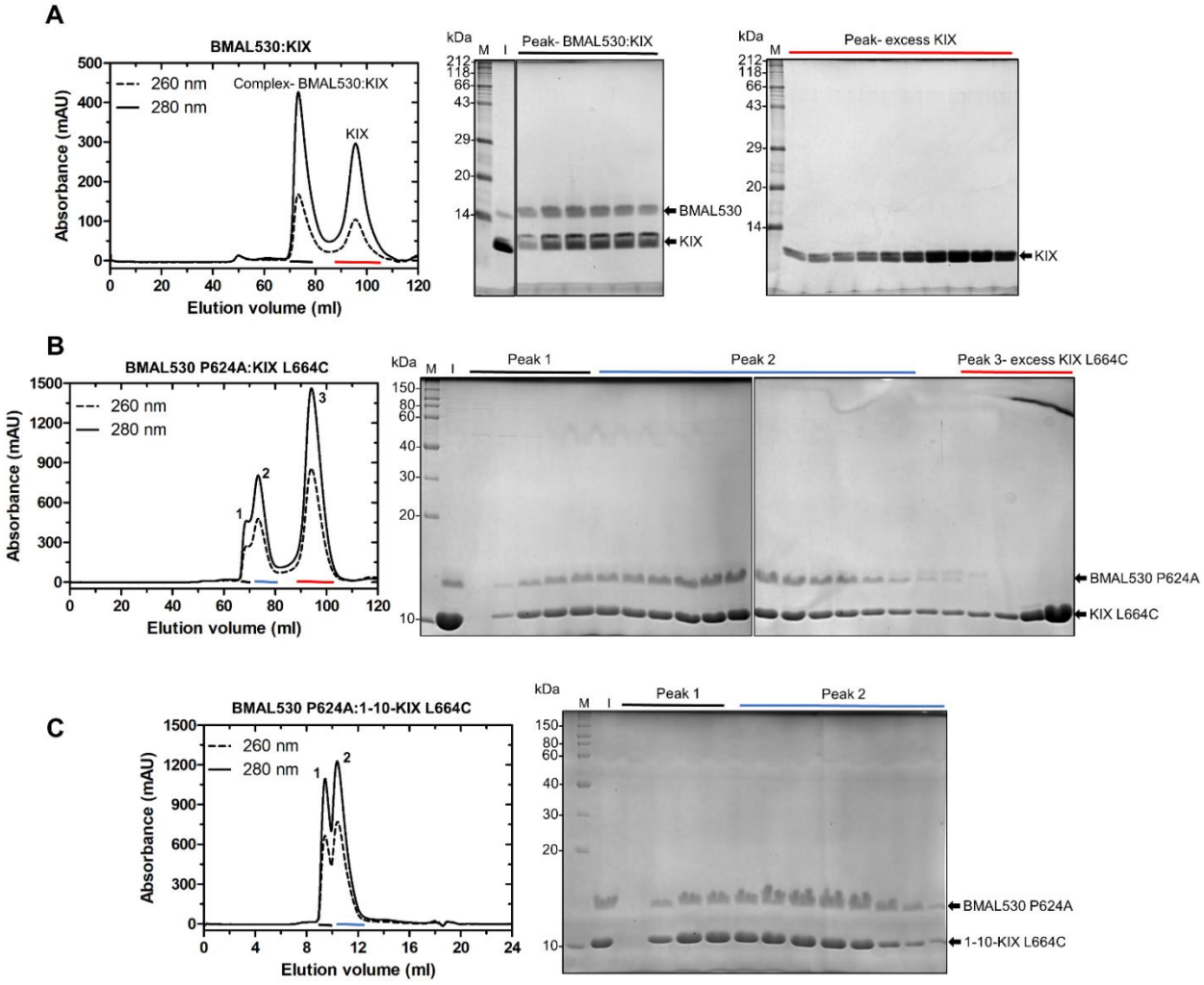

Figure 3.18 The purification of BMAL1-(530-625):KIX complexes and tethering with compound 1-10. (A) The SEC chromatogram showing two peaks of BMAL530:KIX complex and excess KIX eluting at 73 ml and 94 ml, respectively visualized by absorbance at 260 nm and 280 nm. The peak fractions were analyzed on 16% SDS-PAGE gels (Tris-Glycine running buffer). (B) To stabilize BMAL1 and KIX domain, the P624A mutation was introduced within distal C-terminus of BMAL530 and the L664C mutation was introduced within KIX domain for tethering with compound 1-10. The protein complex was purified using Superdex 75 16/60 yielding two overlapping peaks of protein complex (marked with black and blue lines; left panel) and a peak of excess KIX-(L664C) (marked by red line) which were analyzed by 10% Bis-Tris SDS-PAGE gels (MES running buffer; right panel). (C) The fractions corresponding to the two complex peaks were tethered together with the small compound 1-10 and subjected to analytical SEC using Superdex 75 10/300 column, which again yielded two peaks (marked with black and blue lines). Both peaks were analyzed by 10% Bis-Tris gels and setup for crystallization separately. M=protein marker; I=input protein injected on the column.

Next, to further stabilize the KIX domain, the L664C mutation was introduced. As reported (Wang et al., 2013a) and we have also shown in this thesis (section 3.1.2, Figure 3.7), the KIX domain can only be crystallized upon tethering of the small compound 1-10 to cysteine mutated in place of L664 in order to stabilize the protein. The similar approach was tried but the initial tethering and crystallization trials were performed with the preformed BMAL530(P624A):KIX(L664C) complex. The protein complex was purified using the similar procedure as described for the wild-type BMAL530:KIX complex. Surprisingly, the SEC chromatogram showed two overlapping peaks for the BMAL530(P624A):KIX(L664C) complex (one being eluted at 73 ml as for the wild-type BMAL530:KIX complex (peak 2), and a second peak (peak 1) eluting earlier at about 68 ml) as well as a third peak (peak 3) for excess KIX, as analyzed by SDS-PAGE (Figure 3.18B). The fractions corresponding to the two protein complex peaks could not be distinguished by SDS-PAGE and may therefore result from different conformations in the two complex populations leading to different shapes and elution volumes. The two peaks were processed together for tethering with the small compound 1-10 and subsequently subjected to analytical SEC using a Superdex 75 10/300 column. The analytical size-exclusion chromatogram again yielded two peaks which look similar on the gel (Figure 3.18C). The fractions were pooled separately for each peak. As the completeness of compound 1-10 tethering within the preformed BMAL1:KIX complex was not determined experimentally, the two peaks could in principle result from partial labelling of the preformed complex. Additionally, the two peaks could be the result of two different protein conformations as suggested for the untethered BMAL530(P624A):KIX(L664C) complex. Crystallization trials were performed with both peaks separately, but no complex crystals were obtained.

To further obtain the complex of BMAL1 with completely tethered KIX, the tethering with the compound 1-10 was performed with pre-purified KIX(L664C) (refer to section 3.1.2) and the individual BMAL530(P624A) was also purified (section 3.2.2, Figure 3.15). The SEC chromatogram yielded a single peak of the complex (Figure 3.19) eluting at the volume of ~ 11 ml similar to the elution of second peak in Figure 3.18C and to the wild-type BMAL530:KIX complex. This indicated that the elution of an additional peak at an earlier volume during the co-purification of BMAL530(P624A):KIX(L664C) complex might be due to the different oligomerization or

conformational state of the complex but after complete tethering of compound 1-10 to KIX, it favored the elution profile similar to the wild-type BMAL530:KIX complex. The KIX(L664C)-1-10:BMAL530(P624A) complex formed from individual proteins was setup for crystallization, but no complex crystals were obtained.

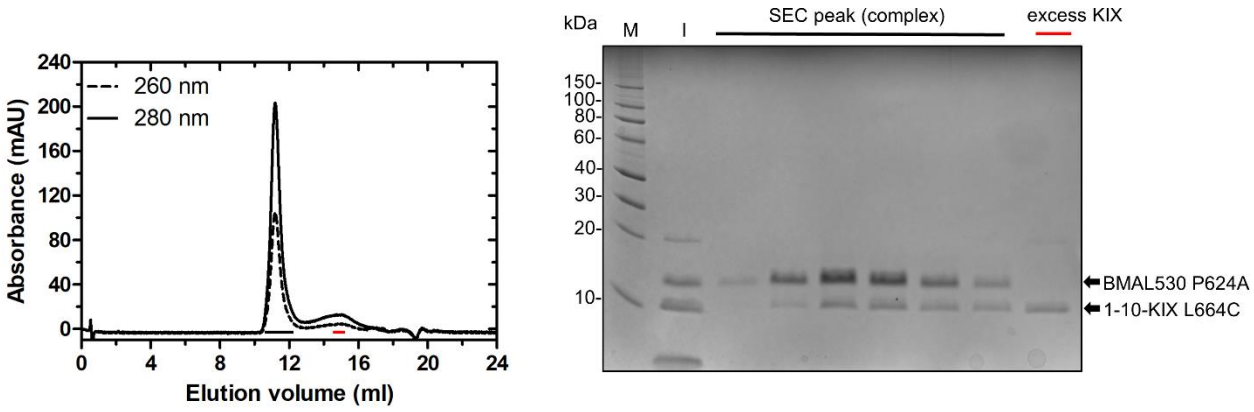

Figure 3.19 Reconstitution of 1-10-KIX(L664C):BMAL530(P624A) complex and crystallization. The SEC analysis of the 1-10-KIX(L664C):BMAL530(P624A) complex reconstituted from the individually purified proteins showing elution of a single peak of the complex at ~ 11 ml and excess KIX at ~ 15 ml observed by UV absorbance at 260 and 280 nm. The peak fractions marked by black and red lines were analyzed by SDS-PAGE (right panel) and fractions corresponding to the complex were setup for crystallization. M=protein marker; I=input protein injected on SEC column.

To further obtain the crystals of the BMAL1:KIX complex, the purified 1-10-tethered-KIX(L664C) protein was setup for co-crystallization with the synthesized 21-mer peptide of BMAL1 (593-SNDEAAMAVIMSLLEADAGLG-613). Initially, the crystallization plate was setup with the published condition of KIX-1-10 (1.8M-2.2 M ammonium sulfate, 0.1 M Tris pH 7.5/HEPES pH 7.0 (Wang et al., 2013a)). Crystals were obtained within one day in a 1:1 and 1:2 protein:peptide ratio (Figure 3.20A). In these crystals, the presence of 1-10 KIX, but not of the peptide, was confirmed by silver staining (data not shown).

Few more crystal hits from all three tested protein:peptide ratios (1:1, 1:2 and 1:5) were obtained from the 96-well screening plate, which was setup along with the published condition. The optimization of the conditions yielded reproducible crystals only in 1:1 and 1:2 in sodium phosphate condition (not shown) and in 1:5 protein:peptide ratio in lithium sulfate condition within one day (Figure 3.20C). After one week, crystals were also obtained in 1:5 protein:peptide ratio in the published condition (2.2 M Ammonium sulphate, 0.1 M HEPES pH 7.5) (Figure 3.20B). The crystal from sodium phosphate condition (1:2) was tested at the home source (Bruker Microstar-H rotating anode with Mar345 detector) which confirmed the absence of bound peptide in the crystals. Further, 1.6 Å and 1.4 Å datasets were collected from the crystals obtained from lithium sulfate (1:5) condition (3.20C) and ammonium sulfate (1:5) condition (3.20B), respectively. No residual density was observed for the bound peptide in both the datasets. However, superposition of our newly determined 1.4 Å KIX-1-10 structure (Figure 3.20D) with the published 1-10-KIX structure (PDB ID:4I9O) showed that the loop region (aa 612-624), located nearby the MLL pocket and between helices α1 and α2, is significantly moved (Figures 3.20E-F) and includes a sulfate ion. This indicates that the presence of the BMAL1 peptide may have forced the displacement of the loop region to draw a more favorable conformation of KIX to be able to bind itself. However, further mutational and structural studies will be required to probe the importance of this loop region of the KIX domain for BMAL1 binding. We also note that in our crystals (Fig. 3.20B), crystal packing contacts in the vicinity of this KIX loop region would have prevented peptide binding in or nearby the MLL pocket.

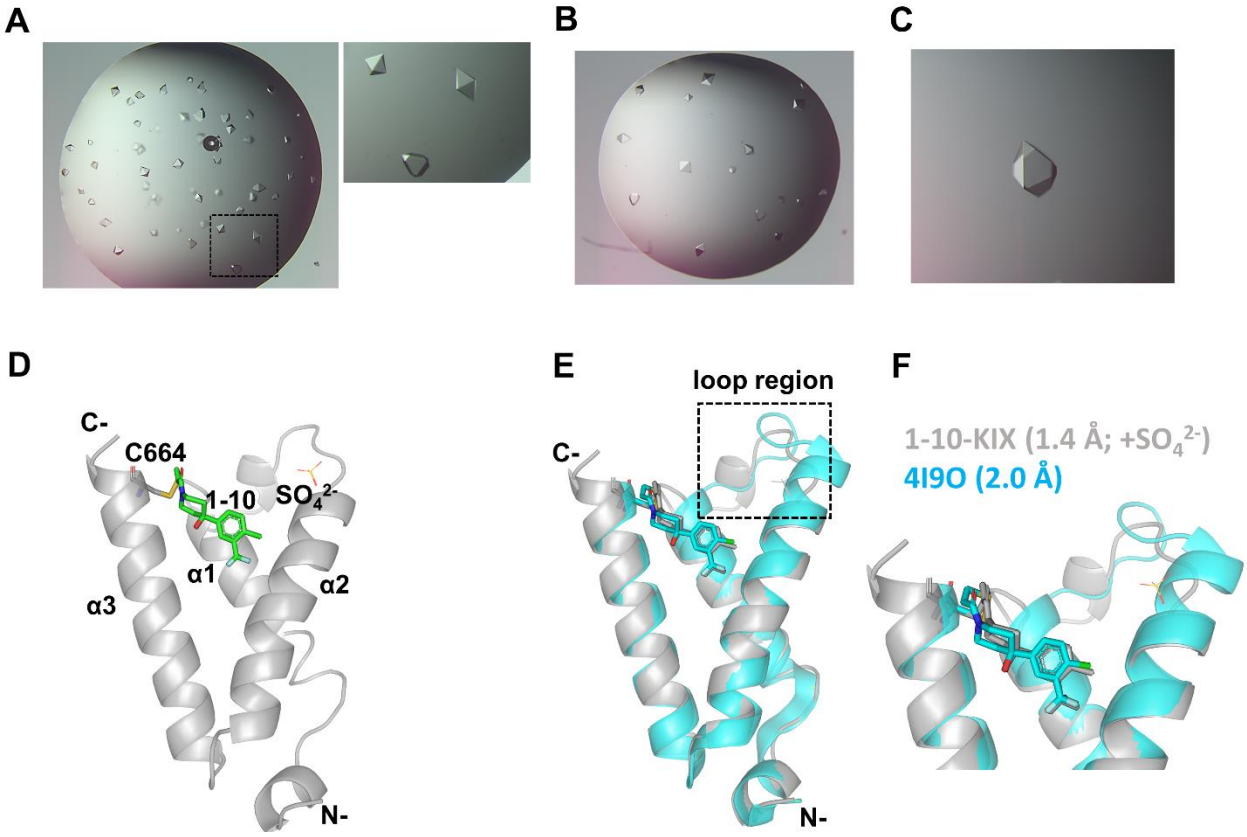

Figure 3.20 Crystallization of the complex of 1-10-KIX(L664C) with a 21-mer BMAL1 TAD peptide. Initial crystallization was setup with the published condition (1.8-2.2 M ammonium sulfate, 0.1 M Tris pH 7.5/HEPES pH 7.0) of KIX-1-10 (Wang et al., 2013a). Crystals were obtained within 1 day using a 1:1 and 1:2 protein:peptide ratio (A). The square marked the enlarged area shown in the right panel. The presence of 1-10-KIX in the crystals was confirmed by SDS-PAGE (silver stain), but the BMAL1-peptide could not be visualized. After one week, crystals appeared in a 1:5 protein:peptide ratio in 2.2 M ammonium sulfate, 0.1 M HEPES pH 7.5 (B), from which the structure of KIX-1-10 (without peptide) was solved at 1.4 Å resolution (D). An additional condition also yielded crystals from a 1:5 protein:peptide ratio (C), which resulted in a 1.6 Å structure of 1-10-KIX without peptide (not shown). (D-F): The superposition of our newly determined 1.4 Å KIX-1-10 structure (D) with the published structure of 1-10-KIX (PDB: 4I9O, cyan, 2.0 Å) showed the presence of a sulfate ion in a loop region near the MLL pocket (marked with square), which moved significantly in the new KIX-1-10 structure (grey) (E). The enlarged area around the loop region is shown in (F).

Table 3.4. X-ray data collection and refinement statistics of 1-10-KIX(L664C) co-crystallized with BMAL1 21-mer peptide (related to Figure 3.20 B, D-F)

	1-10-KIX(L664C) + Peptide
Content crystallization setup	CBP-KIX(L664C) (aa 586-672) Compound 1-10 (Wang et al., 2013a) BMAL1 peptide (aa 593-613)
Content crystal structure	1-10-KIX(L664C) (aa 588-564) 1 SO_4^{2-} ion
Data Collection Statistics	
Beamline	SLS X10SA (PXII)
Space group	$P4_3\,2_1\,2$
Wavelength (Å)	1.000033
Cell dimensions a, b, c (Å) α, β, ϒ (°)	 45.54, 45.54, 90.17 90, 90, 90
Resolution range*	40.65 – 1.40 (1.436 – 1.40)
Completeness (%)*	99.95 (100)
Wilson B-factor (Å^2)	24.02
Refinement Statistics	
Resolution range	40.65 – 1.40
Reflections Used in the refinement Used for R-free	 18452 971
R_{work} (%)	14.2
R_{free} (%)	21.3
Ramachandran values Favored region (%) Allowed region (%) Outliers (%) Average B-factor (Å^2) R.m.s.d bonds (Å) R.m.s.d angles (°)	 98.73 100 0.00 26.43 0.033 2.753

* The values in parenthesis correspond to the highest resolution shell.

3.3 Biochemical and biophysical analyses of BMAL1-KIX interactions

3.3.1 Effect of the acetyl-lysine mimetic BMAL1 K537Q mutation on binding of KIX

The acetylation of BMAL1 at Lys-537 enhances its binding to CRY1 and the subsequent transcriptional repression of CLOCK:BMAL1 (Czarna et al., 2011; Hirayama et al., 2007). In this thesis, the effect of the acetyl-lysine mimetic K537Q mutation was determined on the interaction of BMAL1 with the KIX domain. In the purified BMAL1 protein, the acetyl-lysine mimetic K537Q mutation mirrors the *in vivo* effect of Lys537 acetylation by increasing the CRY1-binding affinity to the BMAL1-TAD (Czarna et al., 2011, 2013). To determine the binding affinity of KIX for wild-type BMAL530 and BMAL530(K537Q), nano-Surface plasmon resonance (nanoSPR) and microscale thermophoresis (MST) experiments were performed. For MST measurements, the purified BMAL1 proteins were fluorescently labeled on the N-terminal His_6-tag and titrated with increasing concentrations of KIX protein (see Materials and methods- section 2.2.14). Similar binding affinities were obtained for the interaction of the wild-type BMAL530 and the BMAL530(K537Q) mutant with the KIX domain (Figure 3.21A-C), suggesting that the binding of BMAL1 to KIX domain is not affected by the lysine acetylation in contrast to the interaction of BMAL1 and CRY1 (Czarna et al., 2011). Likewise, the BMAL1 affinity for KIX is not affected by the P624A mutation (Figure 3.21), which locks the W623-P624 imide bond at the distal C-terminus of BMAL1 in the *trans* conformation, as reported previously (Gustafson et al., 2017). Notably, the binding affinities obtained in MST measurements are lower (still in µM range) compared to the values measured in nanoSPR experiments and to the previously reported binding affinity (Gustafson et al., 2017), which is possibly due to the N-terminal His_6-tag or the interference of the Red-Tris-NTA NT-647 dye used for His_6-tag labeling.

The analysis of MST and nanoSPR measurements using the Hill equation suggested the positive cooperative binding for BMAL1 and KIX indicated by the Hill coefficients (N) greater than 1 (Figure 3.22). The positive cooperativity may possibly be due to the presence of more than one BMAL1-binding motifs within KIX domain which has been investigated in the following sections.

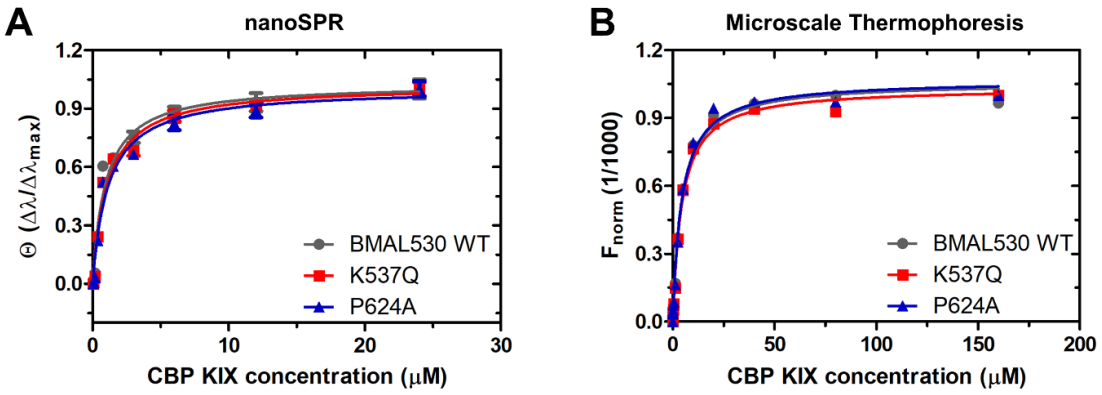

C

CBP KIX	nanoSPR K_D (μM)	MST K_D (μM)
BMAL530 WT	0.96 ± 0.22	4.45 ± 0.46
BMAL530 K537Q	1.09 ± 0.22	4.45 ± 0.43
BMAL530 P624A	1.15 ± 0.25	4.42 ± 0.47

Figure 3.21 Effect of the K537Q mutation mimicking Lys-537 acetylation of BMAL1 on KIX-binding affinity (A) Affinity analysis by nanoSPR. Data points correspond to the normalized mean plasmon shift $\Delta\lambda_{res}$ measured on 30–50 nanoparticles covered by His_6-BMAL530 WT or P624A and K537Q mutants titrated with increasing concentrations of WT KIX (0.04-25 μM). The standard error of the mean is indicated by the error bars. (B) Affinity analysis by MST. The KIX was titrated in increasing concentrations (0.005-160 μM) against 50 nM fluorescently labeled His_6-BMAL530 WT or P624A and K537Q mutants. The normalized fluorescence was plotted against the ligand concentration and best fits were obtained using a one-site binding model. (C) Dissociation constants obtained from nanoSPR and MST measurements. The binding affinity of BMAL1 for KIX was not affected by the P624A mutation as previously described (Gustafson et al., 2017). Also, the identical affinities of KIX for BMAL530 WT and BMAL530(K537Q) indicated no effect of BMAL1 acetylation on its interaction with the KIX domain. Adopted from (Garg et al., 2019).

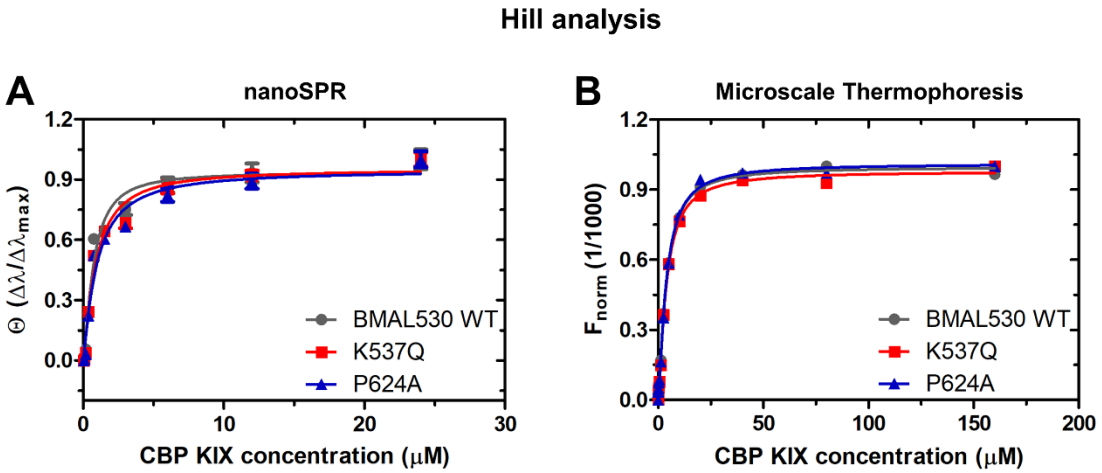

C

CBP KIX	nanoSPR		MST	
	K_D (μM)	N (Hill)	K_D (μM)	N (Hill)
BMAL530 WT	0.73 ± 0.12	1.5 ± 0.3	3.82 ± 0.19	1.4 ± 0.08
BMAL530 K537Q	0.88 ± 0.17	1.3 ± 0.2	3.84 ± 0.22	1.3 ± 0.08
BMAL530 P624A	0.96 ± 0.22	1.2 ± 0.3	3.88 ± 0.24	1.3 ± 0.09

Figure 3.22 Hill analysis of the nanoSPR and MST experiments to determine the effect of K537Q and P624A mutation on the affinity of BMAL1 for KIX domain. (A) nanoSPR measurements. (B) MST measurements. The measurements were performed as described in Figure 3.21. The best fits were obtained using one-site binding model with the Hill slope. (C) The dissociation constants and the corresponding Hill coefficients obtained from the Hill analysis of nanoSPR and MST experiments. The Hill coefficients greater than 1 suggest the positive cooperative binding behavior of BMAL1 and KIX.

3.3.2 Effect of mutations in MLL-binding pocket and 1-10 tethering on KIX affinity for BMAL1

Microscale Thermophoresis and Fluorescence Polarization

The mutations L664C and N627C on opposite sides of the MLL-binding pocket were introduced (refer to Introduction, Figure 1.8) and the compound 1-10 was tethered to C664 or C627 (refer to section 3.1.2) to analyze the role of the MLL-binding pocket of KIX domain in its interaction with BMAL1. The completeness of the tethering was analyzed using mass spectrometry and

found to be >97% and >99% complete for KIX(L664C) and KIX(N627C), respectively (Figures 3.5 and 3.8). The effect of the mutations L664C and N627C and of compound 1-10 on the binding affinities of KIX domain for BMAL1 was determined by MST and fluorescence polarization (FP) experiments. As shown by our nanoSPR and MST measurements (Figures 3.21 and 3.22) and also previously described (Gustafson et al., 2017), the P624A mutation in the C-terminal end of BMAL1, which locks W623-P624 imide bond into *trans* conformation, does not affect the BMAL1 binding affinity to KIX. Therefore, for affinity measurements with the wild-type KIX and mutants, we used the BMAL530(P624A) mutant protein due to its enhanced stability during purification.

For MST and FP experiments, the purified BMAL530(P624A) was fluorescently labeled (refer to section 2.2.13) on the N-terminally fused His_6-tag and titrated with the increasing concentrations of KIX protein (see Materials and methods-sections 2.2.14 and 2.2.15). The KIX domain binds to BMAL1 with about 5 µM affinity in both MST as well as FP experiments. As described in section 3.3.1, the obtained affinity is lower than previously reported (Gustafson et al., 2017), which is possibly due to the interference of the labeled N-terminally fused His_6-tag. Interestingly, the BMAL1 binding affinity for KIX was reduced by about 2- to 2.5-fold upon tethering the compound 1-10 to C664 or C627 in both MST (Figures 3.23A and 3.23B) as well as in FP (Figures 3.23C and 3.23D) measurements. Furthermore, the L664C mutation only slightly reduced the BMAL1 binding affinity as analyzed by FP experiments while N627C mutation enhanced the binding affinity by 1.5-fold in MST and 3-fold in FP experiments compared to the wild-type KIX. The Hill analysis of MST measurements (Figure 3.24 and table 3.5) suggested the positively cooperative binding behavior for BMAL1 and KIX interaction and the cooperativity was lost upon tethering of compound 1-10 in the MLL-binding pocket. Surprisingly, the Hill analysis of FP measurements resulted in overall lower affinity values and the Hill coefficients less than 1. The manual constraining of the Hill coefficients equal to the values obtained by the Hill analysis of MST measurements resulted in the dissociation constants comparable to that of obtained by MST and with satisfactory fitting values (data not shown). Altogether, these results suggest that the MLL-binding pocket plays a role in the interaction of KIX with BMAL1.

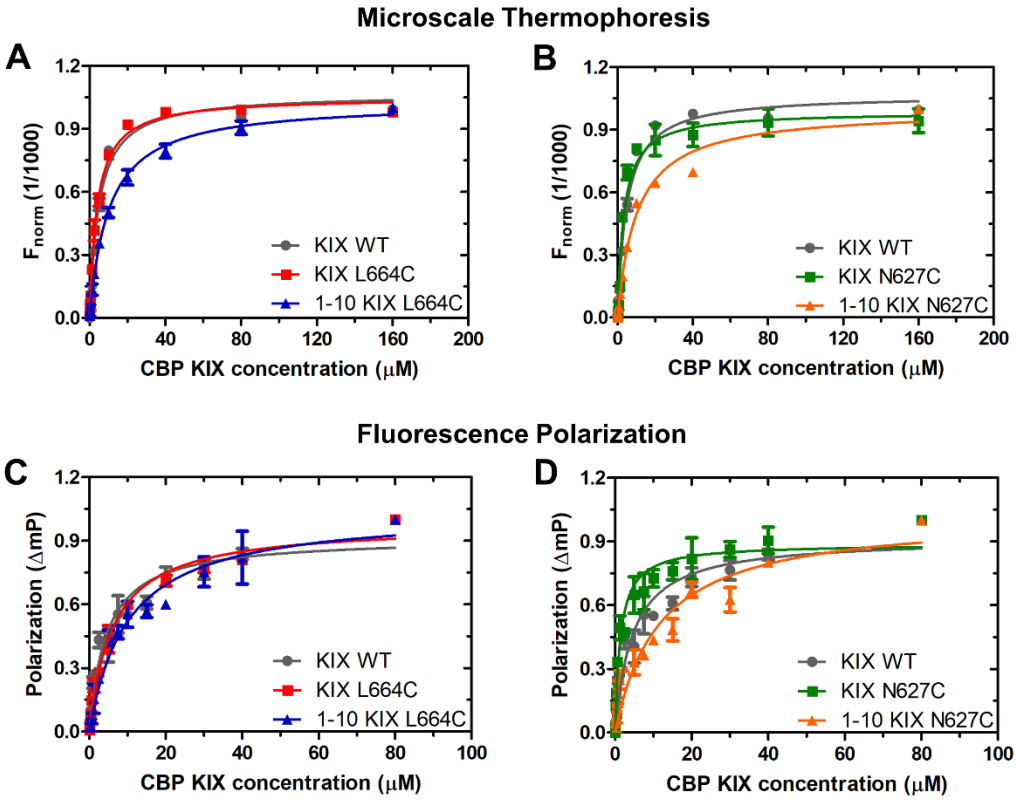

E **Dissociation constants**

BMAL530 P624A	MST K_D (μM)	FP K_D (μM)
KIX WT	4.88 ± 0.38	4.55 ± 0.86
KIX L664C	3.98 ± 0.22	6.15 ± 0.70
1-10 KIX L664C	10.14 ± 0.66	10.05 ± 1.59
KIX N627C	3.35 ± 0.42	1.40 ± 0.25
1-10 KIX N627C	10.17 ± 0.92	11.63 ± 2.56

Figure 3.23 Effect of mutations in MLL-binding pocket and 1-10 tethering analyzed by microscale thermophoresis (MST) and fluorescence polarization (FP). Analyses of the interaction of His_6-BMAL530(P624A) titrated with increasing concentrations of wild-type (WT) KIX and KIX mutants L664C (A, C) or N627C (B, D) untethered and tethered with compound 1-10 measured by MST (A, B) and FP (C, D) experiments. The concentration of Red-Tris NTA-647-labeled His_6-BMAL530(P624A) concentration was kept constant at 50 nM and titrated with varied concentrations (0.005 μM to 160 μM for MST and 0.04 μM to 80 μM for FP experiments) of unlabeled wild-type KIX and mutant proteins. The normalized fluorescence (MST) or polarization (FP) values were plotted against the ligand concentration and the best fits were obtained using a one-site binding model. The ~2-fold lower affinity of 1-10-tethered KIX suggests the role of the MLL-binding pocket in BMAL1 interactions. (E) Dissociation constants (K_D) for BMAL1-KIX interactions obtained from MST and FP. The values are the mean of two or three independent measurements. Adopted from (Garg et al., 2019).

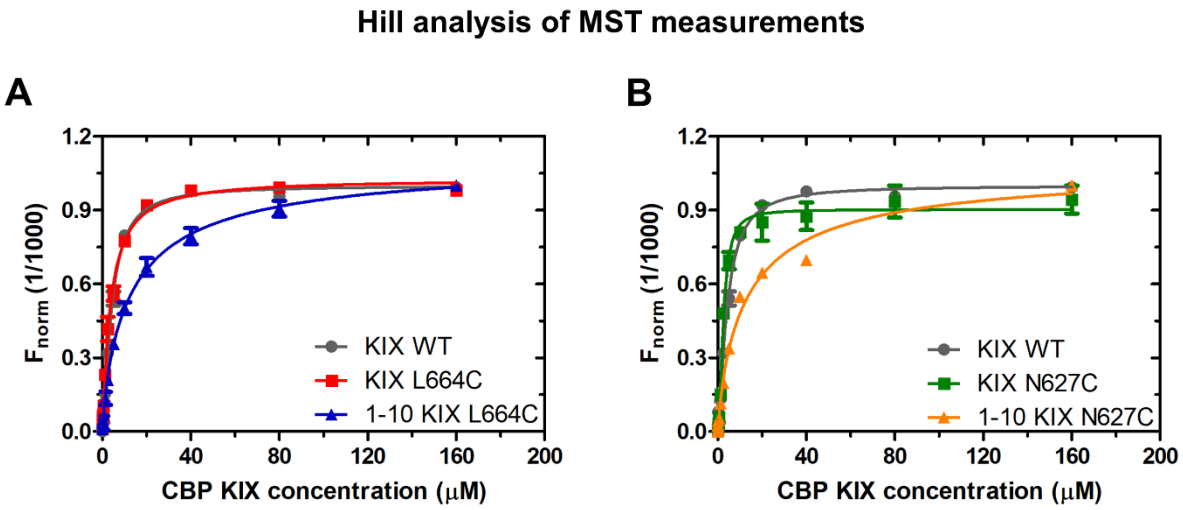

Figure 3.24 Hill analysis of the MST experiments to determine the effect of mutations in MLL-binding pocket and 1-10 tethering on the affinity of KIX domain for BMAL1. (A, B) MST measurements for interaction of His_6-BMAL530(P624A) with wild-type (WT) KIX and untethered/1-10-tethered KIX(L664C) (A) and untethered/1-10-tethered KIX(N627C) (B). The measurements were performed as described in Figure 3.23. The best fits were obtained using one-site binding model with the Hill slope. The dissociation constants (K_D) and the corresponding Hill coefficients obtained from the Hill analysis of MST experiments are given in Table 3.5.

Table 3.5 MST and FP dissociation constants (K_D) and Hill analysis of MST measurements

BMAL530 P624A	MST	MST (Hill analysis)	
	K_D (μM)	K_D (μM)	N (Hill)
KIX WT	4.88 ± 0.38	4.18 ± 0.19	1.4 ± 0.08
KIX L664C	3.98 ± 0.22	3.72 ± 0.21	1.1 ± 0.06
1-10 KIX L664C	10.14 ± 0.66	12.87 ± 1.49	0.8 ± 0.05
KIX N627C	3.35 ± 0.42	2.54 ± 0.16	1.9 ± 0.19
1-10 KIX N627C	10.17 ± 0.92	13.32 ± 2.1	0.8 ± 0.06

3.3.3 GST pull-down assay of MLL1-TAD with BMAL1 and KIX

For quantitative biophysical and structural analyses of KIX-MLL1-TAD interactions, the MLL1-TAD 19-mer peptide (aa 2840-2858) [denoted as MLL19] was used (Brüschweiler et al., 2013; Goto et al., 2002), which includes the minimal region (aa 2844-2854) shown to be important for

transactivation as well as for interaction with the KIX domain (Ernst et al., 2001; Prasad et al., 1995). In this study, the human MLL19 was cloned and purified as the His_6-GST-fusion protein (section 3.1.3, Figure 3.12) to test the ternary complex formation between MLL1-TAD, BMAL1-TAD and KIX domain. The GST pull-down assay was performed with His_6-GST-MLL19 as bait by either simultaneously adding the two individually purified BMAL530 and KIX proteins as prey or using the preformed BMAL530:KIX complex as prey (Figure 3.25A). Interestingly, only KIX was pulled down by MLL19, when incubated with both KIX and BMAL1 proteins (Figure 3.25A, lane 3), and even KIX was sequestered by MLL19 from the preformed BMAL1:KIX complex (Figure 3.25A, lane 5). In comparison, this effect was not observed in control pull-downs using GST as bait with either individual proteins as prey (Figure 3.25A, lane 2), BMAL530:KIX complex as prey (Figure 3.25A, lane 4) or only KIX as prey (Figure 3.25B, lane 9). This assay showed that a ternary complex cannot be formed *in vitro* between MLL1-TAD, BMAL1-TAD, and CBP-KIX domain and further confirmed the importance of the MLL-binding pocket of KIX for interaction with BMAL1.

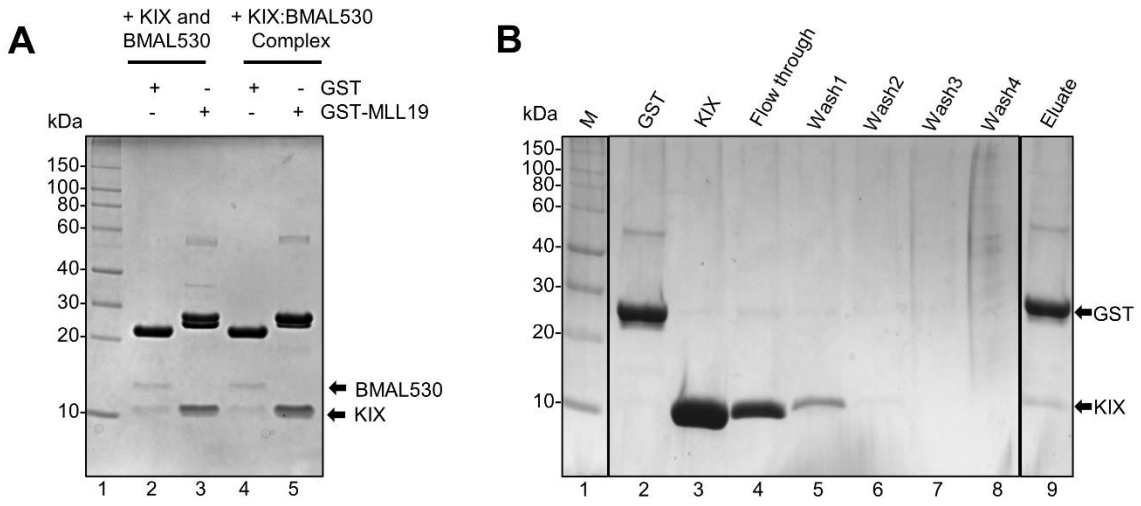

Figure 3.25 GST pull-down experiment. (A) The His_6-GST-MLL19 (bait) was incubated either with individually purified KIX and BMAL530 proteins (prey) or with preformed BMAL530:KIX complex (prey). The MLL19 only pulled down KIX when incubated with individual BMAL530 and KIX proteins (lane 3) and sequestered KIX from the preformed KIX:BMAL530 complex (lane 5) compared to the control pull-downs with GST only (lane 2 and 4). The faint bands of BMAL530 and KIX in control lanes (lane 2 and 4) might be due to the stickiness of GST described in section 3.2.1. The lane 1 shows the protein marker. (B) The negative control pull-down using only GST as bait and KIX as prey. The GST alone could not pull-down KIX (lane 9) and most of the KIX protein was found in flow-through and wash fractions (lanes 4-8). The lanes 2 and 3 show purified GST and KIX proteins. M=protein marker.

3.3.4 Effect of mutations in the MLL- and c-Myb/CREB-pKID binding pocket of KIX by nanoSPR

Nano-Surface Plasmon Resonance

To discern the role of the second c-Myb/CREB-pKID binding pocket of KIX in BMAL1-KIX interactions and to further confirm the role of the MLL-binding pocket, the effect of tethering of compound 1-10 and of mutations in both pockets of KIX domain on binding affinities of BMAL1 was determined by nanoSPR using single plasmonic nanoparticles as nanosensors (Ahijado-Guzmán et al., 2014, 2017; Ye et al., 2018b). For nanoSPR measurements, the gold nanorods functionalized with the N-terminal His_6-tagged wild-type KIX domain or mutants were utilized as sensors and the increasing concentrations of untagged BMAL530(P624A) protein were passed through the flow cell until the equilibrium state was achieved (see Materials and methods, section 2.2.16). After 10 minutes, the wavelength shift of about 1400 particles was measured to obtain 80-200 data points for each protein group corresponding to the wild-type or mutant KIX proteins. The nanoSPR measurements allow for an internal comparison of the BMAL1 affinity values obtained for different KIX mutations in the MLL- and c-Myb/pKID-binding pockets as the affinities for wild-type and mutant KIX proteins were measured within the same titration and flow cell.

Here, in this experiment, the wild-type KIX domain was found to bind BMAL1 with an affinity of ~ 0.6 μM which is in the range reported previously (Gustafson et al., 2017). The obtained affinity values are slightly higher compared to the values obtained in the nanoSPR measurements described in section 3.3.1 (~ 1 μM). We propose that the slightly lower affinity values obtained in the section 3.3.1 are due to the His_6-BMAL1 being a surface-bound receptor and KIX is the titrated ligand compared to the experiment described in this section. This is consistent with our hypothesis that the overall lower affinities measured in MST and FP compared to nanoSPR are due to the labeled N-terminal His_6-tag of BMAL1. Altogether, KIX interactions somehow appear to be affected by the manipulation of the N-terminal end of BMAL530, but this is unrelated to Lys537 acetylation. Furthermore, the binding of BMAL1 was either weakened or enhanced by the mutations L664C and N627C, respectively (Figures 3.26A, B and D), which lie opposite to each other in the MLL-binding pocket of KIX. In qualitative agreement with the MST and FP

measurements, the BMAL1 affinity was further lowered by about two-fold by tethering compound 1-10 in the MLL-binding pocket resulting in the affinities of ~1.5 µM and ~1.3 µM for 1-10-KIX(L664C) and 1-10-KIX(N627C), respectively. These results further confirmed the role of MLL-binding pocket in the KIX-BMAL1 interaction. Notably, the MLL1-TAD binding affinity for the KIX domain has been reported to weaken much more significantly by about 100-fold upon tethering with compound 1-10 (Wang et al., 2013a), suggesting that a different binding mode is used by BMAL1 compared to MLL1. Furthermore, additional binding interfaces e.g. in the second KIX binding pocket may stabilize BMAL1 binding.

The role of the second c-Myb/pKID-binding pocket in BMAL1 interactions was analyzed by measuring the BMAL1 binding affinities to KIX proteins with a double Y650A/A654W and a single Y658A mutation in the shallow groove of this pocket (Figure 3.26C and D). The circular dichroism (CD) spectra showed that both mutant KIX proteins retained their secondary structure (Figure 3.11) and the structural contents were found to be similar to wild-type KIX. The nanoSPR measurements showed that the affinity of KIX for BMAL1 was lowered by about 2- to 2.5-fold by Y650A/A654W double mutation, while less pronounced effects were observed for the Y658A mutant (Figures 3.26 C and D). In contrast, the binding of CREB-pKID and c-Myb to KIX domain was found to weaken substantially by the mutations of Y658, Y650 and A654 (Parker et al., 1999). Therefore, BMAL1 appears to exploit the second KIX binding pocket in a different manner than CREB-pKID and c-Myb.

The Hill analysis of nanoSPR measurements (Figure 3.27) suggested the positive cooperative binding behavior for BMAL1 and KIX interaction and the cooperativity was lost upon tethering of compound 1-10 to KIX(N627C) consistent with the MST measurements. Surprisingly, the tethering of compound 1-10 to KIX(L664C) retained the positive cooperativity in nanoSPR measurements contrary to the values obtained from MST. Interestingly, the double mutation (Y650A/A654W) in the c-Myb/pKID-binding pocket also showed to lose the cooperative binding behavior of BMAL1 and KIX. Altogether, these results suggest that both KIX binding pockets play a role in BMAL1 binding and the cooperative binding is lost upon interfering with either pockets of the KIX domain.

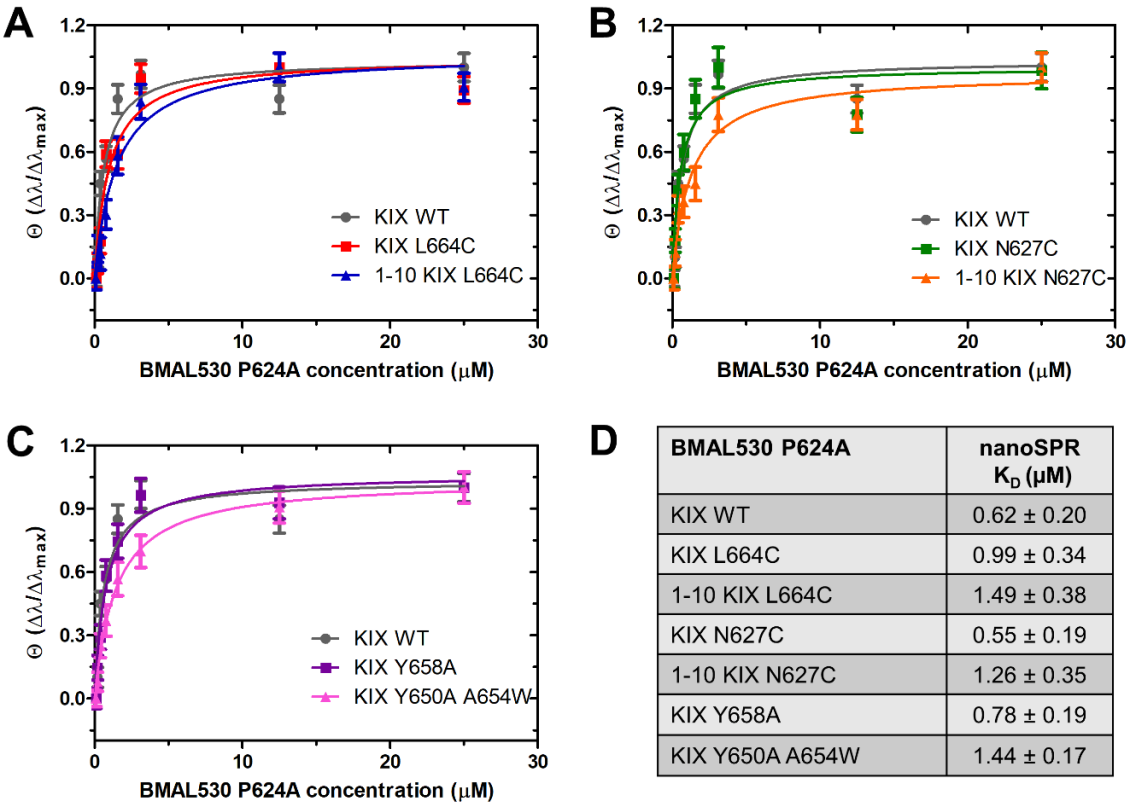

BMAL530 P624A	nanoSPR K_D (μM)
KIX WT	0.62 ± 0.20
KIX L664C	0.99 ± 0.34
1-10 KIX L664C	1.49 ± 0.38
KIX N627C	0.55 ± 0.19
1-10 KIX N627C	1.26 ± 0.35
KIX Y658A	0.78 ± 0.19
KIX Y650A A654W	1.44 ± 0.17

Figure 3.26 Effect of mutations in MLL-binding pocket, 1-10 tethering and mutations in pKID/c-Myb-binding pocket analyzed by nano-Surface Plasmon Resonance (nanoSPR). The Ni-NTA functionalized gold nanorods were covered with the receptor proteins: His_6-tagged wild-type KIX (A-C), compound 1-10 tethered/untethered KIX(L664C) (A), 1-10 tethered/untethered KIX(N627C) (B) and KIX(Y658A), KIX(Y650A/A654W) mutated in the c-Myb/pKID-binding pocket (C) and titrated with the untagged BMAL530(P624A) protein (0.01-25 μM) and plasmon resonance wavelength shifts ($\Delta\lambda_{res}$) were recorded. The data points correspond to the normalized mean plasmon shift $\Delta\lambda_{res}$ measured on 80–200 nanoparticles for each receptor. The standard error of the mean is indicated by the error bars and the best fits were obtained using a one-site binding model in GraphPad Prism. (D) Dissociation constants (K_D) obtained from nanoSPR measurements. The affinity of KIX for BMAL1 was lowered by tethering of compound 1-10 by about 2-fold, consistent with the MST and FP measurements (Figure 3.23). The KIX-BMAL1 interaction was also destabilized by the mutations in the c-Myb/pKID-binding pocket suggesting that both KIX binding pockets play a role in BMAL1 interactions. Adopted from (Garg et al., 2019).

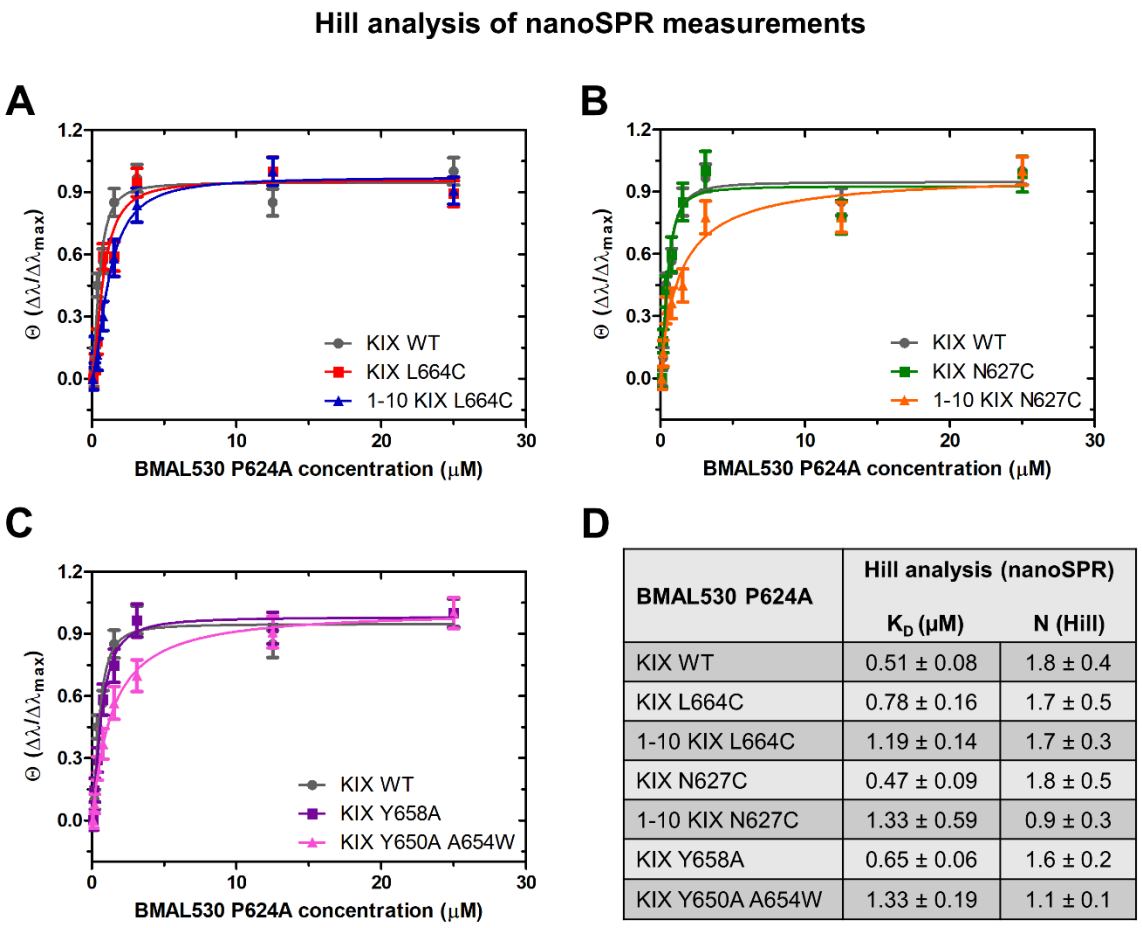

BMAL530 P624A	Hill analysis (nanoSPR)	
	K_D (μM)	N (Hill)
KIX WT	0.51 ± 0.08	1.8 ± 0.4
KIX L664C	0.78 ± 0.16	1.7 ± 0.5
1-10 KIX L664C	1.19 ± 0.14	1.7 ± 0.3
KIX N627C	0.47 ± 0.09	1.8 ± 0.5
1-10 KIX N627C	1.33 ± 0.59	0.9 ± 0.3
KIX Y658A	0.65 ± 0.06	1.6 ± 0.2
KIX Y650A A654W	1.33 ± 0.19	1.1 ± 0.1

Figure 3.27 Hill analysis of the nanoSPR experiments. (A, B, C) nanoSPR measurements for interaction of untagged BMAL530(P624A) with His_6-tagged wild-type (WT) KIX (A-C), untethered/1-10-tethered KIX(L664C) (A), untethered/1-10-tethered KIX(N627C) (B), and KIX(Y658A) and KIX(Y650A/A654W) mutants in the c-Myb/pKID-binding pocket (C). The measurements were performed as described in section 3.3.4. The best fits were obtained using one-site binding model with the Hill slope. (D) The dissociation constants (K_D) and the corresponding Hill coefficients (N) obtained from the Hill analysis of nanoSPR experiments.

3.3.5 Secondary structural analysis of BMAL1:KIX complex: Unraveling the folding behavior of BMAL1 upon complexation with KIX

Circular dichroism (CD) spectroscopy

The folding behavior of BMAL1 upon complex formation with the KIX domain was analyzed using CD spectroscopy. The secondary structural analyses of purified BMAL530 and KIX proteins

(described in section 3.2.2 and Figure 3.16) showed the KIX domain to be mostly helical (~58%) while BMAL1 was mostly unstructured and intrinsically disordered (~70%). Interestingly, after mixing the individually purified KIX and BMAL1 proteins, no pronounced changes were observed in the secondary structural content of the BMAL530:KIX complex over a course of time ranging from 30 min to overnight (~17 h) (Figure 3.28 and Table 3.6). Moreover, the experimental CD spectra of the BMAL530:KIX complex were found to be close to the calculated average of the CD spectra of individual BMAL1 and KIX proteins. Notably, the MST and FP affinity measurements (sections 3.3.1 and 3.3.2) were performed following a 30 min co-incubation of BMAL1 and KIX at each titrant concentration and even after 2 h and overnight co-incubation, comparable results were obtained. This indicated that the binding of BMAL1 and KIX occurs within 30 min and the lack of pronounced secondary structure changes suggested by the CD spectra is not due to a lack of BMAL1-KIX interactions. These results suggest that no major folding event takes place when BMAL1 binds to the KIX domain, unlike the binding-induced folding and structuring of pKID and c-Myb upon complexation with KIX domain (Gianni et al., 2012; Radhakrishnan et al., 1997). However, conformational rearrangements associated with minor secondary structural changes cannot be excluded, based on our CD spectra.

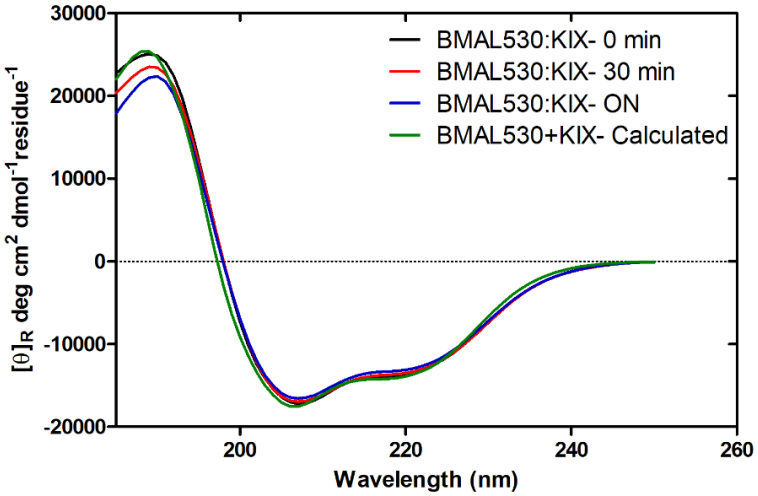

Figure 3.28 Secondary structural analyses of BMAL1-KIX interaction by circular dichroism (CD) spectroscopy. The incubation of BMAL530 with KIX (at time point 0 min) for a period of 30 min to overnight (ON, ~ 17 h) does not suggest major folding of BMAL1 upon complexation as indicated by almost identical spectra in the 208 nm and 222 nm region and high similarity of experimental and calculated complex spectra. The molar ellipticity per residue (MRE,

$[\theta]_R$) is plotted against the wavelength. The calculated (BMAL530+KIX) CD spectrum is the result of the averaged CD spectra of individual BMAL530 and KIX proteins. Adopted from (Garg et al., 2019).

Table 3.6 CD measurements suggest that BMAL1 does not fold upon complexation with the KIX domain (related to Figure 3.28)

	Helix[a]	Strand[a]	Turns	Unordered	N.r.m.s.d.[b]
BMAL530	0.083	0.104	0.111	0.702	0.032
KIX	0.579	0.062	0.182	0.177	0.016
BMAL530:KIX complex 0 min[c]	0.374	0.036	0.091	0.498	0.075
Complex 30 min[c]	0.363	0.046	0.123	0.468	0.079
Complex ON[c]	0.346	0.081	0.153	0.419	0.064
Calculated for complex[d]	0.311	0.086	0.144	0.460	0.093

[a] Helix and strand: include regular and distorted helices and strands.

[b] N.r.m.s.d. = Normalized root mean square deviation.

[c] Incubation time after mixing BMAL530 and KIX proteins at time point 0 min, 30 min and ON; ON = overnight (~ 17 h).

[d] Deconvolution of averaged CD spectra of individual BMAL530 and KIX proteins.

Spectra were deconvoluted using the CONTIN algorithm with reference dataset 6 (Sreerama and Woody, 2000) in the DichroWeb server (Whitmore and Wallace, 2004).

3.3.6 Static light scattering (SLS) analysis of BMAL530, KIX and their complex

As BMAL530 protein runs aberrantly in SDS-PAGE and elutes at a higher volume in SEC compared to its theoretical molecular weight (section 3.2.2), the molecular weights of the individual BMAL530 and KIX proteins as well as their complex were determined precisely by static light scattering (SLS). Averaging the mass values in the peak region yielded mean molecular weights of 11.66 ± 0.87 kDa for BMAL530, 12.30 ± 1.04 kDa for KIX and 16.46 ± 0.94 kDa for the BMAL530:KIX complex (Figure 3.29), which corresponds to a 1:1 complex (BMAL530:KIX). The obtained molecular weights from SLS are in agreement with the theoretical molecular weights and estimated molecular weights from SAXS measurements (section 3.3.7, table 3.7). The SLS measurements were conducted by Prof. Elmar Jaenicke, Institute of Molecular Physiology, JGU Mainz.

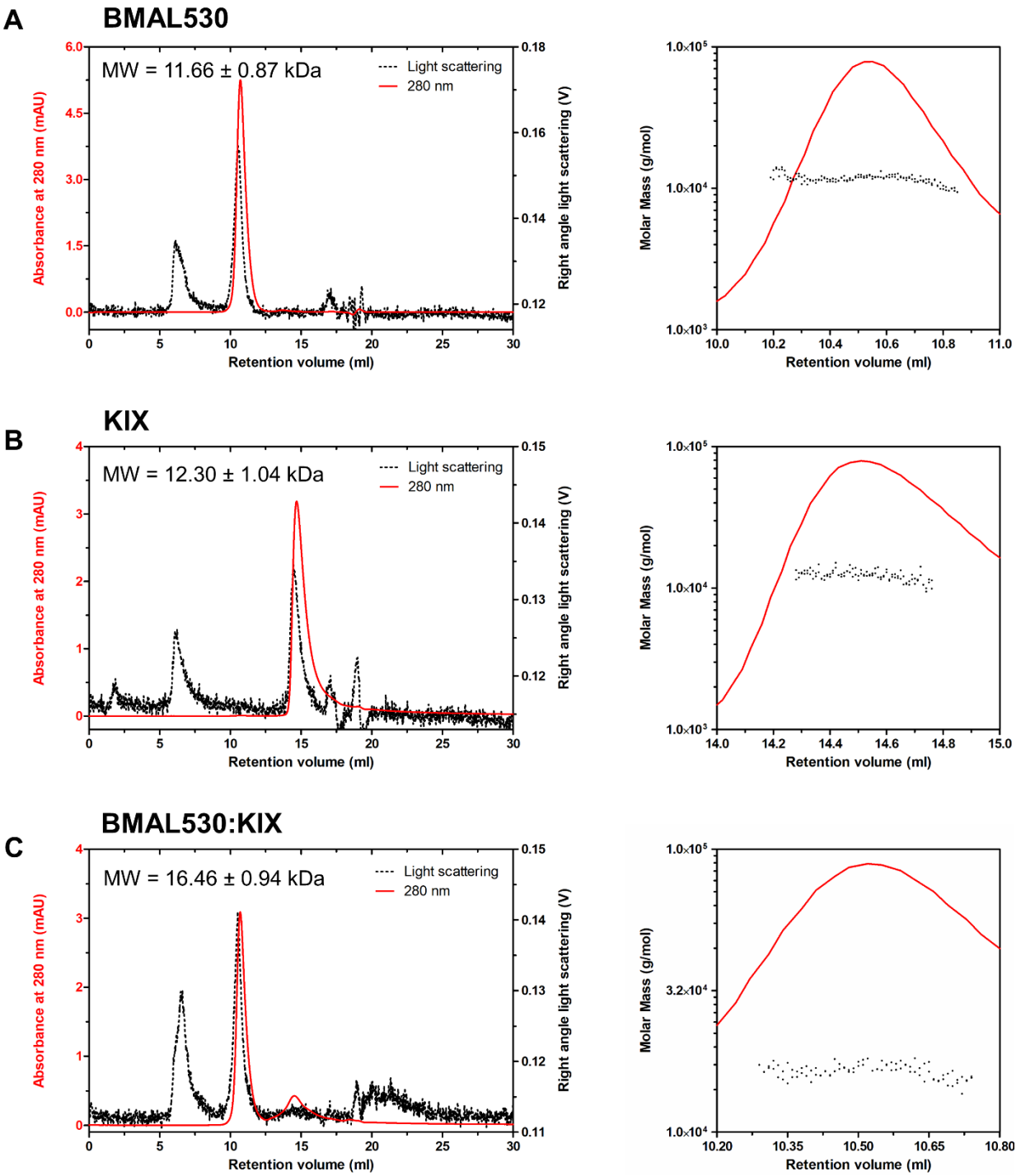

Figure 3.29 Determination of molecular weights of BMAL530 (A), KIX (B) and BMAL530:KIX complex (C) using static light scattering (SLS). The protein concentration was monitored by UV absorbance at 280 nm (red) and by light scattering (LS) at 90° (dotted black) during elution from the size-exclusion column (Superdex 75 10/300) [left panels]. The distribution of average molecular weight values in the peak region are represented by dots (right panels) and plotted in relation to the elution volume. The additional small LS peak observed at ~ 6 ml shows no UV absorbance indicating the 'system peak' which results from larger particles coming either from the HPLC system or due to shedding of the column.

3.3.7 Small-angle X-ray scattering (SAXS) analyses of the BMAL1:KIX complex

The individual BMAL1 and KIX proteins and their complexes were analyzed for their shapes, dimensions, folding and conformational flexibility by performing in-solution SAXS measurements. The SAXS measurements were performed for purified wild-type BMAL530 and BMAL530(P624A) proteins, the wild-type KIX domain, KIX(L664C) untethered and 1-10-tethered, and three BMAL1:KIX complexes: BMAL530:KIX (includes BMAL1(530-625)P624A), BMAL517:KIX (includes BMAL1(517-625)) and BMAL490:KIX (includes BMAL1(490-625)). All protein samples were free of aggregates as shown by the linearity of the plot between natural logarithm of intensity [ln(I)] and s^2 in the low q-region by Guinier analysis (Figures 3.30C, 3.31B and 3.32B).

BMAL530 proteins

The SAXS analyses were performed for individual wild-type (WT) BMAL530 and BMAL530(P624A) proteins. The BMAL1 proteins were found to be mostly unfolded and elongated in shape as suggested by Kratky plots (Figure 3.30B) which is consistent with the CD spectral analysis of BMAL530 (section 3.2.2). The estimated molecular weights (MW) for WT BMAL530 and BMAL530(P624A) proteins calculated using the Bayesian approach (Hajizadeh et al., 2018) are 11.25 kDa and 13.45 kDa, respectively (table 3.7) which is consistent with the experimental MW measured from SLS analysis (section 3.3.6). The MW credibility interval is estimated to be 9.95 kDa-13.80 kDa for both the proteins. The maximum particle dimensions (D_{max}) of BMAL530 and BMAL530(P624A) proteins are calculated from pairwise-distribution function, P(r) (Figure 3.30D) and found to be same (110 Å) for both the proteins. Further, the low-resolution models were calculated for both proteins by *ab initio* shape-determination using DAMMIF/N (Figures 3.30I-J) and GASBOR (not shown), which reasonably fit the experimental data (Figures 3.30 E-F, Table 3.7).

KIX proteins

The in-solution structural analyses of the individual wild-type KIX and KIX(L664C) untethered/compound 1-10 tethered were performed by SAXS. The Kratky plots suggested the KIX proteins to be compact and partially folded (Figures 3.30B and 3.31A) which is consistent with the CD results (section 3.2.2) and the published high-resolution structures (Radhakrishnan et al., 1997; Wang et al., 2013a; Zor et al., 2004). Using a Bayesian approach integrated in the Primus Qt (Hajizadeh et al., 2018), the molecular weights and MW credibility intervals were estimated to be 14.15 kDa and 13.10 kDa-15.80 kDa for KIX domain, 13.45 kDa and 11.65 kDa-13.80 kDa for untethered KIX(L664C) and 11.25 kDa and 9.95 kDa-11.65 kDa for 1-10-tethered KIX(L664C) proteins (table 3.7). The estimated MWs are consistent with the experimental MW of KIX measured by SLS experiments (section 3.3.6) and mass spectrometry (section 3.1.1).

From the pairwise distance distribution functions, P(r), the maximum particle dimensions (D_{max}) of KIX WT, untethered KIX(L664C) and 1-10-tethered KIX(L664C) were calculated to be 73 Å, 81 Å and 64.2 Å, respectively (Figures 3.30D and 3.31C). The maximum dimensions are consistent with the more compact KIX domain compared to the elongated shape of BMAL530 and also with the enhanced conformational stability of the 1-10 tethered KIX domain compared to untethered KIX (Wang et al., 2014). The output files from GNOM were utilized by the *ab initio* shape determination programs- DAMMIF/N and GASBOR to calculate the low-resolution models of KIX proteins. The models calculated from both the programs reasonably fit the experimental SAXS data (Figures 3.30G-H, 3.30K-L and Table 3.7).

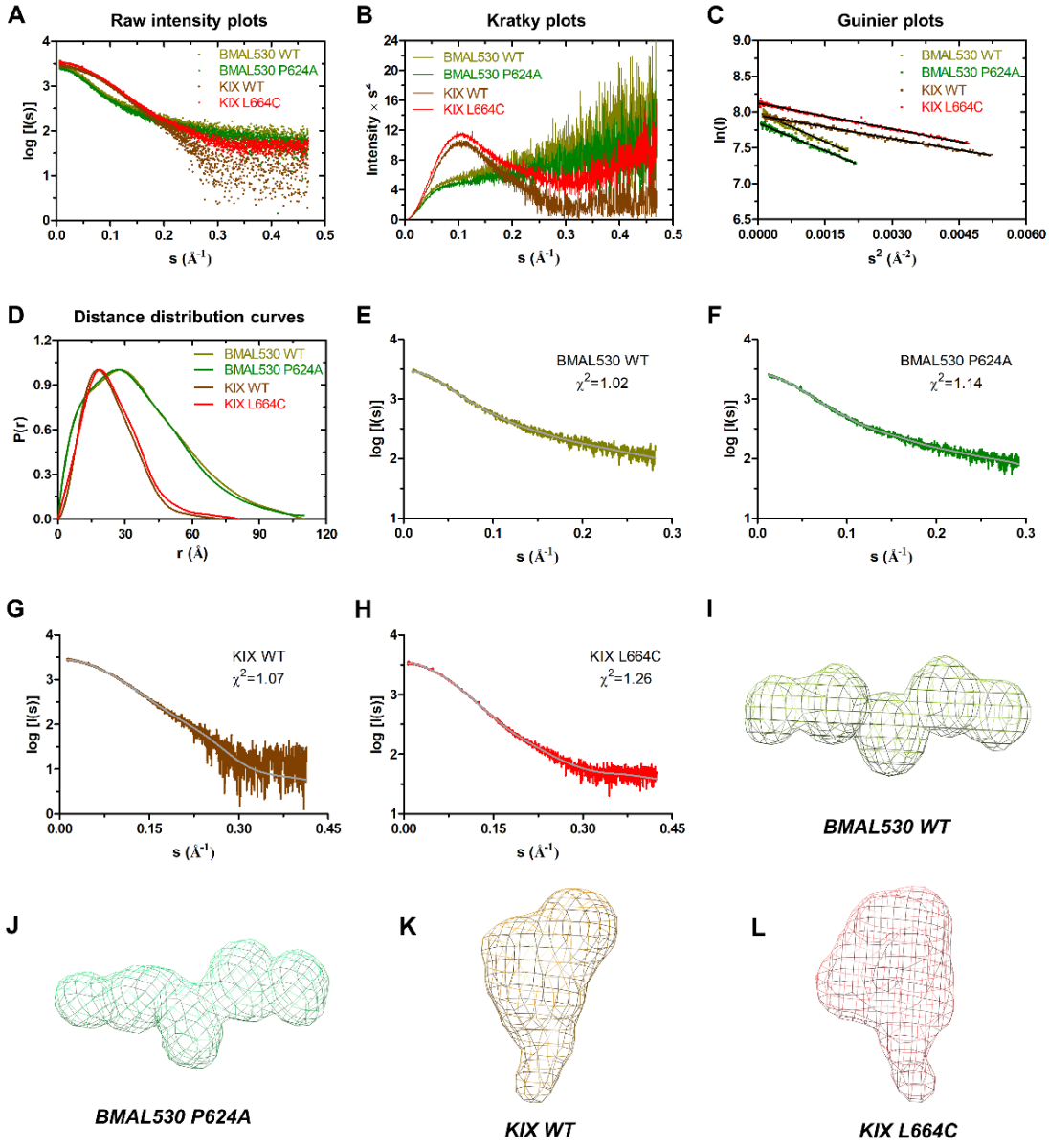

Figure 3.30 SAXS analyses of BMAL530 and KIX proteins. (A) Raw logarithmic intensity plots for wild-type (WT) BMAL530 (olive green), BMAL530(P624A) (green), KIX WT (brown) and KIX(L664C) (red). (B) The Kratky plots for BMAL530 WT, BMAL530(P624A), KIX WT and KIX(L664C); coloring as in panel A. BMAL1 showed a mostly unfolded character and an elongated shape, while KIX proteins are compact and partially folded. (C) The Guinier plots showed no aggregation of all four protein samples as indicated by the linear dependence of ln(I) vs s^2. (D) Distance distribution functions P(r) derived from the experimental SAXS data suggest maximum particle dimensions (D_{max}) of 110 Å for BMAL530 WT and BMAL530(P624A) and 73 Å and 81 Å for KIX WT and KIX(L664C), respectively; coloring as in panel A. (E-H) The best fits of the SAXS models (DAMMIF/N) of BMAL530 WT, BMAL530(P624A), KIX WT and KIX(L664C) (grey) to the experimental scattering data of BMAL530 WT (olive green) (E), BMAL530(P624A) (green) (F), KIX WT (brown) (G) and KIX(L664C) (red) (H). The chi square (χ^2) values close to 1 reflect a good fit. (I-L) The *ab initio* SAXS models calculated from DAMMIF/N for BMAL530 WT (I), BMAL530(P624A) (J), KIX WT (K) and KIX(L664C) (L). The maps were generated from the SAXS envelopes by Chimera (Pettersen et al., 2004). Adapted from (Garg et al., 2019).

Table 3.7 SAXS-derived properties of BMAL1, CBP-KIX and their complexes

Protein	R_g[a] (Å)	D_{max}[b] (Å)	χ^2[c] (DAMMIF/N, GASBOR)	MW_t[d] (kDa)	MW_E (C.I.)[e] (kDa)
BMAL530 WT	28.5	110	1.02, 1.08	9.7	11.25 (9.95-13.80)
BMAL530(P624A)	27.7	110	1.14, 1.21	9.7	13.45 (9.95-13.80)
KIX WT	17.9	73	1.07, 1.09	10.33	14.15 (13.10-15.80)
KIX(L664C)	18.9	81	1.26, 1.4	10.32	13.45 (11.65-13.80)
1-10-KIX(L664C)	17.2	64.2	1.21, 1.22	10.68	11.25 (9.95-11.65)
Complex BMAL530(P624A): KIX(L664C)	27.8	114.5	1.06, 1.13	20.02	19.93 (18.35-21.50)
Complex BMAL517:KIX	31.4	137	1.23, 1.36	21.30	21.18 (19.0-23.35)
Complex BMAL490:KIX	37.5	175	1.21, 1.29	24.17	33.10 (29.25-38.10)

[a] R_g = Radius of gyration derived from Guinier analysis.

[b] D_{max} = Maximum particle dimension derived from distance distribution function.

[c] χ^2: Chi square values show the best fits of the calculated models with the experimental SAXS data and the values close to 1 indicate a good fitting.

[d] MW_t = Theoretical molecular weight based on protein sequence.

[e] MW_E (C.I.) = Expected molecular weight calculated from a Bayesian inference approach (Hajizadeh et al., 2018) in the ATSAS 2.8.4 software package. C.I. indicates the credibility interval of molecular weight with 90-98% probability of finding the correct MW in the given range.

The radius of gyration (R_g) and the V-shape of the SAXS models calculated for KIX proteins from the experimental SAXS data agree with the 1-10-KIX crystal structure (PDB ID 4I9O). However, unsatisfactory fitting values (χ^2 = 4.73 (CRYSOL) and χ^2 = 9.24 (FoXS)) were obtained by fitting the theoretical scattering data calculated from the 1-10-KIX crystal structure to the experimental SAXS data (Figure 3.31D). The N- and C-terminal residues (G586, V587, E666-L672), that were not included in the 1-10-KIX crystal structure, were modeled (Figure 3.31F) which resulted in a much better fit to the experimental SAXS data (χ^2 = 1.51 (CRYSOL) and χ^2 = 1.49 (FoXS)) (Figure 3.31E). The MLL1:KIX complex NMR structure (PDB: 2LXS, eliminating the MLL1-peptide) is also used to position the KIX domain in the 1-10-KIX SAXS envelope as these residues are included in the NMR

structure and furthermore, the MLL-pocket is important for interaction with BMAL1 (sections 3.3.2-3.3.4) and binds the 1-10 compound (Wang et al., 2013a). The theoretical scattering profile obtained from the NMR structure fits well to the experimental SAXS data of 1-10-KIX (χ^2 = 1.57, CRYSOL). Further model optimization was performed using SREFLEX, which improved the fitting of the structure to the experimental SAXS data (χ^2 = 1.21 after SREFLEX) (Figure 3.31E).

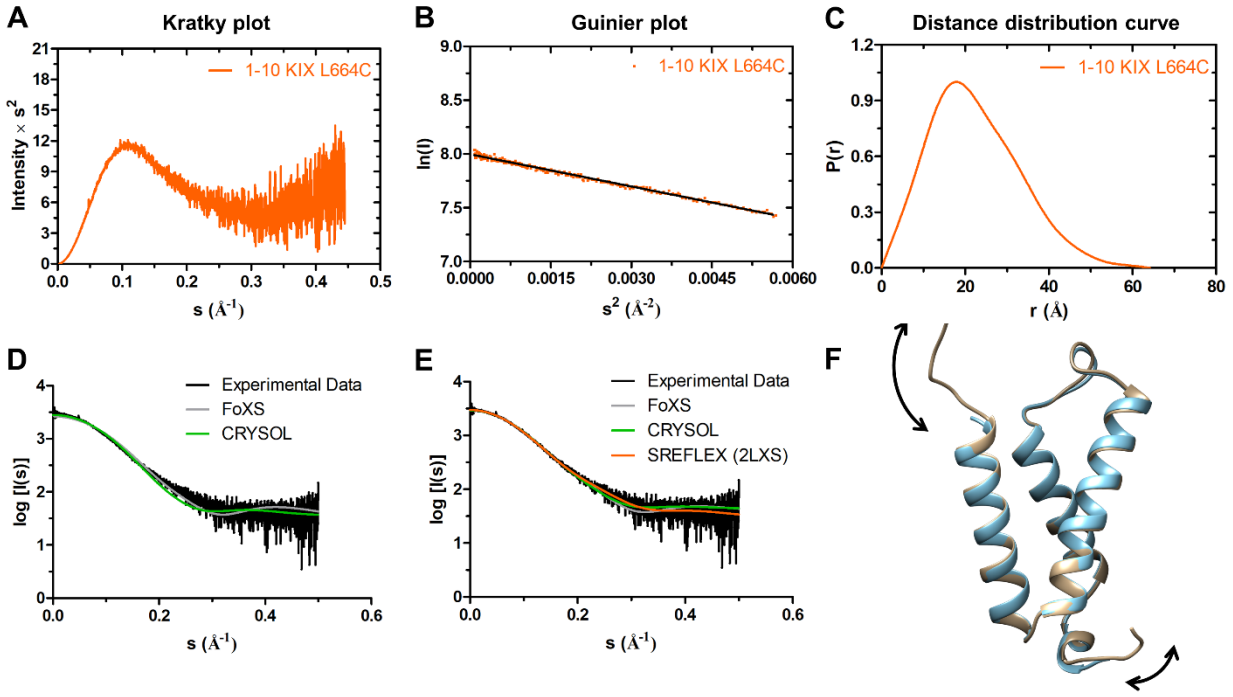

Figure 3.31 SAXS analyses of the 1-10 tethered KIX domain. (A) The Kratky plot for the 1-10 tethered KIX(L664C) domain indicates that it is compact and partially unfolded. (B) The Guinier plot shows no aggregation of the 1-10 tethered KIX(L664C) protein indicated by the linear dependence of ln(I) vs s^2. (C) The distance distribution function P(r) derived from the experimental SAXS data for 1-10-KIX(L664C) resulted in an estimated maximum particle dimension D_{max} of 64.2 Å. (D) The SAXS experimental profile of 1-10-KIX(L664C) (black) compared with the theoretical scattering profiles obtained from the 1-10-KIX(L664C) crystal structure (PDB ID: 4I9O) using FoXS (grey) or CRYSOL (green) resulted in suboptimal fitting (χ^2 = 4.73, CRYSOL; χ^2 = 9.24, FoXS). (E) N- and C-terminal residues (G586, V587, E666-L672) missing in the 1-10-KIX(L664C) crystal structure were modeled with MODELLER. The theoretical scattering profiles calculated from the modeled 1-10-KIX structure resulted in a much better fit to the experimental SAXS data (χ^2 = 1.51, CRYSOL (green); χ^2 = 1.49, FoXS (grey)). Likewise, the NMR structure of the KIX domain (from PDB ID: 2LXS, eliminating the MLL1 peptide) resulted in a very good fit (χ^2 = 1.57 after CRYSOL; χ^2 = 1.21 after further improvement with SREFLEX (orange)). (F) The modeled 1-10-KIX structure was overlaid onto the crystal structure (PDB ID: 4I9O). The modelled regions that were not visible in the crystal structure are indicated with the black arrows. Adopted from (Garg et al., 2019).

BMAL1:KIX complexes

The SAXS analyses was performed for three BMAL1:KIX complexes, viz. BMAL530:KIX, BMAL517:KIX and BMAL490:KIX. The Kratky plots suggested the BMAL1:KIX complexes to be partially unfolded and elongated in shape (Figure 3.32A). The partial folding of the BMAL1:KIX complexes is attributed to the contributions of both the unstructured BMAL1 fragments and the helically folded KIX domain which is consistent with the CD spectra (section 3.3.5). The estimated molecular weights and MW credibility intervals of the BMAL1:KIX complexes calculated using a Bayesian approach are 19.93 kDa and 18.35 kDa-21.50 kDa (BMAL530:KIX); 21.18 kDa and 19.0 kDa-23.35 kDa (BMAL517:KIX) and 33.10 kDa and 29.25 kDa-38.10 kDa (BMAL490:KIX) (Table 3.7). The estimated MWs are consistent with a 1:1 stoichiometry of the BMAL1:KIX complexes (refer to Table 3.7 for theoretical MWs) as also analyzed by SLS measurement of the BMAL530:KIX complex (section 3.3.6). From the distance distribution curves, the maximum particle dimensions (D_{max}) were calculated to be 115 Å, 137 Å and 175 Å for the BMAL530:KIX, BMAL517:KIX and BMAL490:KIX complexes, respectively (Figure 3.32C). The D_{max} and the elongated shapes of the complexes are attributed to the BMAL1 proteins, which remain largely unstructured in the complexes as suggested by the CD (section 3.3.5) and SAXS data and extend beyond the more compact KIX domain.

Furthermore, the low-resolution models were calculated for the BMAL530:KIX complex by two programs- DAMMIF/N and GASBOR using the output file generated from GNOM. The models calculated from both methods reasonably fit the experimental data (Table 3.7 and Figures 3.32D and 3.32G). By overlaying the DAMMIF/N-calculated envelopes of BMAL530 and KIX onto the envelope calculated for the BMAL530:KIX complex (Figure 3.33A), the KIX domain is positioned in a bulkier region in the bottom part of the BMAL530:KIX complex envelope and the additional, more elongated density emerging on the top is attributed to BMAL1 regions not directly interacting with the KIX domain.

For further investigation of the BMAL1 region extending out of the BMAL1:KIX core complex, the SAXS models for BMAL517:KIX and BMAL490:KIX complexes were calculated using DAMMIF/N and GASBOR, which reasonably fit to the experimental SAXS data (Table 3.7 and

Figures 3.32E-F and 3.32H-I). The BMAL1:KIX complexes with the longer BMAL1 constructs were indeed found to be more elongated in shape, as analyzed by comparing the SAXS models of the BMAL530:KIX, BMAL517:KIX and BMAL490:KIX complexes (Figure 3.33B) and depict a bulkier region in their bottom part that can be reasonably fit by the KIX domain envelope (Figures 3.33D-F). Furthermore, an overlay of the bulkier KIX domain regions resulting from the optimal superposition of the SAXS envelopes of BMAL530:KIX-, BMAL517:KIX- and BMAL490:KIX complexes highlights the elongated extensions on one side of the bulkier region in all three complexes that are significantly longer in BMAL490:KIX complex than in the BMAL530:KIX complex.

The narrow-shaped extensions are assigned to the BMAL1 regions N-terminal to the TAD that do not interact with KIX, based on the known information on interaction of KIX domain with the C-terminal BMAL1-TAD residues (Xu et al., 2015). The presented models identified the location and orientation of the N-terminal ends of the three BMAL1 constructs emerging from the BMAL1-TAD:CBP-KIX core complex that includes the C-terminal BMAL1 residues.

To further unravel the side of the KIX domain from where the N-terminal parts of BMAL1 emerge from the KIX:BMAL1-TAD core complex, the high-resolution 3D-structures of KIX domain (PDB: 4I9O and 2LXS, eliminating the MLL1-peptide) were positioned in the SAXS envelope of 1-10 tethered KIX (Figure 3.33C). The fitting of the 1-10-KIX crystal structure (PDB:4I9O) and the NMR structure of KIX (2LXS, model after SREFLEX) to the SAXS envelope of 1-10 tethered KIX and its further superposition onto the SAXS envelope of the BMAL530:KIX complex suggested that the N-terminal BMAL1 region emerges from the KIX domain near the MLL-binding site (Figure 3.33C). Combining the findings in this study with the published literature on BMAL1-KIX interactions (Xu et al., 2015), suggested that the N-terminal BMAL1 region preceding the BMAL1-TAD, that includes K537 and parts of the BMAL1 G-region, extends out from the BMAL1-TAD:CBP-KIX core complex near the MLL-binding site with the KIX-binding C-terminal BMAL1-TAD region docked in.

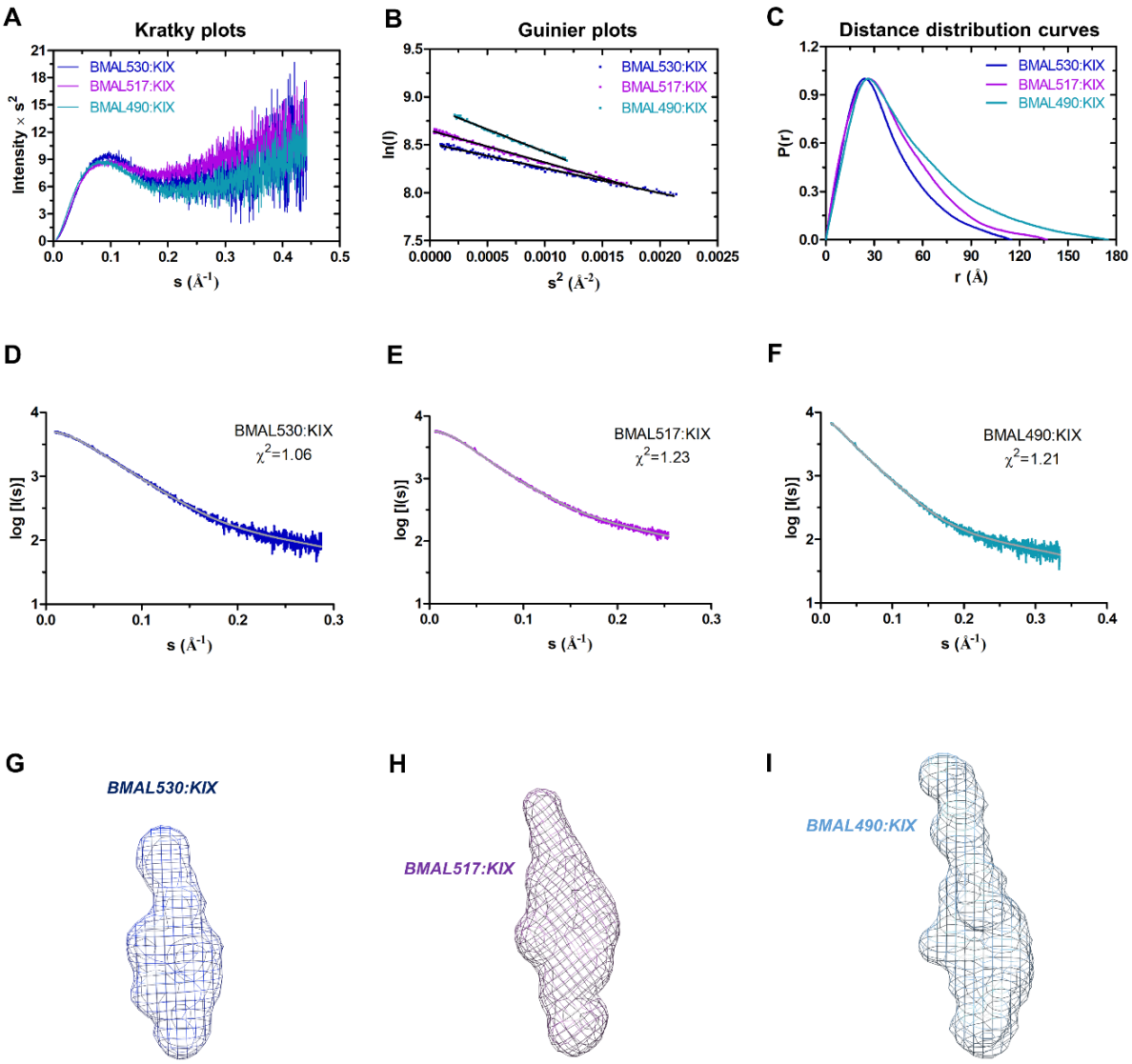

Figure 3.32 SAXS analyses of BMAL1:KIX complexes. (A) The Kratky plots for BMAL530(P624A):KIX(L664C) complex [termed as BMAL530:KIX] (blue), BMAL517:KIX complex (violet) and the BMAL490:KIX complex (cyan). All three complexes are partially unfolded and elongated in shape. (B) The Guinier plots of the complexes showed no aggregation as indicated by the linear dependence of ln(I) vs s^2; coloring as in panel A. (C) Distance distribution functions P(r) derived from the experimental SAXS data result in maximum particle dimensions (D_{max}) of 114.5 Å, 137 Å and 175 Å for the BMAL530:KIX, BMAL517:KIX and BMAL490:KIX complex, respectively; coloring as in panel A. (D-F) The best fits of the SAXS models (DAMMIF/N) of the BMAL530:KIX, BMAL517:KIX and BMAL490:KIX complexes calculated using DAMMIF/N (grey) to the experimental scattering data of the BMAL530:KIX complex (blue) (D), BMAL517:KIX complex (violet) (E) and the BMAL490:KIX complex (cyan) (F). The chi square (χ^2) values close to 1 reflect a good fit. (G-I) The *ab initio* SAXS models calculated from DAMMIF/N for BMAL530:KIX complex (G) BMAL517:KIX complex (H) and BMAL490:KIX complex (I). The maps were generated from the SAXS envelopes by Chimera (Pettersen et al., 2004). Adapted from (Garg et al., 2019).

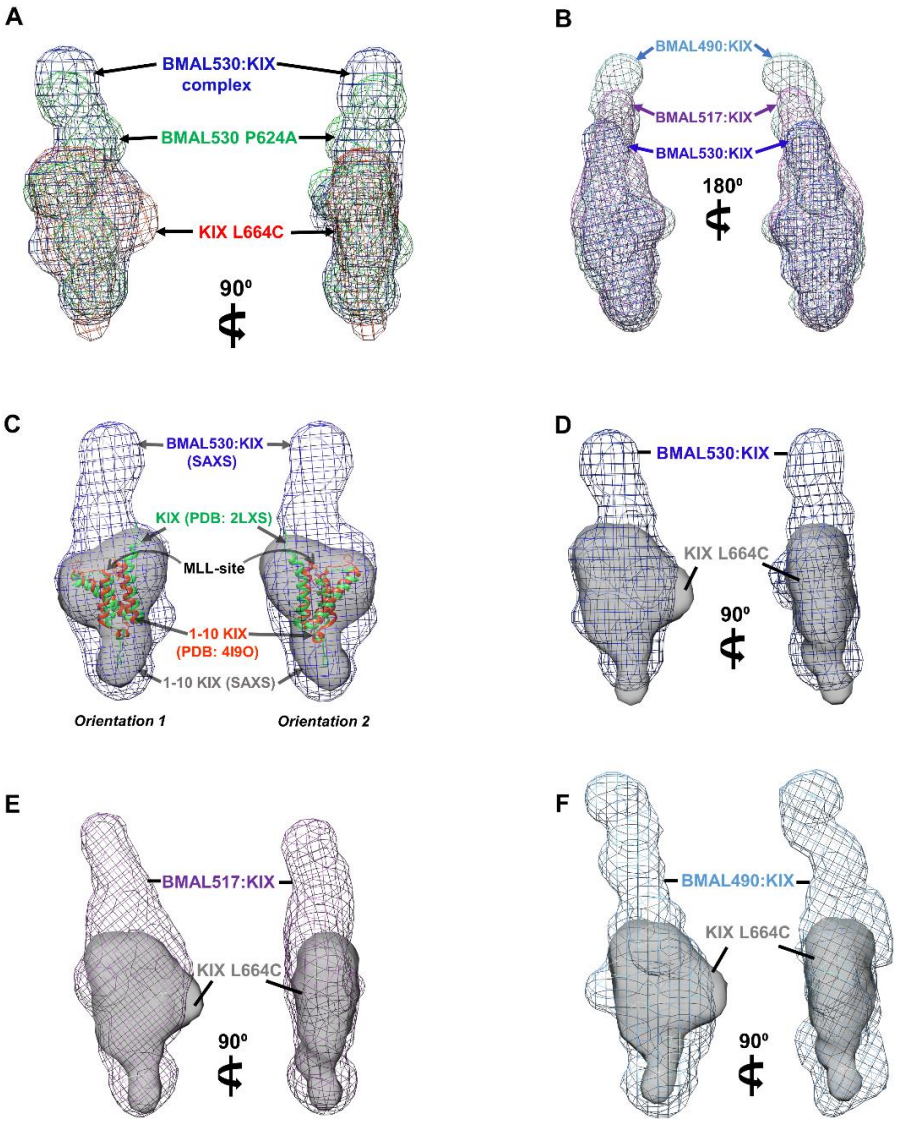

Figure 3.33 Comparison of SAXS envelopes of BMAL1:KIX complexes. (A) The overlay of mesh models of BMAL530(P624A) (green) and KIX(L664C) (red) onto the calculated model of BMAL530:KIX complex (mesh/blue) positions the KIX domain in the bulkier bottom part of complex envelope. (B) Superposition of the DAMMIF/N models (mesh) of BMAL530:KIX complex (blue), BMAL517:KIX complex (violet) and BMAL490:KIX complex (cyan) resulted in an overlay of the bulkier lower parts that accommodate the KIX domain and the KIX binding C-terminal BMAL1-TAD regions. The gradual elongation at the top of the complex envelopes are consistent with increasing N-terminal extensions of BMAL517 and BMAL490 preceding the BMAL1-TAD. (C) The 1-10-KIX(L664C) crystal structure (red, PDB: 4I9O) and the NMR structure of KIX domain (green, PDB: 2LXS after SREFLEX) were fitted into the SAXS envelope of 1-10-KIX(L664C) whose further fitting into the BMAL530:KIX complex envelope depicts the N-terminal BMAL1 extensions including parts of the G-region emerging from BMAL1-TAD:KIX core complex near the MLL-site of KIX (two orientations with KIX rotated by 180°). (D-F) The fitting of the KIX(L664C) SAXS envelope (grey/surface) into SAXS models of the BMAL530:KIX complex (blue/mesh) (D), BMAL517:KIX complex (violet/mesh) (E), and BMAL490:KIX complex (cyan/mesh) (F) further highlights the positioning of KIX domain in the bottom bulkier part of the complexes. The fitting and superpositions were performed using Chimera (Pettersen et al., 2004). Adapted from (Garg et al., 2019).

Notably, the alternative orientations of the KIX domain within the bulkier regions of the complex envelopes cannot be entirely excluded based on the low-resolution SAXS envelopes. However, the fitting of alternative KIX orientations within the bulkier regions of the complex envelopes was suboptimal compared to the presented orientation (Figures 3.33D-F) and resulted in the additional extensions emerging from the KIX:BMAL1-TAD core complex on the opposite side of the N-terminal BMAL1 regions. The fact that the most C-terminal BMAL1 residues are engaged in the KIX binding (Xu et al., 2015), makes the fitting of alternative KIX orientation less consistent.

3.4 Purification of BMAL1:CRY1 complexes and crystallization attempts

3.4.1 Purification of BMAL1:CRY1 complex

The C-terminus of BMAL1 along with the TAD region interacts with both negative and positive transcriptional regulators (Czarna et al., 2011, 2013; Kiyohara et al., 2006; Park et al., 2015; Takahata et al., 2000; Xu et al., 2015). The K537 acetylation in BMAL1 enhances the CRY1-mediated transcriptional repression and the affinity of CRY1 for BMAL1 (Czarna et al., 2011; Hirayama et al., 2007). In this study, the lysine-acetylation-mimetic K537Q mutant of BMAL1 is used for the purification of complex with CRY1. In the starting of this study, the purification trials of the BMAL1:CRY1 complex were made using GST-tagged mouse BMAL1-(490-625)K537Q [termed as BMAL490(K537Q)] and N-terminally-His_6-tagged full-length (FL) mouse CRY1. The similar problems of stickiness of GST were encountered while purifying the BMAL1:CRY1 complex as in the case of purification of BMAL490:KIX complex (section 3.2.1). To tackle the problem of stickiness and to optimize the purity of the complex for crystallization, the BMAL490(K537Q) was re-cloned in pCoofy1 vector as the His_6-fusion and the expression and solubility tests were performed in *E. coli* Rosetta DE3 at 18°C in TB medium. The protein was well expressed and soluble in the tested conditions. The full-length mouse CRY1 was expressed using Bac-to-Bac baculovirus expression system (Life Technologies) and the required amount of virus was optimized for optimal expression (see Materials and methods). The complex was purified using

Ni^{+2}-affinity and anion-exchange chromatography (AEX) as described in section 2.2.4. The final purification using Superdex 200 16/60 size-exclusion column yielded two main peaks of CRY1:BMAL490(K537Q) complex and excess BMAL490(K537Q) at 66 ml and 81 ml, respectively (Figure 3.34). The purified CRY1:BMAL490(K537Q) complex protein was setup for crystallization trials at 4°C and 20°C at a concentration of 9 mg/ml. No crystallization hits were obtained in the tested conditions.

To improve the purity of the complex, another purification trial was made with a change during the anion-exchange step. The protein was eluted along a flatter NaCl gradient to improve the resolution of the non-specific impurities and the complex. This step could not improve the purity of the protein and further the final purification was performed using size-exclusion chromatography by Superdex 200 16/60 column (data not shown).

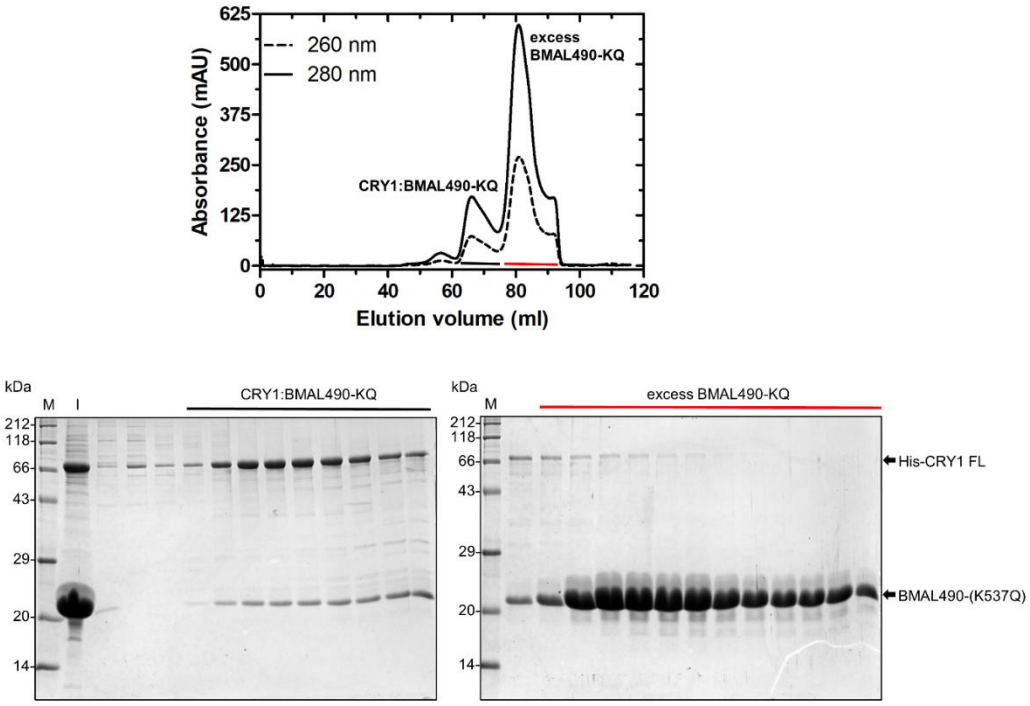

Figure 3.34 The purification of the complex of BMAL1-(490-625)K537Q with full-length (FL) mCRY1. The purification was performed with full-length mCRY1 and BMAL490(K537Q), both as the His_6-fusion proteins using Ni^{+2}-affinity, anion-exchange and size-exclusion chromatography as the final step. The size-exclusion chromatogram using Superdex 200 16/60 showed the peaks of complex elution at ~ 66 ml and elution of excess BMAL490(K537Q) at ~ 81 ml. The eluted fractions, marked by black (for complex) and red lines (for excess BMAL490(K537Q)), are analyzed by SDS-PAGE (lower panel). The fractions corresponding to the complex were concentrated and setup for crystallization trials. M=Protein Marker; I=input protein injected on the size-exclusion column.

3.4.2 Reconstitution of the BMAL1:CRY1-(1-496) complex

C-His$_6$-CRY496:BMAL530-K537Q

The interactions of C-terminal residues of BMAL1 with mammalian Cryptochrome are mediated by the C-terminal coiled-coil helix (CC) of the photolyase homology region (PHR) and the C-terminal tail (Czarna et al., 2011, 2013). However, it has been reported recently that the truncation of the C-terminal tail of mCRY1 does not affect the binding with BMAL1 and the CRY1-(1-496) [CRY496], which includes the PHR, binds equally well with a short BMAL1-TAD peptide (aa 593-625, K_D ~ 1 μM) (Gustafson et al., 2017). For the purpose of crystallization of the BMAL1:CRY1 complex, the crystallizable region of mCRY1 (CRY496) (Figure 3.35A) with C-terminally-fused His_6-tag was used to reconstitute its complex with His_6-BMAL530(K537Q) protein. Initial trials of the complex formation were made with the individually purified His_6-BMAL530(K537Q) and C-His_6-CRY496. The size-exclusion using Superdex 200 10/300 resulted in two overlapping peaks with one mainly eluted CRY496 alone and other mainly BMAL1 (Figure 3.35B). As the peaks were overlapping, it could not be clear from the SDS-PAGE as well whether a complex was formed.

The second trial of purification of the CRY496:BMAL530(537Q) complex was performed by lysis of the cells individually expressing CRY496 and BMAL530(K537Q) protein and the co-purification. The final purification by SEC using Superdex 200 16/60 column yielded a peak at 72 ml and two overlapping peaks (Figure 3.35C) which were analyzed by SDS-PAGE. Analysis by SDS-PAGE showed that the eluted peak at 72 ml mainly contains CRY496 with the faint bands of BMAL530(K537Q), suggesting that a strong CRY496:BMAL530(K537Q) complex could not be formed. The interference of the His_6-tag at the C-terminus of CRY496 could not be excluded in formation of the complex based on importance of the CC-helix in mediating the interaction with BMAL1. Therefore, reconstitution of the CRY496:BMAL1 complex was further tried using CRY496 with N-terminally fused His_6-tag.

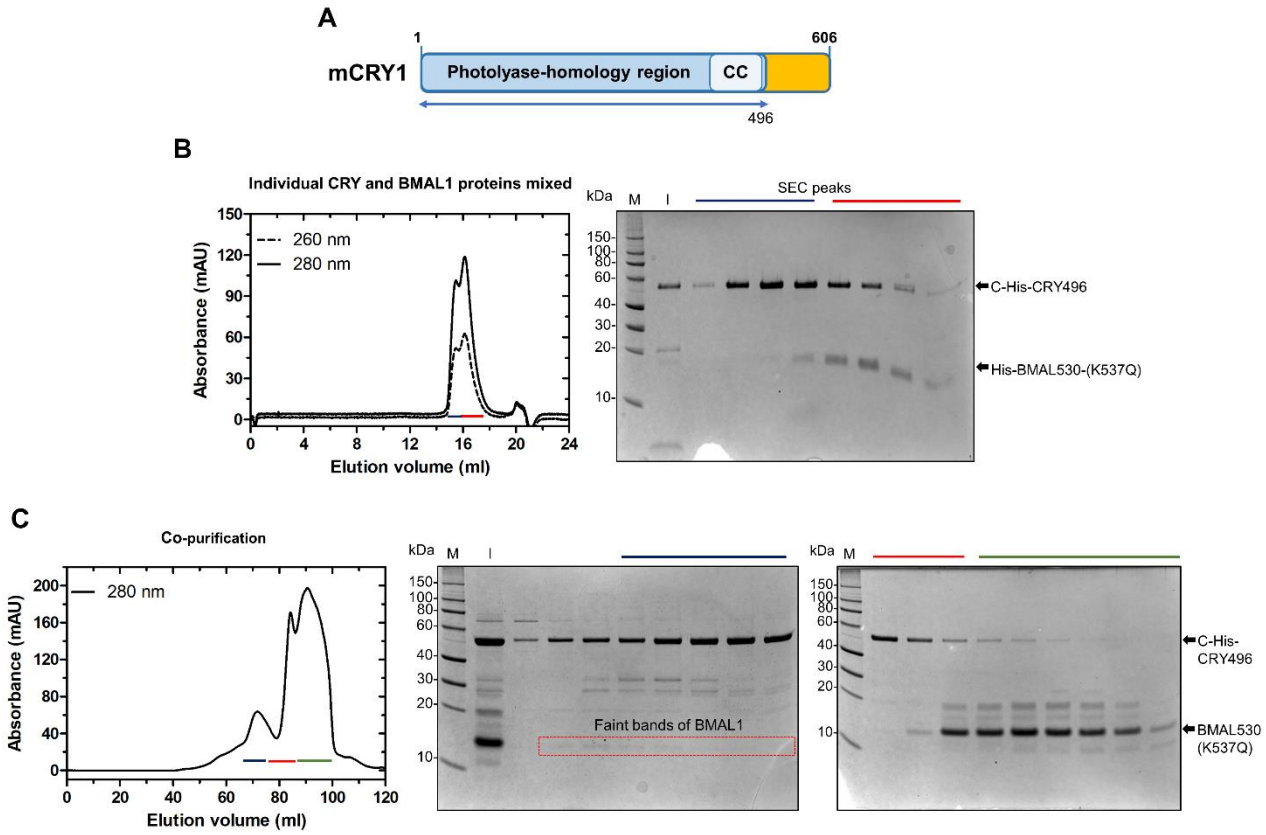

Figure 3.35 Reconstitution of the mouse CRY496:BMAL530(K537Q) complex. (A) Domain architecture of mouse CRY1 showing photolyase-homology region with the coiled-coil (CC) helix and the C-terminal tail. The arrow indicates the crystallizable construct of mCRY1 (aa 1-496) used in this section for complex formation with BMAL1. (B) The pre-purified individual C-His_6-CRY496 and His_6-BMAL530(K537Q) proteins were incubated together and loaded on the size-exclusion Superdex 200 10/300 column. The size-exclusion chromatogram showed two overlapping peaks with one eluted mainly CRY496 and other BMAL530(K537Q) as shown by SDS-PAGE analysis. The peak fractions analyzed by SDS-PAGE are marked with blue and red lines. (C) The reconstitution of the CRY1:BMAL1 complex was performed again by co-purification. The cells individually expressing C-His_6-CRY496 and His_6-BMAL530(K537Q) proteins were lysed and co-purified by Ni^{+2}-affinity chromatography followed by anion-exchange and size-exclusion chromatography. The size-exclusion chromatogram using Superdex 200 16/60 column showed the elution of three peaks. The peak fractions marked by blue, red and green lines were analyzed by SDS-PAGE and showed that the peak eluted at 72 ml mainly consists of CRY496 with the faint bands of BMAL530(K537Q). M=protein marker, I=input protein injected on SEC column.

N-His_6-CRY496:BMAL530 K537Q

To further test the possibility of C-terminally-fused His_6-tag interfering in the formation of CRY496:BMAL530(K537Q) complex, the CRY496 was expressed as N-terminal His_6-fusion protein

in insect cells. The expression was tested with varying amounts of virus and incubation time (Figure 3.36) (see Materials and methods).

The purification was performed with Ni^{+2}-affinity chromatography followed by anion-exchange and size-exclusion chromatography. The size-exclusion chromatogram using Superdex 200 16/60 column resulted in two distinct peaks mainly of CRY496 at 76 ml and BMAL530(K537Q) at 85 ml (Figure 3.37). Similar to the purification trial of the BMAL1:CRY1 complex with C-His_6-CRY496 (Figure 3.35C), the faint bands of BMAL530(K537Q) were observed from SDS-PAGE analysis of the peak at 76 ml along with CRY496. These results suggest that in our experimental conditions, a strong CRY496:BMAL530(K537Q) complex cannot be formed, which may possibly due to the truncation of the C-terminal tail of CRY1. The disordered C-terminal tail region of CRY1 along with the CC-helix have been reported to contain the BMAL1-binding epitopes (Czarna et al., 2011) and both regions may be equally important for reconstitution of the CRY1:BMAL1 complex in SEC. Additionally, in this thesis, a longer BMAL1 construct (aa 530-625) with N-terminal extension preceding the TAD has been used compared to the short BMAL1-TAD (aa 593-625) used by Gustafson et al. (Gustafson et al., 2017) which may also contribute in lowering the CRY1-binding affinity.

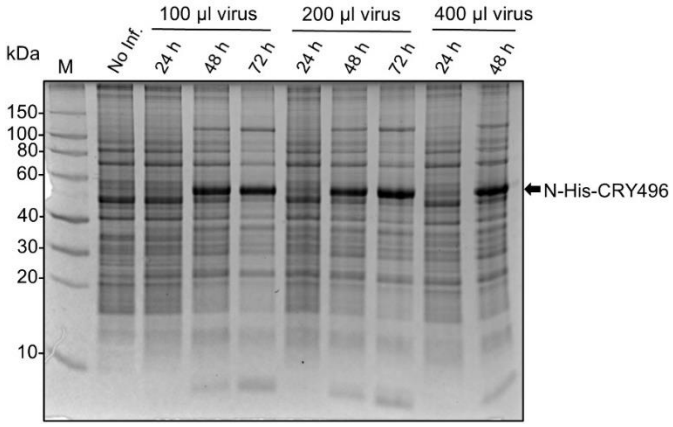

Figure 3.36 Expression of N-terminally His_6-tagged mouse CRY496 protein. The 50 ml High Five insect cells with a density of $0.5x10^6$ cells/ml were infected with varying amounts of P2 virus (100 µl, 200 µl and 400 µl) and the samples were collected after 24 h, 48 h and 72 h. All the collected samples including control (non-infected cells) were analyzed by 10% Bis-Tris gels. Arrow indicates the expressed N-His_6-CRY496 protein. M=protein marker, No Inf.=no infection.

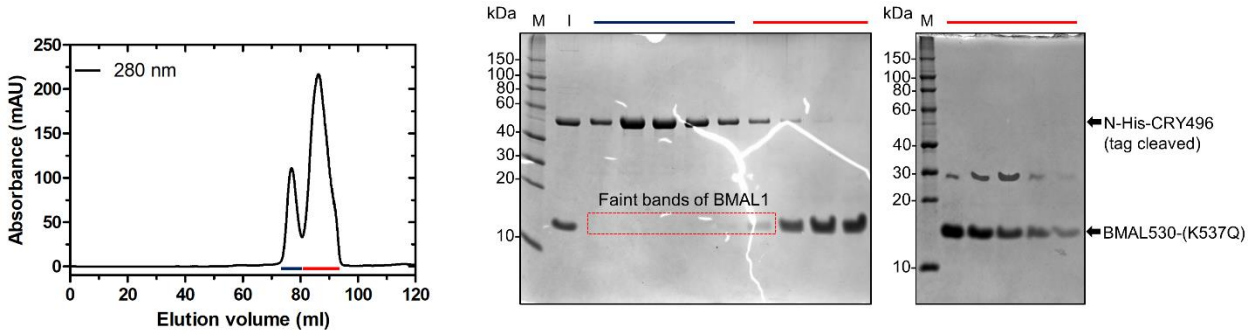

Figure 3.37 The reconstitution of the CRY1:BMAL1 complex performed using N-terminally His_6-tagged CRY496. The cells individually expressing N-His_6-CRY496 (see Figure 3.36) and His_6-BMAL530(K537Q) proteins were lysed and co-purified by Ni^{+2}-affinity chromatography followed by anion-exchange and size-exclusion chromatography. The size-exclusion chromatogram using Superdex 200 16/60 column showed the elution of two peaks at 76 ml and 85 ml observed by UV absorbance at 280 nm. The peak fractions marked by blue and red lines were analyzed by SDS-PAGE and showed that the peak eluted at 76 ml mainly consists of CRY496 with the faint bands of BMAL530(K537Q) similar to the purification with C-His_6-CRY496 (Figure 3.35C) indicating that a strong complex between CRY496 and BMAL530(K537Q) cannot be reconstituted. M=protein marker, I=input protein injected on SEC column.

3.5 Incorporation of Lys-537 acetylation in BMAL1 using tRNA-synthetase/amber-suppressor pair

The Lys-537 acetylation in BMAL1 enhances its affinity for CRY1 and the transcriptional repression (Czarna et al., 2011; Hirayama et al., 2007). The *in vitro* biochemical studies were performed with the $K537Q_{mBMAL1}$ mutant mimicking the Lys-537 acetylation (Czarna et al., 2011). Here, in this study, we aim to incorporate K537-specific acetylation using a tRNA-synthetase/amber-suppressor pair (section 2.2.1) (Neumann et al., 2008, 2009).

The codon encoding for K537 was mutated to Amber codon and the initial acetylation-incorporation trials were performed by co-transformation of the $Amber_{BMAL490}$ mutant (cloned in modified pCoofy1 with ampicillin resistance), pCDF-pylT vector (Strep/$Spec^R$) and AcKRS-3 gene (Kan^R) (encodes for acetyl-lysyl-tRNA synthetase) in *E. coli* BL21 DE3 strain. The expression was performed in 1 L TB media supplemented with 2 mM acetyl lysine and 20 mM nicotinamide. The nicotinamide acts as the inhibitor of deacetylation activity of sirtuins (Avalos et al., 2005).

The lysis of the cells was carried out in the lysis buffer supplemented with 20 mM nicotinamide (see Materials and methods for the composition of lysis buffer). The purification was performed by Ni^{+2}-affinity and size-exclusion chromatography. The precipitation was observed before the protein was concentrated to load on the size-exclusion column. The size-exclusion chromatogram using Superdex 75 16/60 column yielded three peaks as observed by UV-absorbance at 280 nm, which were analyzed by SDS-PAGE (data not shown). One peak eluted close to the void volume contained mostly chaperones (MW ~ 66 kDa) and a protein of ~ 14 kDa (theoretical MW of His_6-BMAL490 ~ 14 kDa). Other peak eluted at ~ 58 ml was analyzed to contain a protein of MW ~ 25 kDa. As His_6-BMAL490 runs aberrantly in SDS-PAGE at >20 kDa (section 3.2.1), the identity of the ~ 14 kDa protein and ~ 25 kDa protein were confirmed by mass spectrometry and found to be *E. coli* RNA-binding protein and cAMP-activated transcription regulator protein. The RNA-binding protein is an RNA-chaperone and functions during the cellular stress. This indicated that the cells were under stress in the used experimental conditions.

Before the mass spectrometry analysis, the proteins eluted from the peak at ~ 58 ml in SEC and the Ni^{+2}-affinity column were also analyzed by Western blot using anti-penta His antibody. The Western blot detection showed the double band in the protein eluted from SEC (data not shown) which we attribute to the His_6-3C protease used to cleave the His_6-tag after Ni^{+2}-affinity chromatography.

Next trial of incorporating the acetyl lysine was performed by expressing the protein in *E. coli* Rosetta DE3 competent cells and in LB medium and the nicotinamide was omitted from the lysis buffer as it seemed to be interfering with binding of the protein on Ni^{+2}-affinity column. The purification was performed using Ni^{+2}-affinity and size-exclusion chromatography. The size-exclusion chromatogram from Superdex 75 10/300 column resulted in two peaks at ~ 9 ml and ~ 11 ml which were analyzed by SDS-PAGE (data not shown). The proteins (at ~ 17 kDa and ~ 26 kDa) were further analyzed by mass spectrometry and identified to be *E. coli* FKBP-type peptidyl-prolyl isomerase and Ferric uptake regulator protein, respectively.

Based on the published protocol of incorporating the Lys-acetylation (Neumann et al., 2008, 2009), the $Amber_{BMAL490}$ mutant gene was re-cloned in pCDF vector carrying the pylT gene which

encodes for $tRNA_{CUA}$ amber suppressor. The cloned plasmid was co-transformed in Rosetta DE3 with AcKRS-3 gene and expressed in the presence of 2 mM acetyl-lysine and 20 mM nicotinamide. The final purification by size-exclusion chromatography using Superdex 75 10/300 column yielded the peaks similar to the previous purification trial which were analyzed by SDS-PAGE (data not shown). The protein (~ 17 kDa) eluted in the peak at ~ 11 ml was previously analyzed to be Ferric uptake regulator protein by mass spectrometry. Another protein at ~ 23 kDa was analyzed to be FKBP-type peptidyl-prolyl isomerase. The identification of only *E. coli* contaminant proteins indicates that no Lys-537 acetylated BMAL490 was expressed. Further expression trials may be performed by varying the supplemented concentration of the acetyl lysine during protein induction.

4. Discussion

In the mammalian circadian clock, the C-terminal transactivation domain (TAD) of BMAL1 and the preceding BMAL1 G-region (E429-I578) including the acetylated K537 (Figure 1.4A, 1.5) possess the critical functional importance (Bunger et al., 2000; Hirayama et al., 2007; Kiyohara et al., 2006; Park et al., 2015; Takahata et al., 2000; Xu et al., 2015). The transcriptional repression or activation of CLOCK:BMAL1 is facilitated by the BMAL1-TAD via its interaction with CRY or the CBP/p300 KIX domain, respectively (Czarna et al., 2011, 2013; Kiyohara et al., 2006; Park et al., 2015; Takahata et al., 2000; Xu et al., 2015). On the other hand, the CBP-KIX interacts with several transcriptional regulators through its two binding pockets (Thakur et al., 2014).

In this thesis, biochemical, biophysical and structural insights into the mechanisms of the BMAL1-KIX interaction have been provided. The affinity measurements of the BMAL1 proteins with the KIX domain and the pull-down studies of the BMAL1:KIX complex with MLL1 facilitate to unravel the contributions of the MLL- and c-Myb-binding pockets of CBP-KIX in the interaction with BMAL1. Further, the contributions of the two CBP-KIX pockets, the effect of $Lys537_{BMAL1}$ acetylation and the binding-induced conformational transition studied in this thesis enhance the mechanistic understanding of the roles of the BMAL1-TAD-CBP-KIX interaction and its interplay with the other KIX-binding partners and with the BMAL1-CRY interaction in circadian gene regulation. The SAXS models of BMAL1-TAD:CBP-KIX complexes provided in this thesis show the first structural view into the architecture of the complex which further helps to determine the location of the N-terminal region of BMAL1 preceding the TAD with respect to the core BMAL1-TAD:CBP-KIX complex. Finally, the study in this thesis enhances the structural and mechanistic understanding of the CBP-dependent gene regulation in the mammalian circadian clock. In the following sections, the work performed in this thesis, the underlying importance and future prospects will be discussed in more details.

4.1 *In vitro* reconstitution of BMAL1:KIX complexes and crystallization

For crystallization of the BMAL1:KIX complex, it was necessary to define stable constructs of the C-terminal region of BMAL1 and of the CBP-KIX domain. As the complex of KIX with the previously described ~14 kDa C-terminal mouse BMAL1(490-625) fragment [termed BMAL490 in this thesis], which includes the C-terminal TAD, Lys-537 and parts of the G-region (Czarna et al., 2011) did not crystallize, new stable C-terminal BMAL1 constructs (in complex with the KIX domain) were defined in this thesis by limited proteolysis of the BMAL490:KIX complex (BMAL517) and by the further N-terminal truncation of a Proline-rich region (BMAL530). The KIX domain was found to be stable in the BMAL1 complex during proteolysis and signs of KIX degradation were seen only upon C-terminal degradation of BMAL1. Hence, the C-terminal region of BMAL1 protects the KIX domain in the complex, consistent with earlier reports that the KIX-binding sites reside in the C-terminal region of BMAL1 (Xu et al., 2015). This thesis reports the purification of complexes of KIX with two newly defined BMAL1 constructs (BMAL517 and BMAL530), that were stable during various sequential purification steps described in sections 3.2.3 and 3.2.4. However, both complexes could not be crystallized. The difficulties in crystallization might be due to the facts that the KIX domain is conformationally malleable (Wang et al., 2013a) and that the C-terminal region of BMAL1 is disordered (Czarna et al., 2011) and contains a conformational switch in the distal C-terminus that undergoes *cis-trans* isomerization (Gustafson et al., 2017). To improve the likelihood of BMAL1:KIX complex crystallization, the BMAL1-TAD was locked in *trans* conformation by introducing the P624A mutation and KIX was tethered with the small compound 1-10 in the MLL-binding pocket, which stabilizes KIX and renders it suitable for crystallization (Wang et al., 2013a). The BMAL1 proteins are prone to degradation when purified alone (this study) and the stability is enhanced upon introducing the P624A mutation which might be due to inability of the P624A mutant to undergo *cis-trans* isomerization.

Herein, we also performed co-crystallization of 1-10-KIX with a 21-mer C-terminal BMAL1 peptide, which includes the IxxLL$_{606}$ motif within the predicted α-helix important for KIX-binding (Xu et al., 2015). A 1.4 Å KIX-1-10 crystal structure, that we solved from these crystal setups, revealed no density for the BMAL1 peptide, but showed a significant displacement of a loop region located nearby the MLL pocket between the α1 and α2 helices of the KIX domain. In light

of the importance of the MLL-pocket for BMAL1 binding (this study), the movement of the loop nearby the MLL1 pocket may be significant and be correlated with the presence of the peptide in the setups. However, this loop region is also involved in crystal contacts, which may prevent a complete loop reorientation and peptide binding (loop movement occurs within crystal packing constraints). Alternative loop conformation is also stabilized by a sulfate ion. Further mutational and *in vivo* studies could hint at the role and the biological function of the loop region in BMAL1-CBP interactions. In addition, further crystallization trials with a BMAL1 peptide including the last seven C-terminal residues could be performed keeping in mind the importance of this region (Czarna et al., 2011; Kiyohara et al., 2006; Xu et al., 2015). Besides that, as we found that both KIX pockets play a role in BMAL1-binding (this study), it could be possible that the two KIX-binding regions of BMAL1 (predicted helix and C-terminal residues) could bind near both KIX pockets.

Further, the SEC analysis showed that the C-terminal BMAL1 proteins alone as well as in complex with KIX domain elutes at an advanced volume and indicated the higher experimental molecular weight as compared to the theoretical molecular weight calculated from the amino acid sequence. Also, purified C-terminal BMAL1 proteins run at an aberrant molecular weight in SDS-PAGE consistent with the previous study (Czarna et al., 2011). This discrepancy is might be due to the elongated shape of C-terminally disordered region of BMAL1, as SEC is a hydrodynamic technique that separates the molecules according to their shape and size and elongated proteins can elute at the volumes corresponding to the higher molecular weight as compared to the globular protein of same molecular weight (Erickson, 2009; La Verde et al., 2017). SAXS analysis further confirmed the elongated shape of BMAL1 proteins. The SLS analysis and the estimated molecular weights calculated using Bayesian inference approach (Hajizadeh et al., 2018) from the SAXS measurements performed in this study showed the BMAL1 proteins to be monomeric and further demonstrated a 1:1 stoichiometry of BMAL1:KIX complexes.

4.2 Role of the MLL- and pKID/c-Myb binding pockets in BMAL1-KIX interaction

Primarily, the quantitative interaction studies were performed in this thesis to unravel the role of MLL- and pKID/c-Myb-binding pockets of the KIX domain in BMAL1-KIX interactions. The

affinity measurements using MST, FP and nanoSPR revealed that the tethering of compound 1-10 to KIX(L664C) or KIX(N627C) in the MLL-binding pocket, which significantly weakens the affinity of the MLL1-TAD to KIX (Wang et al., 2013a), only moderately decreased the affinity of BMAL1 to KIX by about two-fold. The untethered KIX(L664C) mutation showed only a trend of reducing binding affinity for BMAL1 compared to a ~ 6-fold reduced affinity for MLL1-TAD (Wang et al., 2013a). In contrast, the untethered KIX(N627C) mutation on the opposite side of the MLL-binding pocket showed a trend of enhancing BMAL1 binding. Altogether, these observations suggested that the MLL-binding pocket is involved in BMAL1 interactions, but with a different binding mode of the BMAL1-TAD compared to the MLL1-TAD, possibly in closer proximity to N627. The diverse binding modes of different ligands in the MLL pocket have been described structurally and are enabled by the intriguing degree of plasticity of the MLL-binding pocket (Wang et al., 2012).

In the MST and FP experiments performed in this study, overall lower KIX binding affinities of BMAL530 were observed unexpectedly, compared to the nanoSPR experiments described here and the published data (Gustafson et al., 2017). These observations have been attributed to the fluorescently-labeled N-terminal His_6-tag fused to BMAL530 suggesting that the modifications of the BMAL1 region N-terminal to the TAD could have an impact on the BMAL1-TAD-KIX interaction which may be correlated with the reported functional importance of the BMAL1 G-region (Xu et al., 2015).

Further, the pull-down experiments of a 19mer MLL1-TAD fragment (MLL19) with the KIX:BMAL530 complex and with individual BMAL530 and KIX proteins were also performed in this study. Interestingly, MLL19 was only able to pull down KIX, but not BMAL1, when incubated with the individual BMAL530 and KIX proteins together. Furthermore, MLL19 displaced BMAL1 from the pre-purified KIX:BMAL530 complex. The binding site competition between MLL1 and BMAL1 observed in the pull-down experiments further supports the importance of the MLL-binding pocket of the KIX domain for BMAL1-TAD interactions. It remains to be examined how the acetylation of MLL1 on K1130 and K1333 by the CBP-HAT domain, which enhances MLL1-dependent H3K4 trimethylation and subsequent co-activation of CLOCK:BMAL1 dependent circadian genes *in vivo* (Aguilar-Arnal et al., 2015; Katada and Sassone-Corsi, 2010), would be

impacted by the binding site competition between the BMAL1-TAD and the MLL1-TAD for the CBP-KIX domain. It is conceivable that the further stabilization of the BMAL1-CBP interaction is required for the recruitment of CBP to the CLOCK:BMAL1 complex, e.g. via posttranslational modifications or additional CBP domains, for enhancing the specificity of CBP for BMAL1 over alternative KIX-binding transcription factors such as MLL1. The simultaneous recruitment of MLL1 and CBP to CLOCK:BMAL1 and the acetylation of MLL1 by CBP would then be attainable, as CBP is recruited via BMAL1 (Kiyohara et al., 2006; Park et al., 2015; Takahata et al., 2000; Xu et al., 2015) whereas MLL1 interacts with the exon19 region of CLOCK using a MLL1 binding site near K1130 and K1333 (Aguilar-Arnal et al., 2015; Katada and Sassone-Corsi, 2010).

In this work, we introduced the mutations Y658A and Y650A/A654W in the second pKID/c-Myb binding pocket of KIX domain to determine its role in BMAL1 binding, in addition to the MLL-pocket. These mutations are known to significantly weaken the interaction of KIX with c-Myb or pKID (Parker et al., 1999) but interestingly, in the nanoSPR experiments presented in this study, BMAL1 binding to KIX is only moderately impacted by these mutations with a ~2 to 2.5-fold weakened affinity for the Y650A/A654W double mutant and an even less pronounced effect of the Y658A mutant. Interestingly, the binding affinity analysis using the Hill equation suggested the BMAL1-KIX interaction to be positively cooperative and the cooperativity is lost upon tethering with compound 1-10 in the MLL-pocket or by the double mutation (Y650A/A654W) in the c-Myb/pKID-pocket, further suggesting the role of both binding sites in interaction. As previously described (section 1.3.3), the alterations in both KIX binding pockets only moderately impacted binding of FOXO3a, suggesting that the interaction of KIX domain with BMAL1 is reminiscent of FOXO3a binding and like FOXO3a or p53 (Lee et al., 2009; Wang et al., 2012), BMAL1-TAD may interact with both KIX binding sites, but using different binding modes than MLL1, CREB-pKID or c-Myb. As detailed in section 1.3.3, FOXO3a interacts simultaneously to both binding sites of KIX with its conserved regions 2 and 3 (CR2C and CR3) orienting themselves in different conformations and orientations which deviate from that of the MLL1-TAD or pKID peptides (Wang et al., 2012). In the case of the p53-TAD, synergistic binding of its two subdomains AD1 and AD2 to both KIX binding sites (Lee et al., 2009) has been documented. The BMAL1-TAD also contains a ϕxxϕϕ motif ($IxxLL_{606}$, ϕ = hydrophobic residue) like CR2C and CR3

of FOXO3a, subdomains AD1 and AD2 of the p53-TAD, and other transactivation domains of KIX binding partners, which could potentially interact with either of the two KIX binding sites. Moreover, the IxxLL$_{606}$ motif of BMAL1 was shown to be much more important for KIX binding than the seven most C-terminal BMAL1 residues, as the deletion of the C-terminal BMAL1 residues only led to a two-fold reduced affinity whereas the L605A/L606A double mutation completely disrupted the BMAL1-KIX interaction (Xu et al., 2015). Based on our results, we presently favor a scenario in which the more important BMAL1 interaction site is located near the MLL-binding pocket as in the pull-down experiments presented in this work, the MLL19-TAD peptide completely displaced BMAL1 from the BMAL1:KIX complex.

4.3 Inability of BMAL1-TAD to undergo binding-induced folding

The intrinsically disordered regions within the TADs of KIX-binding partners typically attain folding upon complexation with the KIX domain (Gianni et al., 2012; De Guzman et al., 2006; Parker et al., 1999; Radhakrishnan et al., 1997; Thakur et al., 2014; Zor et al., 2002). Upon binding to CRY1 and KIX, the BMAL1-TAD also undergoes conformational rearrangements as suggested by manganese-dependent paramagnetic relaxation enhancement studies (Xu et al., 2015). These studies prompted us to further biophysically characterize the formation of the BMAL1-TAD:KIX complex by CD spectroscopy to monitor the binding-induced changes in the secondary structure. The CD and SAXS analyses performed herein showed that the BMAL1-TAD and the preceding N-terminal regions are intrinsically disordered, consistent with the previous studies (Czarna et al., 2011; Xu et al., 2015) allowing the BMAL1-TAD to dynamically interact with co-regulators in the mammalian circadian clock. Contrary to the induced folding of the c-Myb-TAD and CREB-pKID upon binding to KIX (Gianni et al., 2012; Radhakrishnan et al., 1997), interestingly, our CD spectra showed that the BMAL1-TAD interaction with the KIX domain does not lead to pronounced changes in secondary structure content compared to the averaged spectra of BMAL530 and KIX proteins. Hence, our CD data do not suggest any major folding events of extended unstructured BMAL1 regions upon complexation with KIX domain. However, conformational rearrangements associated with minor secondary structure changes, e.g. a locally enhanced helical folding of the

IxxLL$_{606}$ motif region at the KIX interface or orientation changes of the polypeptide chain cannot be excluded by our CD data and shall be further explored.

4.4 Docking of C-terminal BMAL1 region into the core BMAL1-TAD/CBP-KIX complex

The structural studies on BMAL1-TAD alone and the BMAL1-KIX complexes using SAXS measurements presented in this thesis provided the first insights into their architecture. The SAXS analyses of the BMAL530 fragment, which includes the BMAL1-TAD and parts of the G-region, revealed it to be elongated, lacking a compact domain and mostly unfolded. Furthermore, the BMAL530:KIX complex has an extended shape with a D_{max} similar to the unbound BMAL530. These results together with the Kratky Plot analyses suggested that the BMAL1-TAD does not fold upon KIX binding, consistent with our CD spectra.

In this work, we have also performed SAXS measurements of complexes of the KIX domain with BMAL1 proteins of varying N-terminal length preceding the TAD in order to locate the N-terminal G-region including Lys537 within the BMAL1:KIX complex. The N-terminal parts of the BMAL1 fragments used herein (BMAL530, BMAL517 and BMAL490) extend out of the bulkier BMAL1-TAD:KIX core complex, as revealed from the comparison and superposition of the BMAL530:KIX complex with the complexes including longer BMAL1 fragments (BMAL517:KIX, BMAL490:KIX). On the basis of the fitting of high-resolution 3D structures and the SAXS envelope of the KIX domain into our SAXS models of the three BMAL1:KIX complexes as well as the KIX-BMAL1 interaction studies presented in this work and also reported previously (Xu et al., 2015), we propose that the C-terminal BMAL1-TAD region is bound to the KIX domain utilizing both binding sites, while the N-terminal part preceding the BMAL1-TAD, which includes parts of the G-region and Lys537, emerges from the KIX:BMAL1-TAD core complex near the MLL-binding pocket. This model interpretation is also consistent with our finding that the MLL1-TAD interferes with BMAL1-TAD:KIX complex formation. Our model provides a plausible starting point to further mechanistically probe BMAL1-CBP interactions, which requires to be expanded by elucidating the high-resolution structures to look closely into the structure of the complex.

4.5 Role of Lys537$_{BMAL1}$ acetylation in BMAL1-CBP interaction

The acetylation of BMAL1 at Lys537 enhances its binding to CRY1 and the transcriptional repression of CLOCK:BMAL1 *in vivo* (Hirayama et al., 2007). The *in vivo* effect of K537 acetylation is mirrored by the acetyl-lysine mimetic K537Q mutation in the purified BMAL1 protein by enhancing the CRY1 binding affinity to the BMAL1-TAD (Czarna et al., 2011, 2013). In this study, using NanoSPR and MST measurements, we found that the K537Q mutation does not affect the binding affinity of BMAL530 for KIX which contrasts with the enhancing effect of both the *in vitro* K537Q mutation and the *in vivo* K537 acetylation on CRY1 binding. Considering the mimicking of the effect of K537 acetylation by K537Q mutation, as reported for CRY1-BMAL1-TAD interactions (Czarna et al., 2011, 2013; Hirayama et al., 2007), our findings suggest that K537 acetylation does not affect the BMAL1-TAD-CBP-KIX interaction. As K537 acetylation is daily rhythmic in mouse liver peaking in the repressive phase (Hirayama et al., 2007), it is possible that CBP-KIX may preferentially bind to non-acetylated BMAL1 during the transcriptionally active phase. However, in the context of full-length CBP and in cells, BMAL1-CBP interactions could still be modulated by K537 acetylation through alternative mechanisms such as by promoting the participation of multiple domains of CBP in interaction, as for example in the case of acetylated CREB-pKID (Paz et al., 2014). Moreover, further *in vivo* investigation is required to determine the putative effect of K537$_{BMAL1}$ acetylation on CBP-dependent co-activation of CLOCK:BMAL1 or circadian chromatin modification.

4.6 Conclusions and Future prospects

In summary, the study performed herein has highlighted the significance of the MLL-binding pocket of KIX for BMAL1 interactions and determined the location of the N-terminal region preceding BMAL1-TAD and including the parts of the G-region, relative to the BMAL1-TAD:KIX core complex. Additionally, the moderate effect of mutations in the second binding pocket of KIX on BMAL1 binding suggested that the BMAL1-KIX interactions are not predominantly mediated via the second KIX binding pocket. Furthermore, we observed a negative interference of MLL1-TAD binding and of 1-10 tethering to N627 on BMAL1 binding, rather than a positive cooperative

effect as in case of pKID binding (Goto et al., 2002; Wang et al., 2014), suggesting that BMAL1 does not bind to KIX in a CREB-pKID like manner. Based on the work presented in this thesis, the formation of a ternary BMAL1/CBP/CREB complex can therefore not be excluded. In addition to the *in vitro* biophysical and biochemical experiments performed here, *in vivo* validation and high-resolution structures are required to provide a closer look into the complex formation and conclusively define the effect of these mutations on BMAL1-CBP interactions. Moreover, BMAL1 peptides including the last seven residues could be designed for co-crystallization with the 1-10 tethered KIX domain. Additionally, *in vivo* and mutational studies could be carried out to deduce the importance of loop region near the MLL-pocket of the KIX domain that displaced significantly in our newly determined KIX-1-10 crystal structure.

For the regulation of circadian transcription and chromatin modification as well as phase resetting and light entrainment of the clock via *per1* gene activation, the CBP is recruited to CLOCK:BMAL1 and/or CREB (Gau et al., 2002; Travnickova-Bendova et al., 2002) for which the interplay between BMAL1 and CREB binding to CBP plays a critical role and needs to be further analyzed. Furthermore, the impact of the posttranslational modifications on BMAL1-CBP interaction could be further explored. For example, the CREB-pKID phosphorylation on Ser133 and Ser142 affects the KIX binding and plays a critical role in the SCN light entrainment (Gau et al., 2002) and the pKID acetylation on Lys136 promotes binding to the bromodomain of CBP in addition to the KIX domain (Paz et al., 2014). Besides that, the contribution of the additional domains of CBP in interaction with BMAL1 also needs to be analyzed. Such as, BMAL1 acetylation may promote its interaction with the CBP-Bromodomain similar to the CREB-pKID acetylation and could form a ternary complex with the CBP-KIX to enhance the recruitment of CBP to CLOCK:BMAL1 in circadian gene regulation, but it is largely unknown and could be further examined. The work presented herein has significantly advanced our mechanistic understanding of BMAL1-CBP interactions and lays a stepping stone for further structural and mechanistic analyses which is required to fully understand the protein interaction networks underlying CBP- and CRY1-dependent gene regulation in the mammalian circadian clock.

References

Aguilar-Arnal, L., Katada, S., Orozco-Solis, R., and Sassone-Corsi, P. (2015). NAD+-SIRT1 control of H3K4 trimethylation through circadian deacetylation of MLL1. Nat. Struct. Mol. Biol. *22*, 312–318.

Ahijado-Guzmán, R., Prasad, J., Rosman, C., Henkel, A., Tome, L., Schneider, D., Rivas, G., and Sönnichsen, C. (2014). Plasmonic Nanosensors for Simultaneous Quantification of Multiple Protein–Protein Binding Affinities. Nano Lett. *14*, 5528–5532.

Ahijado-Guzmán, R., Menten, J., Prasad, J., Lambertz, C., Rivas, G., and Sönnichsen, C. (2017). Plasmonic Nanosensors for the Determination of Drug Effectiveness on Membrane Receptors. ACS Appl. Mater. Interfaces *9*, 218–223.

Antoch, M.P., and Kondratov, R. V. (2010). Circadian proteins and genotoxic stress response. Circ. Res.

Aryal, R.P., Kwak, P.B., Tamayo, A.G., Gebert, M., Chiu, P.-L., Walz, T., and Weitz, C.J. (2017). Macromolecular Assemblies of the Mammalian Circadian Clock. Mol. Cell *67*, 770-782.e6.

Avalos, J.L., Bever, K.M., and Wolberger, C. (2005). Mechanism of sirtuin inhibition by nicotinamide: altering the NAD(+) cosubstrate specificity of a Sir2 enzyme. Mol. Cell *17*, 855–868.

Baker, C.L., Loros, J.J., and Dunlap, J.C. (2012). The circadian clock of Neurospora crassa. FEMS Microbiol. Rev.

Barun, B. (2013). Pathophysiological background and clinical characteristics of sleep disorders in multiple sclerosis. Clin. Neurol. Neurosurg. *115*.

Bélanger, V., Picard, N., and Cermakian, N. (2006). The circadian regulation of Presenilin-2 gene expression. Chronobiol. Int. *23*, 747–766.

Bell-Pedersen, D., Cassone, V.M., Earnest, D.J., Golden, S.S., Hardin, P.E., Thomas, T.L., and Zoran, M.J. (2005). Circadian rhythms from multiple oscillators: Lessons from diverse organisms. Nat. Rev. Genet.

Bernard, P., Gabarit, P., Bahassi, E.M., and Couturier, M. (1994). Positive-selection vectors using

the F plasmid ccdB killer gene. Gene *148*, 71–74.

Berson, D.M. (2003). Strange vision: Ganglion cells as circadian photoreceptors. Trends Neurosci.

Blanchet, C.E., Spilotros, A., Schwemmer, F., Graewert, M.A., Kikhney, A., Jeffries, C.M., Franke, D., Mark, D., Zengerle, R., Cipriani, F., et al. (2015). Versatile sample environments and automation for biological solution X-ray scattering experiments at the P12 beamline (PETRA III, DESY). J. Appl. Crystallogr. *48*, 431–443.

Brown, S.A., Ripperger, J., Kadener, S., Fleury-Olela, F., Vilbois, F., Rosbash, M., and Schibler, U. (2005). Cell biology: PERIOD1-associated proteins modulate the negative limb of the mammalian circadian oscillator. Science (80-.).

Brüschweiler, S., Konrat, R., and Tollinger, M. (2013). Allosteric communication in the KIX domain proceeds through dynamic repacking of the hydrophobic core. ACS Chem. Biol.

Buhr, E.D., and Takahashi, J.S. (2013). Molecular components of the mammalian circadian clock. Handb. Exp. Pharmacol.

Buhr, E.D., Yoo, S.H., and Takahashi, J.S. (2010). Temperature as a universal resetting cue for mammalian circadian oscillators. Science (80-.).

Bunger, M.K., Wilsbacher, L.D., Moran, S.M., Clendenin, C., Radcliffe, L.A., Hogenesch, J.B., Simon, M.C., Takahashi, J.S., and Bradfield, C.A. (2000). Mop3 is an essential component of the master circadian pacemaker in mammals. Cell *103*, 1009–1017.

Busino, L., Bassermann, F., Maiolica, A., Lee, C., Nolan, P.M., Godinho, S.I.H., Draetta, G.F., and Pagano, M. (2007). SCFFbxl3controls the oscillation of the circadian clock by directing the degradation of cryptochrome proteins. Science (80-.).

Campbell, K.M., and Lumb, K.J. (2002). Structurally distinct modes of recognition of the KIX domain of CBP by Jun and CREB. Biochemistry.

Chauhan, R., Chen, K.F., Kent, B.A., and Crowther, D.C. (2017). Central and peripheral circadian clocks and their role in Alzheimer's disease. DMM Dis. Model. Mech. *10*, 1187–1199.

Chaves, I., Yagita, K., Barnhoorn, S., Okamura, H., van der Horst, G.T.J., and Tamanini, F. (2006). Functional Evolution of the Photolyase/Cryptochrome Protein Family: Importance of the C Terminus of Mammalian CRY1 for Circadian Core Oscillator Performance. Mol. Cell. Biol. *26*, 1743–1753.

Chaves, I., Pokorny, R., Byrdin, M., Hoang, N., Ritz, T., Brettel, K., Essen, L.-O., van der Horst, G.T.J., Batschauer, A., and Ahmad, M. (2011). The Cryptochromes: Blue Light Photoreceptors in Plants and Animals. Annu. Rev. Plant Biol.

Chou, D.M., and Elledge, S.J. (2006). Tipin and Timeless form a mutually protective complex required for genotoxic stress resistance and checkpoint function. Proc. Natl. Acad. Sci. U. S. A. *103*, 18143–18147.

Coomans, C.P., Van Den Berg, S.A.A., Houben, T., Van Klinken, J.B., Van Den Berg, R., Pronk, A.C.M., Havekes, L.M., Romijn, J.A., Van Dijk, K.W., Biermasz, N.R., et al. (2013). Detrimental effects of constant light exposure and high-fat diet on circadian energy metabolism and insulin sensitivity. FASEB J. *27*, 1721–1732.

Curtis, A.M., Cheng, Y., Kapoor, S., Reilly, D., Price, T.S., and FitzGerald, G.A. (2007). Circadian variation of blood pressure and the vascular response to asynchronous stress. Proc. Natl. Acad. Sci. U. S. A. *104*, 3450–3455.

Czarna, A., Breitkreuz, H., Mahrenholz, C.C., Arens, J., Strauss, H.M., and Wolf, E. (2011). Quantitative analyses of cryptochrome-mBMAL1 interactions: mechanistic insights into the transcriptional regulation of the mammalian circadian clock. J. Biol. Chem. *286*, 22414–22425.

Czarna, A., Berndt, A., Singh, H.R., Grudziecki, A., Ladurner, A.G., Timinszky, G., Kramer, A., and Wolf, E. (2013). Structures of Drosophila Cryptochrome and Mouse Cryptochrome1 Provide Insight into Circadian Function. Cell *153*, 1394–1405.

Dallmann, R., and Weaver, D.R. (2010). Altered body mass regulation in male mPeriod mutant mice on high-fat diet. Chronobiol. Int. *27*, 1317–1328.

Delezie, J., Dumont, S., Dardente, H., Oudart, H., Gréchez-Cassiau, A., Klosen, P., Teboul, M.,

Delaunay, F., Pévet, P., and Challet, E. (2012). The nuclear receptor REV-ERBα is required for the daily balance of carbohydrate and lipid metabolism. FASEB J. *26*, 3321–3335.

Delvecchio, M., Gaucher, J., Aguilar-Gurrieri, C., Ortega, E., and Panne, D. (2013). Structure of the p300 catalytic core and implications for chromatin targeting and HAT regulation. Nat. Struct. Mol. Biol.

Dibner, C., Schibler, U., and Albrecht, U. (2010). The Mammalian Circadian Timing System: Organization and Coordination of Central and Peripheral Clocks. Annu. Rev. Physiol.

Doi, M., Takahashi, Y., Komatsu, R., Yamazaki, F., Yamada, H., Haraguchi, S., Emoto, N., Okuno, Y., Tsujimoto, G., Kanematsu, A., et al. (2010). Salt-sensitive hypertension in circadian clock-deficient Cry-null mice involves dysregulated adrenal Hsd3b6. Nat. Med. *16*, 67–74.

Duong, H.A., and Weitz, C.J. (2014). Temporal orchestration of repressive chromatin modifiers by circadian clock Period complexes. Nat. Struct. Mol. Biol. *21*, 126–132.

Duong, H.A., Robles, M.S., Knutti, D., and Weitz, C.J. (2011). A molecular mechanism for circadian clock negative feedback. Science (80-.). *332*, 1436–1439.

Durgan, D.J., and Young, M.E. (2010). The cardiomyocyte circadian clock: Emerging roles in health and disease. Circ. Res. *106*, 647–658.

Dyson, H.J., and Wright, P.E. (2016). Role of Intrinsic Protein Disorder in the Function and Interactions of the Transcriptional Coactivators CREB-binding Protein (CBP) and p300. J. Biol. Chem. *291*, 6714–6722.

Erickson, H.P. (2009). Size and shape of protein molecules at the nanometer level determined by sedimentation, gel filtration, and electron microscopy. Biol. Proced. Online.

Ernst, P., Wang, J., Huang, M., Goodman, R.H., and Korsmeyer, S.J. (2001). MLL and CREB bind cooperatively to the nuclear coactivator CREB-binding protein. Mol. Cell. Biol. *21*, 2249–2258.

Etchegaray, J.-P., Lee, C., Wade, P.A., and Reppert, S.M. (2003). Rhythmic histone acetylation underlies transcription in the mammalian circadian clock. Nature *421*, 177–182.

Ferreon, J.C., Lee, C.W., Arai, M., Martinez-Yamout, M.A., Dyson, H.J., and Wright, P.E. (2009). Cooperative regulation of p53 by modulation of ternary complex formation with CBP/p300 and HDM2. Proc. Natl. Acad. Sci. U. S. A. *106*, 6591–6596.

Filipski, E., Li, X.M., and Lévi, F. (2006). Disruption of circadian coordination and malignant growth. Cancer Causes Control *17*, 509–514.

La Fleur, S.E., Kalsbeek, A., Wortel, J., Fekkes, M.L., and Buijs, R.M. (2001). A daily rhythm in glucose tolerance: A role for the suprachiasmatic nucleus. Diabetes *50*, 1237–1243.

Franke, D., and Svergun, D.I. (2009). *DAMMIF* , a program for rapid *ab-initio* shape determination in small-angle scattering. J. Appl. Crystallogr. *42*, 342–346.

Franke, D., Petoukhov, M. V, Konarev, P. V, Panjkovich, A., Tuukkanen, A., Mertens, H.D.T., Kikhney, A.G., Hajizadeh, N.R., Franklin, J.M., Jeffries, C.M., et al. (2017). ATSAS 2.8: a comprehensive data analysis suite for small-angle scattering from macromolecular solutions. J. Appl. Cryst *50*, 1212–1225.

Fu, L., Pelicano, H., Liu, J., Huang, P., and Lee, C.C. (2002). The circadian gene Period2 plays an important role in tumor suppression and DNA damage response in vivo. Cell *111*, 41–50.

Gale, J.E., Cox, H.I., Qian, J., Block, G.D., Colwell, C.S., and Matveyenko, A. V. (2011). Disruption of circadian rhythms accelerates development of diabetes through pancreatic beta-cell loss and dysfunction. J. Biol. Rhythms *26*, 423–433.

Garg, A., Orru, R., Ye, W., Distler, U., Chojnacki, J.E., Köhn, M., Tenzer, S., Sönnichsen, C., and Wolf, E. (2019). Structural and mechanistic insights into the interaction of the circadian transcription factor BMAL1 with the KIX domain of the CREB-binding protein. J. Biol. Chem. *294*, 16604–16619.

Gatfield, D., and Schibler, U. (2007). Proteasomes keep the circadian clock ticking. Science (80-.).

Gau, D., Lemberger, T., von Gall, C., Kretz, O., Le Minh, N., Gass, P., Schmid, W., Schibler, U., Korf, H.W., and Schütz, G. (2002). Phosphorylation of CREB Ser142 Regulates Light-Induced Phase

Shifts of the Circadian Clock. Neuron *34*, 245–253.

Gekakis, N., Staknis, D., Nguyen, H.B., Davis, F.C., Wilsbacner, L.D., King, D.P., Takahashi, J.S., and Weitz, C.J. (1998). Role of the CLOCK protein in the mammalian circadian mechanism. Science (80-.).

Gery, S., Komatsu, N., Baldjyan, L., Yu, A., Koo, D., and Koeffler, H.P. (2006). The Circadian Gene Per1 Plays an Important Role in Cell Growth and DNA Damage Control in Human Cancer Cells. Mol. Cell *22*, 375–382.

Gianni, S., Morrone, A., Giri, R., and Brunori, M. (2012). A folding-after-binding mechanism describes the recognition between the transactivation domain of c-Myb and the KIX domain of the CREB-binding protein. Biochem. Biophys. Res. Commun. *428*, 205–209.

Giordano, A., and Avantaggiati, M.L. (1999). p300 and CBP: Partners for life and death. J. Cell. Physiol. *181*, 218–230.

Goto, N.K., Zor, T., Martinez-Yamout, M., Dyson, H.J., and Wright, P.E. (2002). Cooperativity in transcription factor binding to the coactivator CREB-binding protein (CBP). The mixed lineage leukemia protein (MLL) activation domain binds to an allosteric site on the KIX domain. J. Biol. Chem. *277*, 43168–43174.

Gotter, A.L., Suppa, C., and Emanuel, B.S. (2007). Mammalian TIMELESS and Tipin are Evolutionarily Conserved Replication Fork-associated Factors. J. Mol. Biol. *366*, 36–52.

Grossman, S.R. (2001). p300/CBP/p53 interaction and regulation of the p53 response. Eur. J. Biochem.

Gu, Z., Wang, B., Zhang, Y.B., Ding, H., Zhang, Y., Yu, J., Gu, M., Chan, P., and Cai, Y. (2015). Association of ARNTL and PER1 genes with Parkinson's disease: A case-control study of Han Chinese. Sci. Rep. *5*.

Gustafson, C.L., and Partch, C.L. (2015). Emerging Models for the Molecular Basis of Mammalian Circadian Timing. Biochemistry *54*, 134–149.

Gustafson, C.L., Parsley, N.C., Asimgil, H., Lee, H.-W., Ahlbach, C., Michael, A.K., Xu, H., Williams,

O.L., Davis, T.L., Liu, A.C., et al. (2017). A Slow Conformational Switch in the BMAL1 Transactivation Domain Modulates Circadian Rhythms. Mol. Cell *66*, 447-457.e7.

De Guzman, R.N., Goto, N.K., Dyson, H.J., and Wright, P.E. (2006). Structural Basis for Cooperative Transcription Factor Binding to the CBP Coactivator. J. Mol. Biol. *355*, 1005–1013.

Hajizadeh, N.R., Franke, D., Jeffries, C.M., and Svergun, D.I. (2018). Consensus Bayesian assessment of protein molecular mass from solution X-ray scattering data. Sci. Rep. *8*, 7204.

Henzler-Wildman, K., and Kern, D. (2007). Dynamic personalities of proteins. Nature *450*, 964–972.

Hirayama, J., Sahar, S., Grimaldi, B., Tamaru, T., Takamatsu, K., Nakahata, Y., and Sassone-Corsi, P. (2007). CLOCK-mediated acetylation of BMAL1 controls circadian function. Nature *450*, 1086–1090.

Homolak, J., Mudrovčić, M., Vukić, B., and Toljan, K. (2018). Circadian Rhythm and Alzheimer's Disease. Med. Sci. *6*, 52.

Hood, S., and Amir, S. (2017). Neurodegeneration and the circadian clock. Front. Aging Neurosci. *9*.

Van Der Horst, G.T.J., Muijtjens, M., Kobayashi, K., Takano, R., Kanno, S.I., Takao, M., De Wit, J., Verkerk, A., Eker, A.P.M., Van Leenen, D., et al. (1999). Mammalian Cry1 and Cry2 are essential for maintenance of circadian rhythms. Nature.

Huang, N., Chelliah, Y., Shan, Y., Taylor, C.A., Yoo, S.H., Partch, C., Green, C.B., Zhang, H., and Takahashi, J.S. (2012). Crystal structure of the heterodimeric CLOCK:BMAL1 transcriptional activator complex. Science (80-.).

Ikeda, M., and Nomura, M. (1997). CDNA cloning and tissue-specific expression of a novel basic helex-loop-helix/PAS protein (BMAL1) and identification of alternatively spliced variants with alternative translation initiation site. Biochem. Biophys. Res. Commun. *233*, 258–264.

Ikeda, M., Yu, W., Hirai, M., Ebisawa, T., Honma, S., Yoshimura, K., Honma, K.I., and Nomura, M. (2000). cDNA cloning of a novel bHLH-PAS transcription factor superfamily gene, BMAL2: Its

mRNA expression, subcellular distribution, and chromosomal localization. Biochem. Biophys. Res. Commun. *275*, 493–502.

Ito, A., Lai, C.H., Zhao, X., Saito, S., Hamilton, M.H., Appella, E., and Yao, T.P. (2001). p300/CBP-mediated p53 acetylation is commonly induced by p53-activating agents and inhibited by MDM2. EMBO J. *20*, 1331–1340.

Janknecht, R., and Hunter, T. (1996). A growing coactivator network. Nature *383*, 22–23.

Johnson, C.H., Mori, T., and Xu, Y. (2008). A Cyanobacterial Circadian Clockwork. Curr. Biol.

Kang, J.E., Lim, M.M., Bateman, R.J., Lee, J.J., Smyth, L.P., Cirrito, J.R., Fujiki, N., Nishino, S., and Holtzman, D.M. (2009). Amyloid-β dynamics are regulated by orexin and the sleep-wake cycle. Science (80-.). *326*, 1005–1007.

Kasper, L.H., Boussouar, F., Ney, P.A., Jackson, C.W., Rehg, J., van Deursen, J.M., and Brindle, P.K. (2002). A transcription-factor-binding surface of coactivator p300 is required for haematopoiesis. Nature *419*, 738–743.

Katada, S., and Sassone-Corsi, P. (2010). The histone methyltransferase MLL1 permits the oscillation of circadian gene expression. Nat. Struct. Mol. Biol. *17*, 1414–1421.

Kee, B.L., Arias, J., and Montminy, M.R. (1996). Adaptor-mediated recruitment of RNA polymerase II to a signal-dependent activator. J. Biol. Chem. *271*, 2373–2375.

Kiyohara, Y.B., Tagao, S., Tamanini, F., Morita, A., Sugisawa, Y., Yasuda, M., Yamanaka, I., Ueda, H.R., van der Horst, G.T.J., Kondo, T., et al. (2006). The BMAL1 C terminus regulates the circadian transcription feedback loop. Proc. Natl. Acad. Sci. U. S. A. *103*, 10074–10079.

Koike, N., Yoo, S.-H., Huang, H.-C., Kumar, V., Lee, C., Kim, T.-K., and Takahashi, J.S. (2012). Transcriptional architecture and chromatin landscape of the core circadian clock in mammals. Science *338*, 349–354.

Kondratov, R. V., and Antoch, M.P. (2007). Circadian proteins in the regulation of cell cycle and genotoxic stress responses. Trends Cell Biol. *17*, 311–317.

Kondratov, R. V., Kondratova, A.A., Gorbacheva, V.Y., Vykhovanets, O. V., and Antoch, M.P. (2006). Early aging and age-related pathologies in mice deficient in BMAL1, the core component of the circadian clock. Genes Dev. *20*, 1868–1873.

Kume, K., Zylka, M.J., Sriram, S., Shearman, L.P., Weaver, D.R., Jin, X., Maywood, E.S., Hastings, M.H., and Reppert, S.M. (1999). mCRY1 and mCRY2 Are Essential Components of the Negative Limb of the Circadian Clock Feedback Loop. Cell *98*, 193–205.

Kung, A.L., Rebel, V.I., Bronson, R.T., Ch'ng, L.E., Sieff, C.A., Livingston, D.M., and Yao, T.P. (2000). Gene dose-dependent control of hematopoiesis and hematologic tumor suppression by CBP. Genes Dev. *14*, 272–277.

Lamia, K.A., Sachdeva, U.M., Di Tacchio, L., Williams, E.C., Alvarez, J.G., Egan, D.F., Vasquez, D.S., Juguilon, H., Panda, S., Shaw, R.J., et al. (2009). AMPK regulates the circadian clock by cryptochrome phosphorylation and degradation. Science (80-.).

Lee, B., Aiqing Li, A., Hansen, K.F., Ruifeng Cao, R., Jae Hwa Yoon, J.H., and Obrietan, K. (2010). CREB Influences Timing and Entrainment of the SCN Circadian Clock. J. Biol. Rhythms *25*, 410–420.

Lee, C.W., Arai, M., Martinez-Yamout, M.A., Dyson, H.J., and Wright, P.E. (2009). Mapping the interactions of the p53 transactivation domain with the KIX domain of CBP. Biochemistry.

Lee, Y.H., Bedford, M.T., and Stallcup, M.R. (2011). Regulated recruitment of tumor suppressor BRCA1 to the p21 gene by coactivator methylation. Genes Dev.

Lefta, M., Campbell, K.S., Feng, H.Z., Jin, J.P., and Esser, K.A. (2012). Development of dilated cardiomyopathy in Bmal1-deficient mice. Am. J. Physiol. - Hear. Circ. Physiol. *303*.

Li, M.Z., and Elledge, S.J. (2007). Harnessing homologous recombination in vitro to generate recombinant DNA via SLIC. Nat. Methods *4*, 251–256.

Liu, H., and Naismith, J.H. (2008). An efficient one-step site-directed deletion, insertion, single and multiple-site plasmid mutagenesis protocol. BMC Biotechnol. *8*, 91.

Lowrey, P.L., and Takahashi, J.S. (2004). MAMMALIAN CIRCADIAN BIOLOGY: Elucidating Genome-

Wide Levels of Temporal Organization. Annu. Rev. Genomics Hum. Genet.

Lu, K.P., Finn, G., Lee, T.H., and Nicholson, L.K. (2007). Prolyl cis-trans isomerization as a molecular timer. Nat. Chem. Biol.

Lucas, R.J., Hattar, S., Takao, M., Berson, D.M., Foster, R.G., and Yau, K.W. (2003). Diminished pupillary light reflex at high irradiances in melanopsin-knockout mice. Science (80-.).

Luckow, V.A., Lee, S.C., Barry, G.F., and Olins, P.O. (1993). Efficient generation of infectious recombinant baculoviruses by site-specific transposon-mediated insertion of foreign genes into a baculovirus genome propagated in Escherichia coli. J. Virol. *67*, 4566–4579.

Marcheva, B., Ramsey, K.M., Buhr, E.D., Kobayashi, Y., Su, H., Ko, C.H., Ivanova, G., Omura, C., Mo, S., Vitaterna, M.H., et al. (2010). Disruption of the clock components CLOCK and BMAL1 leads to hypoinsulinaemia and diabetes. Nature *466*, 627–631.

Merbitz-Zahradnik, T., and Wolf, E. (2015). How is the inner circadian clock controlled by interactive clock proteins?: Structural analysis of clock proteins elucidates their physiological role. FEBS Lett. *589*, 1516–1529.

Miyazaki, K., Wakabayashi, M., Hara, Y., and Ishida, N. (2010). Tumor growth suppression in vivo by overexpression of the circadian component, PER2. Genes to Cells *15*, 351–358.

Mohawk, J.A., and Takahashi, J.S. (2011). Cell autonomy and synchrony of suprachiasmatic nucleus circadian oscillators. Trends Neurosci.

Mohawk, J.A., Green, C.B., and Takahashi, J.S. (2012). Central and Peripheral Circadian Clocks in Mammals. Annu. Rev. Neurosci.

Nakajima, T., Uchida, C., Anderson, S.F., Chee-Gun, L., Hurwitz, J., Parvin, J.D., and Montminy, M. (1997). RNA helicase A mediates association of CBP with RNA polymerase II. Cell *90*, 1107–1112.

Neumann, H., Peak-Chew, S.Y., and Chin, J.W. (2008). Genetically encoding Nε-acetyllysine in recombinant proteins. Nat. Chem. Biol. *4*, 232–234.

Neumann, H., Hancock, S.M., Buning, R., Routh, A., Chapman, L., Somers, J., Owen-Hughes, T.,

van Noort, J., Rhodes, D., and Chin, J.W. (2009). A Method for Genetically Installing Site-Specific Acetylation in Recombinant Histones Defines the Effects of H3 K56 Acetylation. Mol. Cell *36*, 153–163.

Ogryzko, V. V, Schiltz, R.L., Russanova, V., Howard, B.H., and Nakatani, Y. (1996). The Transcriptional Coactivators p300 and CBP Are Histone Acetyltransferases. Cell *87*, 953–959.

Ondo, W.G. (2014). Sleep/wake problems in Parkinson's disease: Pathophysiology and clinicopathologic correlations. J. Neural Transm. *121*.

Padmanabhan, K., Robles, M.S., Westerling, T., and Weitz, C.J. (2012). Feedback regulation of transcriptional termination by the mammalian circadian clock PERIOD complex. Science (80-.). *337*, 599–602.

Panda, S., Sato, T.K., Castrucci, A.M., Rollag, M.D., DeGrip, W.J., Hogenesch, J.B., Provencio, I., and Kay, S.A. (2002). Melanopsin (Opn4) requirement for normal light-induced circadian phase shifting. Science (80-.).

Panjkovich, A., and Svergun, D.I. (2016). Deciphering conformational transitions of proteins by small angle X-ray scattering and normal mode analysis. Phys. Chem. Chem. Phys. *18*, 5707–5719.

Park, N., Kim, H.-D., Cheon, S., Row, H., Lee, J., Han, D.-H., Cho, S., and Kim, K. (2015). A Novel Bmal1 Mutant Mouse Reveals Essential Roles of the C-Terminal Domain on Circadian Rhythms. PLoS One *10*, e0138661.

Parker, D., Rivera, M., Zor, T., Henrion-Caude, A., Radhakrishnan, I., Kumar, A., Shapiro, L.H., Wright, P.E., Montminy, M., and Brindle, P.K. (1999). Role of secondary structure in discrimination between constitutive and inducible activators. Mol. Cell. Biol. *19*, 5601–5607.

Partch, C.L., Green, C.B., and Takahashi, J.S. (2014). Molecular architecture of the mammalian circadian clock. Trends Cell Biol. *24*, 90–99.

Paz, J.C., Park, S., Phillips, N., Matsumura, S., Tsai, W.-W., Kasper, L., Brindle, P.K., Zhang, G., Zhou, M.-M., Wright, P.E., et al. (2014). Combinatorial regulation of a signal-dependent activator by phosphorylation and acetylation. Proc. Natl. Acad. Sci. U. S. A. *111*, 17116–17121.

Pettersen, E.F., Goddard, T.D., Huang, C.C., Couch, G.S., Greenblatt, D.M., Meng, E.C., and Ferrin, T.E. (2004). UCSF Chimera- A visualization system for exploratory research and analysis. J. Comput. Chem. *25*, 1605–1612.

Prasad, R., Yano, T., Sorio, C., Nakamura, T., Rallapalli, R., Gu, Y., Leshkowitz, D., Croce, C.M., and Canaani, E. (1995). Domains with transcriptional regulatory activity within the ALL1 and AF4 proteins involved in acute leukemia. Proc. Natl. Acad. Sci. U. S. A. *92*, 12160–12164.

Radhakrishnan, I., Pérez-Alvarado, G.C., Parker, D., Dyson, H.J., Montminy, M.R., and Wright, P.E. (1997). Solution Structure of the KIX Domain of CBP Bound to the Transactivation Domain of CREB: A Model for Activator:Coactivator Interactions. Cell *91*, 741–752.

Richards, J., and Gumz, M.L. (2013). Mechanism of the circadian clock in physiology. Am. J. Physiol. - Regul. Integr. Comp. Physiol.

Sanada, K., Harada, Y., Sakai, M., Todo, T., and Fukada, Y. (2004). Serine phosphorylation of mCRY1 and mCRY2 by mitogen-activated protein kinase. Genes to Cells.

Sancar, A. (2003). Structure and function of DNA photolyase and cryptochrome blue-light photoreceptors. Chem. Rev.

SantaLucia, J., and Hicks, D. (2004). The Thermodynamics of DNA Structural Motifs. Annu. Rev. Biophys. Biomol. Struct. *33*, 415–440.

Sato, T.K., Yamada, R.G., Ukai, H., Baggs, J.E., Miraglia, L.J., Kobayashi, T.J., Welsh, D.K., Kay, S.A., Ueda, H.R., and Hogenesch, J.B. (2006). Feedback repression is required for mammalian circadian clock function. Nat. Genet.

Schmalen, I., Reischl, S., Wallach, T., Klemz, R., Grudziecki, A., Prabu, J.R., Benda, C., Kramer, A., and Wolf, E. (2014). Interaction of circadian clock proteins CRY1 and PER2 is modulated by zinc binding and disulfide bond formation. Cell *157*, 1203–1215.

Schmitt, K., Grimm, A., and Eckert, A. (2017). Amyloid-β-induced changes in molecular clock properties and cellular bioenergetics. Front. Neurosci. *11*.

Schneidman-Duhovny, D., Hammel, M., Tainer, J.A., and Sali, A. (2016). FoXS, FoXSDock and

MultiFoXS: Single-state and multi-state structural modeling of proteins and their complexes based on SAXS profiles. Nucleic Acids Res. *44*, W424–W429.

Shearman, L.P., Sriram, S., Weaver, D.R., Maywood, E.S., Chaves, I., Zheng, B., Kume, K., Lee, C.C., van der Horst, G.T., Hastings, M.H., et al. (2000). Interacting molecular loops in the mammalian circadian clock. Science *288*, 1013–1019.

Shi, S., Hida, A., McGuinness, O.P., Wasserman, D.H., Yamazaki, S., and Johnson, C.H. (2010). Circadian Clock Gene Bmal1 Is Not Essential; Functional Replacement with its Paralog, Bmal2. Curr. Biol. *20*, 316–321.

Shirogane, T., Jin, J., Ang, X.L., and Harper, J.W. (2005). SCFbeta-TRCP controls clock-dependent transcription via casein kinase 1-dependent degradation of the mammalian period-1 (Per1) protein. J. Biol. Chem. *280*, 26863–26872.

Solt, L.A., Wang, Y., Banerjee, S., Hughes, T., Kojetin, D.J., Lundasen, T., Shin, Y., Liu, J., Cameron, M.D., Noel, R., et al. (2012). Regulation of circadian behaviour and metabolism by synthetic REV-ERB agonists. Nature *485*, 62–68.

Song, H., Moon, M., Choe, H.K., Han, D.-H., Jang, C., Kim, A., Cho, S., Kim, K., and Mook-Jung, I. (2015). Aβ-induced degradation of BMAL1 and CBP leads to circadian rhythm disruption in Alzheimer's disease. Mol. Neurodegener. *10*, 13.

Sreerama, N., and Woody, R.W. (2000). Estimation of Protein Secondary Structure from Circular Dichroism Spectra: Comparison of CONTIN, SELCON, and CDSSTR Methods with an Expanded Reference Set. Anal. Biochem. *287*, 252–260.

Stewart, D.E., Sarkar, A., and Wampler, J.E. (1990). Occurrence and role ofcis peptide bonds in protein structures. J. Mol. Biol.

Stow, L.R., Richards, J., Cheng, K.Y., Lynch, I.J., Jeffers, L.A., Greenlee, M.M., Cain, B.D., Wingo, C.S., and Gumz, M.L. (2012). The circadian protein period 1 contributes to blood pressure control and coordinately regulates renal sodium transport genes. Hypertension *59*, 1151–1156.

Svergun, D.I. (1992). Determination of the regularization parameter in indirect-transform

methods using perceptual criteria. J. Appl. Crystallogr. *25*, 495–503.

Svergun, D.I. (1999). Restoring Low Resolution Structure of Biological Macromolecules from Solution Scattering Using Simulated Annealing. Biophys. J. *76*, 2879–2886.

Svergun, D., Barberato, C., and Koch, M.H.J. (1995). *CRYSOL* – a Program to Evaluate X-ray Solution Scattering of Biological Macromolecules from Atomic Coordinates. J. Appl. Crystallogr. *28*, 768–773.

Svergun, D.I., Petoukhov, M. V., and Koch, M.H.J. (2001). Determination of Domain Structure of Proteins from X-Ray Solution Scattering. Biophys. J. *80*, 2946–2953.

Takahashi, J.S., Hong, H.-K., Ko, C.H., and McDearmon, E.L. (2008). The genetics of mammalian circadian order and disorder: implications for physiology and disease. Nat. Rev. Genet. *9*, 764–775.

Takahata, S., Ozaki, T., Mimura, J., Kikuchi, Y., Sogawa, K., and Fujii-Kuriyama, Y. (2000). Transactivation mechanisms of mouse clock transcription factors, mClock and mArnt3. Genes to Cells.

Thakur, J.K., Yadav, A., and Yadav, G. (2014). Molecular recognition by the KIX domain and its role in gene regulation. Nucleic Acids Res. *42*, 2112–2125.

Travnickova-Bendova, Z., Cermakian, N., Reppert, S.M., and Sassone-Corsi, P. (2002). Bimodal regulation of mPeriod promoters by CREB-dependent signaling and CLOCK/BMAL1 activity. Proc. Natl. Acad. Sci. U. S. A. *99*, 7728–7733.

Turek, F.W., Joshu, C., Kohsaka, A., Lin, E., Ivanova, G., McDearmon, E., Laposky, A., Losee-Olson, S., Easton, A., Jensen, D.R., et al. (2005). Obesity and metabolic syndrome in circadian Clock mutant nice. Science (80-.). *308*, 1043–1045.

Unsal-Kacmaz, K., Mullen, T.E., Kaufmann, W.K., and Sancar, A. (2005). Coupling of Human Circadian and Cell Cycles by the Timeless Protein. Mol. Cell. Biol. *25*, 3109–3116.

La Verde, V., Dominici, P., and Astegno, A. (2017). Determination of Hydrodynamic Radius of Proteins by Size Exclusion Chromatography. BIO-PROTOCOL *7*.

Vo, N., and Goodman, R.H. (2001). CREB-binding protein and p300 in transcriptional regulation. J. Biol. Chem. *276*, 13505–13508.

Volkov, V. V., and Svergun, D.I. (2003). Uniqueness of *ab initio* shape determination in small-angle scattering. J. Appl. Crystallogr. *36*, 860–864.

Wang, F., Marshall, C.B., Yamamoto, K., Li, G.-Y., Gasmi-Seabrook, G.M.C., Okada, H., Mak, T.W., and Ikura, M. (2012). Structures of KIX domain of CBP in complex with two FOXO3a transactivation domains reveal promiscuity and plasticity in coactivator recruitment. Proc. Natl. Acad. Sci. U. S. A. *109*, 6078–6083.

Wang, N., Majmudar, C.Y., Pomerantz, W.C., Gagnon, J.K., Sadowsky, J.D., Meagher, J.L., Johnson, T.K., Stuckey, J. a, Brooks, C.L., Wells, J. a, et al. (2013a). Ordering a dynamic protein via a small molecule stabilizer. J. Am. Chem. Soc.

Wang, N., Lodge, J.M., Fierke, C.A., and Mapp, A.K. (2014). Dissecting allosteric effects of activator-coactivator complexes using a covalent small molecule ligand. Proc. Natl. Acad. Sci. U. S. A. *111*, 12061–12066.

Wang, Z., Wu, Y., Li, L., and Su, X.D. (2013b). Intermolecular recognition revealed by the complex structure of human CLOCK-BMAL1 basic helix-loop-helix domains with E-box DNA. Cell Res.

Webb, B., and Sali, A. (2014). Comparative Protein Structure Modeling Using MODELLER. Curr. Protoc. Bioinforma. *47*, 5.6.1-5.6.32.

Whitmore, L., and Wallace, B.A. (2004). DICHROWEB, an online server for protein secondary structure analyses from circular dichroism spectroscopic data. Nucleic Acids Res. *32*, W668–W673.

Xu, H., Gustafson, C.L., Sammons, P.J., Khan, S.K., Parsley, N.C., Ramanathan, C., Lee, H.-W., Liu, A.C., and Partch, C.L. (2015). Cryptochrome 1 regulates the circadian clock through dynamic interactions with the BMAL1 C terminus. Nat. Struct. Mol. Biol. *22*, 476–484.

Yagita, K., Tamanini, F., Yasuda, M., Hoeijmakers, J.H.J., Van der Horst, G.T.J., and Okamura, H. (2002). Nucleocytoplasmic shuttling and mCRY-dependent inhibition of ubiquitylation of the

mPER2 clock protein. EMBO J.

Yao, T.P., Oh, S.P., Fuchs, M., Zhou, N.D., Ch'ng, L.E., Newsome, D., Bronson, R.T., Li, E., Livingston, D.M., and Eckner, R. (1998). Gene dosage-dependent embryonic development and proliferation defects in mice lacking the transcriptional integrator p300. Cell *93*, 361–372.

Ye, R., Selby, C.P., Ozturk, N., Annayev, Y., and Sancar, A. (2011). Biochemical analysis of the canonical model for the mammalian circadian clock. J. Biol. Chem.

Ye, R., Selby, C.P., Chiou, Y.-Y., Ozkan-Dagliyan, I., Gaddameedhi, S., and Sancar, A. (2014). Dual modes of CLOCK:BMAL1 inhibition mediated by Cryptochrome and Period proteins in the mammalian circadian clock. Genes Dev. *28*, 1989–1998.

Ye, W., Götz, M., Celiksoy, S., Tüting, L., Ratzke, C., Prasad, J., Ricken, J., Wegner, S. V., Ahijado-Guzmán, R., Hugel, T., et al. (2018a). Conformational Dynamics of a Single Protein Monitored for 24 h at Video Rate. Nano Lett. *18*, 6633–6637.

Ye, W., Celiksoy, S., Jakab, A., Khmelinskaia, A., Heermann, T., Raso, A., Wegner, S. V., Rivas, G., Schwille, P., Ahijado-Guzmán, R., et al. (2018b). Plasmonic Nanosensors Reveal a Height Dependence of MinDE Protein Oscillations on Membrane Features. J. Am. Chem. Soc. *140*, 17901–17906.

Yu, W., and Hardin, P.E. (2006). Circadian oscillators of Drosophila and mammals. J. Cell Sci.

Zeng, Z.L., Luo, H.Y., Yang, J., Wu, W.J., Chen, D.L., Huang, P., and Xu, R.H. (2014). Overexpression of the circadian clock gene bmal1 increases sensitivity to oxaliplatin in colorectal cancer. Clin. Cancer Res. *20*, 1042–1052.

Zor, T., Mayr, B.M., Dyson, H.J., Montminy, M.R., and Wright, P.E. (2002). Roles of phosphorylation and helix propensity in the binding of the KIX domain of CREB-binding protein by constitutive (c-Myb) and inducible (CREB) activators. J. Biol. Chem. *277*, 42241–42248.

Zor, T., De Guzman, R.N., Dyson, H.J., and Wright, P.E. (2004). Solution Structure of the KIX Domain of CBP Bound to the Transactivation Domain of c-Myb. J. Mol. Biol.

Zuber, A.M., Centeno, G., Pradervand, S., Nikolaeva, S., Maquelin, L., Cardinaux, L., Bonny, O.,

and Firsov, D. (2009). Molecular clock is involved in predictive circadian adjustment of renal function. Proc. Natl. Acad. Sci. U. S. A. *106*, 16523–16528.